# Ultrasound and Microbubbles: Modulating and Quantifying Blood Flow in Liver Cancers

Connor Douglas Krolak

A dissertation submitted

in partial fulfillment of the

requirements for the degree of

Doctor of Philosophy

University of Washington

2026

Reading Committee:

Dr. Michalakis Averkiou, Chair

Dr. Thanasis Loupas

Dr. Xiaohu Gao

Dr. Neda Bagheri, GSR

Program Authorized to Offer Degree:

Bioengineering

University of Washington

# Abstract

Ultrasound and Microbubbles: Modulating and Quantifying Blood Flow in Liver Cancers

Connor Douglas Krolak

Chair of the Supervisory Committee:

Mike Averkiou

Department of Bioengineering

Contrast-enhanced ultrasound (CEUS) is an ever-developing field, uniquely branching between both diagnostic and therapeutic applications. In this body of work, we present several investigations on how ultrasound and microbubbles can be leveraged as a *theranostic* tool for the improved treatment of primary liver cancer, or hepatocellular carcinomas. These works emphasize clinical translation through the use of clinically approved technologies and agents, aiming for the rapid adoption of these approaches to combat the ever-evolving challenge of liver cancer. We begin with a brief introduction of the current clinical state of liver cancer, existing diagnostic and therapeutic strategies, and role of CEUS in these areas as explored in this thesis (**Chapter 1**). We then investigate the clinical use of CEUS to develop much needed repeatable metrics of tumor blood flow that enable accurate longitudinal evaluations (**Chapter 2**). We then describe quantitative diagnostic tools for the early detection of hepatocellular carcinoma and evaluate them in a clinical patient study (**Chapter 3)**. Using these important tumor blood flow quantification methods, we then investigate use of clinical ultrasound scanners image-guided for tumor blood flow alteration for enhanced drug penetration in a murine model of hepatocellular carcinoma (**Chapter 4**). We then describe the temporal and spatial dynamics of cavitation-induced tumor perfusion loss for a greater understanding of how acoustic conditions influence this phenomenon to design more effective therapeutic ultrasound-mediated cavitation strategies (**Chapter 5**). We discuss ongoing work investigating the role of ultrasound cavitation treatments in augmenting immunotherapy-based approaches in an orthotopic murine model of liver cancer (**Chapter 6**). We conclude with a summary of the accomplishments and future directions of this work (**Chapter 7**).

# TABLE OF CONTENTS

# LIST OF FIGURES

# LIST OF TABLES

# ACKNOWLEDGEMENTS

This work was supported by grants from the Brotman Baty Institute (BBI 683886 CC12), TL1 TR002318 (Krolak), and the National Institute of Biomedical Imaging and Bioengineering of the National Institutes of Health (R01EB032655). All acknowledgements to individuals are included following their respective chapters.

Firstly, I am forever grateful to my advisor, **Mike Averkiou**. You have been there to support me constantly throughout my PhD, inside and outside of the lab. You have taught me to work hard, speak directly to the data, and always ask questions. Your endless excitement for science is infectious, and your drive to make waves (*get it?*) in the field has inspired me to be a better scientist. I will never forget your kindness and generosity, and I am so grateful I had the opportunity to work for you. I'll always listen for the clinking of a washer in my car and think of you. I would also like to thank my Supervisory Committee: **Thanasis Loupas**, **Xiaohu Gao**, and **Neda Bagheri** for your support and advice. **Thanasis**, you were especially like a mentor to me and have always been invested in my success, and I am so incredibly grateful for that.

My growth as both a scientist and a person were not limited solely to my committee, I have been shaped by the relationships that I built during my time at UW. I am specifically grateful to the following people:

To my collaborator and mentor **Yak-Nam Wang** for your unrelenting support and kindness. Your persistence in checking on my well-being made more of a difference in my success than you know. Thank you for allowing me to ask so, so many questions and helping me grow in the researcher I am today. Your expertise and advise were pivotal to so much of the work in this thesis, and I could not have done this without you.

To my collaborators **Heidi Kenerson** and **Raymond Yeung**, thank you so much for all your guidance and critique of the biological component of this work. **Heidi**, I especially thank you for your superhuman efforts to support this work, and I am grateful for your surgical expertise.

To my first lab mates **Sara Keller**, **Ting-Yu Lai**, **Eric Juang**, and **Alicia Clark**, thank you for carving a path for my work, and your contributions to the lab set the example I aspired to follow. To members of the lab who worked directly with me: **Lance De Koninck**, **Kaleb Vuong, Sherry Gu**, **Jenifer Mendez Pacheco**, **Marissa Shumaker**, **Angela Wei**, and **Max Siauw**. You not only contributed directly to the success of this work but also helped me grow as a person and I am grateful for all of your friendships. To all members of the lab I bonded with: **Fadwa Shagroun**, **Phuong Tran**, **Hanna Michaelis** and the many undergrads, thank you all for your support and comradery over the years.

To my friends in Seattle, especially **Josephine Law** and **Zeinab Rashed**, for making Seattle feel like home. I am grateful for the many trips we have gone on together, thank you for making graduate school a great experience. Thank you to **Shane Gilligan-Steinberg** and **Kevin Jiang**, my first roommates in Seattle, for helping me find joy in being locked in an apartment during the pandemic.

To my grandparents, especially **Harold** and **Ginger Upp**, thank you for your unrelenting support and love. My love for nature and the world came from you, and I am a more empathetic, joyful, and loving person because of you both and I hope you are still watching over me.

To my brother, **Trevor Krolak**, thank you for always being a model of excellence to live up to. Your unapologetic passion for science and biology is inspiring, and I thank you for always sharing that world with me. Sorry that you're not the only Dr. Krolak now!

To my partner **Reggie Wimbley**, words alone cannot express my gratitude. You have been MY greatest supporter and cheerleader, raising me up every time that I stumbled. Thank you for helping me believe that I was worthy of achieving my dreams, and my life is so much better with you in it. A special thank you to **Alistair Wimbley** for the much-needed laughs and cuddles, and our shared love of food.

Finally, to my mother **Jennifer** and father **Steven Krolak**, for your endless support and love. You made so many sacrifices to give me the opportunities that led me here, and you continue to bring so much joy and love into my life.

# Chapter 1. INTRODUCTION

**Abstract**

Liver cancer, particularly hepatocellular carcinoma (HCC), presents a substantial healthcare burden that is only expected to rise. Despite medical advances, delays in diagnosis and impaired hepatic function associated with underlying HCC risk factors further restrict available treatment options. Ultrasound and microbubbles are being investigated in both imaging and therapy, as they can provide both a source of contrast-enhanced imaging signal and a generator of microscale forces relevant to treatment depending on acoustic conditions employed. In this chapter we introduce the current clinical challenges associated with diagnosis and therapy of HCC, and describe how imaging and treatment with ultrasound and microbubbles can be used to overcome them. Additionally, the overall research aims of the project and a summary of the chapters that follow will be presented.

## 1.1 DIAGNOSIS AND TREATMENT OF LIVER CANCER

Liver cancer, through its poor prognosis and highly aggressive nature, is the sixth most common cancer whose global impact is projected to increase (1). Hepatocellular carcinoma (HCC) is the most common primary liver malignancy and is the second leading cause of cancer-related deaths in men globally (2, 3). The global burden for this disease is even more significant in low-resource nations where prevalent HCC risk factors of Hepatitis B and C are more active (4). However, HCC has also been the fastest-rising cause of cancer-related deaths in the United States and is globally on the rise along with an increased prevalence of non-alcoholic fatty liver disease (5). Similarly, delays in diagnosis and compromised hepatic function due to underlying HCC risk factors limit treatment options, and are partly attributed to the high mortality of this disease (6). Therefore, developing novel methods for early HCC detection, precise treatment, and continuous monitoring are critical.

### 1.1.1 *Current diagnostic imaging strategies for HCC*

Current clinical HCC surveillance is tailored to the patient's risk profile through risk-assessment scores which evaluate factors such as age, hereditary risk, and gender (7). If liver cirrhosis is present, patients undergo periodic imaging surveillance and alpha-fetoprotein (AFP) testing due to high risk of development of focal liver lesions. Standard B-mode liver ultrasound (US) is often employed for imaging surveillance due to its broad accessibility and low cost in detecting liver tumors. HCC most often appears hypoechoic on B-mode ultrasound, but about a quarter of cases show hyperechoic or mixed patterns (8). Tumors under 1 cm of diameter may also appear isoechoic, further challenging diagnosis. Computed tomography (CT) and magnetic resonance imaging (MRI) techniques can also be used to detect focal liver lesions with greater sensitivity but exclude patient populations due to greater costs and radiation doses. Regardless of imaging modality utilized, once a lesion is identified further characterization is performed with contrast-based imaging to evaluate blood flow.

Due to differences in cellular compositions, focal liver lesions exhibit unique vascular patterns which can be used in differentiation and diagnosis. Contrast-enhanced ultrasound (CEUS) is well suited for assessing tumor vasculature because its contrast agents (1–10 μm inert gas microbubbles) are confined to the vascular space and function as true blood-pool tracers. This unique microbubble agent and imaging modality offers high temporal resolution, ease of use, and an excellent safety profile (9-11). Unlike contrast agents used in CT or MRI, microbubbles do not extravasate, enabling accurate evaluation of blood flow and tissue perfusion. For clinical diagnosis of focal liver lesions, Lumason microbubbles (Bracco, Geneva, Switzerland), marketed as SonoVue outside the United States are commonly used. Current diagnostic workflows rely on the distinctive vascular imaging properties of this microbubble.

HCC is diagnosed with vascular imaging via the presence arterial phase hyperenhancement (APHE) and its relative washout compared to parenchyma in the late phase as seen on contrast-enhanced CT, MRI, or US in addition to other ancillary features (12). To standardize the evaluations of HCCs from imaging, the Liver Imaging and Reporting Data System (LI-RADS) was created (13, 14), where lesions are categorized on a scale from 1 to 5 based on likelihood of being an HCC (where LR-1 is definitely benign and LR-5 is definitely HCC). CEUS has a slightly

modified LI-RADS scheme due to the microbubble nature of its contrast agent, particularly through the ability to detect "true washout" (15, 16). The observed washout in CEUS is thought to result from the lack of healthy reticuloendothelial (Kupffer) cells within the tumor which contribute to sustained microbubble signal observed in liver parenchyma via phagocytosis of the microbubble agent. At timepoints when the contribution of systemically circulating microbubbles is limited (4-5 minutes after contrast administration with a bolus injection), washout is depicted as a lack of contrast signal within the tumor as compared to the surrounding liver.

Although ultrasound is routinely used for lesion detection and surveillance and CEUS offers important advantages, including real-time visualization of arterial-phase hyperenhancement (APHE) and the ability to avoid vascular pseudo lesions such as arterioportal shunts (cite), the American Association for the Study of Liver Diseases (AASLD) still recommends contrast-enhanced CT or MRI as the initial modality for evaluating vascular characteristics (17, 18). Even though LI-RADS defines unique vascular features to identify HCCs, wash-in and washout criteria are based on subjective assessment and hypothetical time-intensity curves (TICs) that are not generated in clinical practice and only qualitative evaluations are made. Despite the high diagnostic specificity of CEUS LI-RADS, its moderate sensitivity and subjective evaluation could potentially be improved through the quantification of the vascular patterns defined in CEUS LI-RADS to promote its use as a first line vascular diagnostic option.

### 1.1.2 *Current therapeutic strategies for HCC*

Due to the complex series of risk factors impacting the liver, current treatment options are highly patient-specific with varying degrees of success. HCCs detected at early stages can be treated with localized therapies such as radiofrequency ablation (19), cryoablation (20), transarterial radioembolization (21), transarterial chemoembolization (22), and resection (23). However, these treatments not only have restrictive criteria such as requiring small lesions (<3 cm diameter) in ideal liver locations (distal from major vessels and bile ducts), but also still introduce perioperative risk (24, 25). Unfortunately, tumor recurrence remains a significant challenge due to poor tumor differentiation, the presence of satellite lesions, and especially the diseased state of the liver. Lack of completely curative treatment even plagues transplantation, where up to 15% of patients experience post-operative recurrence (26).

Recently, histotripsy has been FDA-approved for the treatment of liver cancers. Histotripsy is a novel technology that employs non-thermal, high-intensity focused ultrasound pulses to non-invasively ablate targeted tissue regions, converting them into acellular debris (27). Histotripsy relies on cavitation of bubbles generated within the sonicated medium by the ultrasound pulses to ablate tissue, heavily dependent on the device parameters utilized (28). The HistoSonics Edison (Ann Arbor, MI, USA) is a recently approved and adopted device that utilizes histotripsy for treating HCC. Current limitations of this technique include high cost of the device and the risk of injury to nearby structures and interference from the lungs, excluding some patients from this option (29).

In more advanced disease stages, patients are no longer eligible for localized therapies and must rely on systemic therapeutic approaches. Previous drug treatments included multi-drug therapies utilizing anti-angiogenics (Bevacizumab) and multikinase inhibitors (Sorafenib), aiming to tackle the abnormal vasculature and overexpression of VEGF-A inherent to solid tumors (30). However, these treatments have seen limited success, partly due to the presence of diffuse liver disease and partly attributed to the complex tumor microenvironment which compromises drug delivery. The current clinical standard of care are immune checkpoint inhibitors, but efficacy of these drug combinations is still being evaluated in clinical trials. However, clinical outcomes with immunotherapy have been inconsistent, with only about 20–30% of patients showing a response to single-agent treatment (31). Even the most commonly employed combination of anti-PD-1/PD-L1 inhibitors demonstrate response rates ranging from roughly 10% to 30% (32, 33), underscoring the need for more effective treatment strategies.

## 1.2 QUANTIFICATION OF CONTRAST-ENHANCED ULTRASOUND IMAGING

### 1.2.1 *Contrast imaging physics*

Shelled microbubbles exposed to an acoustic field undergo volumetric oscillations, radially compressing when the acoustic pressure exceeds ambient levels and expanding when the pressure falls below it (34). Above a threshold amplitude that amounts to a mechanical index (MI) of ~0.1, the shell integrity is disrupted, and this leads to microbubble destruction and gas diffusion. In

contrast-enhanced ultrasound imaging, a MI of 0.1 are typically employed to avoid microbubble destruction. Even at these low amplitudes, the resulting oscillations of the microbubble are asymmetric, and generate nonlinear backscattered echoes where not only the fundamental transmitted frequency ($f_0$) but also its harmonic multiples ($n * f_0$, where n is an integer) are emitted (35). Because their emitted frequencies are not solely the fundamental frequency used to excite them, microbubbles are often referred to as nonlinear acoustic scatterers. Meanwhile, at these low MIs used for microbubble imaging, ultrasound propagation in tissue is linear and the scattered ultrasound from tissue does not contain any significant harmonic components. Imaging strategies take advantage of the nonlinear property of microbubbles by utilizing pulse sequences designed to isolate harmonic components unique to these contrast agents, to generate microbubble-only images. Commonly used pulsing schemes include pulse inversion (36), amplitude modulation (37, 38), and amplitude-modulated pulse inversion (39) which consecutively send two or more pulses which are either inverse from one another or differ in amplitude. Through the combination of backscattered signals from these pulses, linear components are suppressed while nonlinear components are enhanced. Resulting CEUS images solely depict microbubbles, supplying information specific to blood flow (9). At these low MIs, microbubbles are not destroyed and can be repeatedly imaged in real time, capturing the temporal dynamics of the bloodstream that they are immersed in. Consequently, CEUS is a valuable clinical tool for assessing microvascular perfusion.

### 1.2.2 *Time-intensity curve analysis*

The most common approach for evaluating the temporal dynamics of contrast intensity within a region of interest (ROI) is through the generation of a time-intensity curve (TIC). TICs are derived from the average pixel intensity within the ROI repeated on each frame of for all frames of the image loop. Quantification of CEUS images is possible as the backscattered intensity from microbubbles at diagnostic MIs is proportional to microbubble concentration (40). However, microbubbles dosing is incredibly important, as too high of concentrations can attenuate sound and shadow deeper structure in a process known as acoustic shadowing (9).

Generation of a meaningful TIC for a ROI in 2D imaging requires that it continuously images the same plane and that motion across images is minimized. The two primary sources of motion for

CEUS scans of the liver are respiratory motion and probe motion, which are particularly impactful in HCC evaluations as washout can only be visualized 4-to-5 minutes after bolus injection and asking the patient to hold their breath is not feasible (41). Motion tracked from simultaneously acquired B-mode images is commonly used in motion-compensation algorithms, which must discard frames where the lesion moves out of plane and correct in-plane motion in the remaining frames (42-45). However, freehand CEUS introduces substantial risk of probe motion that cannot be reproduced, and maintaining a fixed imaging plane is essential for respiratory-gating and motion-correction methods (46).

TICs are often fitted to indicator-dilution models to suppress noise and enable estimation of perfusion-related parameters (47). Only TICs derived from linearized rather than DICOM/log-compressed data are suitable for model-based curve fitting approaches, but this functionality is typically restricted to proprietary software, limiting broader adoption of quantitative CEUS. In clinical studies to evaluate abdominal lesions with CEUS, the microbubble contrast agent is primarily delivered with a bolus injection due to their well-defined characteristics and ease of clinic use. However, another means of microbubble delivery is performed with infusion, where microbubbles are continuously delivered intravenously while microbubbles are agitated to establish a steady state of microbubble signal in the vasculature. Several studies have leveraged destruction-replenishment protocols with microbubble infusion to eliminate cardiopulmonary transit effects and enable repeated assessments of liver perfusion in clinical CEUS (48-50). However, it requires a specialized infusion pump to maintain continuous mixing and careful control of infusion rate, and long delays to reach steady state or excessively high microbubble concentrations can occur, reducing its clinical adoption.

Studies quantifying CEUS data frequently analyze four bolus-transit metrics: rise time (*RT*), mean transit time (*MTT*), peak intensity (*PI*), and area under the curve (*AUC*) as these measures provide insight into changes in microvascular perfusion (10, 51-54). These parameters have been utilized in several CEUS studies characterizing vascular dynamics in diabetic nephropathy (53), coronary artery disease (55), and various focal liver lesions (hepatocellular carcinoma, cholangiocarcinoma, liver metastases, etc.) (48, 56-58). Current clinical CEUS studies quantifying tumor blood flow have seen limited utility due to the lack of consistency in microbubble administration, imaging

parameters, and motion correction methods. Consequently, perfusion metrics observed across injections in many of these works lack the sensitivity necessary for practical use in the clinic for diagnosis or longitudinal evaluations. In **Chapter 2**, we describe a comprehensive protocol for CEUS perfusion quantification and evaluate the repeatability of these bolus-transit metrics in clinical CEUS examinations of liver lesions. This study establishes thresholds for identifying true physiological changes in vascularity over time from CEUS data and discusses the elimination of curve fitting when standardized data collection techniques are employed.

### 1.2.3 *Algorithm development and advanced techniques*

Image post-processing methods have been increasingly applied to enhance the visualization and interpretation of contrast-enhanced ultrasound (CEUS) data. Some of these approaches utilize quantitative metrics derived from CEUS data to aid visualization of blood-flow dynamics, including techniques such as parametric processing. Parametric processing extends traditional TIC analysis by performing perfusion-related calculations at the scale of individual image pixels (or small groups of pixels) rather than over a larger region of interest. Perfusion metrics are mapped to color values and overlaid on the ultrasound image, enabling assessment of spatial heterogeneity and improved delineated feature boundaries. In **Chapter 3**, we build on the findings of **Chapter 2** and we describe how parametric processing of clinical CEUS data quantifying vascular metrics present in the CEUS LI-RADS scheme can potentially improve diagnostic sensitivity and reduce operator-bias.

Although real-time evaluations of blood flow are a key feature of CEUS, several image processing techniques summarize microbubble activity throughout time, assessing relative vascular volume and allowing comparison of vasculature with differing flow rates or feeding vessels. Advances in ultrafast imaging and reconstruction have enabled super-resolution ultrasound techniques capable of localizing, tracking, and mapping individual microbubbles within micro vessels beyond the resolution limit of standard CEUS (59). These methods have shown promise for more precise evaluation of tumor perfusion (60-62), although their clinical translation in liver imaging remains limited due to respiratory motion and the relatively low volume rates achievable on current clinical systems with 3D ultrasound imaging. However, techniques such as maximum intensity projection (MIP) is one such technique to further aid visualization by accumulating the brightest pixel values

across a CEUS cine loop while still using standard bolus techniques and 2D imaging. Although not as highly resolved and sensitive as super-resolution, this process also emphasizes vascular architecture and spatial distribution of flow. Despite a simpler implementation, this technique is still highly sensitive to motion as any translation can result in smearing of microbubble signal in the image, requiring robust data collection protocols and advanced motion compensation algorithms. We utilized this technique in **Chapters 4 and 5** to capture the spatial extent of TTPL resulting from cavitation treatments in murine tumors.

### 1.2.4 *Treatment monitoring*

As a result of the complexity of the disease, influence of liver health, and wide variety of treatment options, monitoring of treatment efficacy is challenging. Localized therapies offer clearer treatment outcome metrics because their effects stem from direct intervention, while systemic treatments involve more complex and diffuse biological processes that make outcomes harder to interpret. HCC response to systemic therapy is typically assessed by measuring tumor size using the Response Evaluation Criteria in Solid Tumors (RECIST), or by evaluating the extent of residual arterialized tissue with modified RECIST (mRECIST) on either contrast-enhanced CT or contrast-enhanced MRI performed at intervals of at least three months (63). However, current methods are often unable to provide early indicators of treatment efficacy, contributing to the overall low response rates observed (64). In addition, the complexity, cost, and limited accessibility of contrast-enhanced CT and contrast-enhanced MRI restrict the feasibility of frequent imaging, limiting rigorous short-interval monitoring during therapy. Earlier identification of nonresponding tumors would enable clinicians to adjust treatment regimens sooner, potentially improving patient outcomes. Because tumor angiogenesis is a defining feature of cancer (65, 66), and all systemic therapies including current immunotherapy-based treatments directly influence the abnormal vascular architecture of HCC, earlier vascular-based biomarkers may offer a timelier assessment of therapeutic response. Researchers have applied quantitative CEUS analysis to explore how perfusion-related metrics correspond to therapeutic response in several clinical settings, including metastatic renal cell carcinoma (50, 67, 68), primary renal tumors (69), and liver metastases (48, 51). However, current attempts to use quantitative CEUS in clinical data lack consistency in microbubble delivery, image settings, and extracted perfusion metrics that have

limited outcomes of these works. Protocols and techniques described in **Chapters 2 and 3** aim to assist in establishing standardized clinical CEUS evaluations for systemic drug treatments of HCC.

## 1.3 THERAPEUTIC LEVERAGE OF ULTRASOUND AND MICROBUBBLES

### 1.3.1 *The tumor microenvironment acts as a barrier to systemic therapy*

The tumor microenvironment (TME) creates multiple barriers that impede effective drug delivery. Hypoxia is a major driver of these barriers, stimulating tumor cells and bone-marrow–derived myeloid cells to secrete high levels of vascular endothelial growth factor, platelet-derived growth factor, and other cytokines that promote the formation of structurally abnormal vasculature. These vessels grow in a highly irregular manner, exhibiting disordered three-dimensional branching, poor or absent smooth muscle and pericyte coverage, and disrupted basement membranes (70, 71). Although these vessels are excessively permeable, the combination of increased leakiness, chronic inflammation, and the near absence of functional lymphatic drainage leads to the accumulation of interstitial fluid within the tumor mass (72-74). This buildup elevates tumor interstitial fluid pressure (IFP), and because pressure gradients within tumors are largely uniform, convective transport becomes negligible, severely restricting movement of therapeutic agents across vessel walls (75-77). Larger therapeutics such as antibodies and nanoparticles can exploit the enhanced permeability and retention (EPR) effect to extravasate through hyperpermeable vessels and avoid lymphatic clearance, yet their diffusion remains limited, causing them to accumulate near blood vessels with minimal penetration into the tumor (78, 79). Even when drugs reach tumor cells, additional obstacles persist as agents must traverse cellular or nuclear membranes, and multidrug-resistant efflux pumps may expel them (80, 81). Beyond physical transport barriers, the TME also fosters immunosuppression through the release of inhibitory cytokines and the induction of regulatory T cells, further diminishing therapeutic efficacy (82-85).

### 1.3.2 *Microbubble cavitation dynamics and biological effects*

In therapeutic ultrasound, higher mechanical indices than those used diagnostically are applied, producing microbubble responses that transition from stable to inertial cavitation as acoustic pressure increases. Stable cavitation is defined by the appearance of sub- and ultra-harmonic emissions without substantial broadband noise (86), reflecting large bubble oscillations that persist

throughout the acoustic pulse. Once pressure exceeds a threshold, inertial cavitation emerges, characterized by elevated broadband noise driven by rapid bubble expansion and collapse that generate potent localized mechanical effects (87).

Cavitating microbubbles, particularly those undergoing inertial cavitation, exert potent mechanical forces on surrounding tissues, giving rise to a spectrum of biologically significant effects. These include transient increases in cell-membrane permeability (sonoporation), enhanced penetration of therapeutic agents through opening of cell-cell junctions, alteration of tumor vasculature, and broader modulation of the tumor microenvironment (88-91). Depending on the applied acoustic pressure and pulse characteristics, cavitation treatments have also been attributed to reductions in interstitial fluid pressure through the deformation of extracellular-matrix structures and decompression of collapsed micro vessels (92, 93). Cavitation-induced modulation of the TME has also been reported to facilitate immune-cell infiltration and release intact tumor-associated peptides that may support antigen presentation for immune-based therapies (94). We describe on-going work where we are investigating the role of cavitation treatments in immune response in **Chapter 6**. At higher acoustic pressures and large cycle pulses, microvascular injury such as endothelial damage, edema, and localized hemorrhage has been observed (95, 96). In addition to mechanical effects, microbubble oscillation and collapse can elevate local tissue temperature through thermoviscous absorption, offering opportunities for mild hyperthermia or activation of heat-sensitive agents (97-99). In **Chapter 4**, we further explore how microbubble cavitation under different acoustic conditions on a diagnostic scanner can influence the tumor microenvironment and enhance drug delivery.

### 1.3.3 *Cavitation-induced tumor vascular changes*

Under certain ultrasound conditions used to induce microbubble cavitation, tumors can exhibit a marked reduction in blood flow, often referred to as vascular shutdown or transient tumor perfusion loss (TTPL) (91, 93, 100, 101). This response appears to be tumor-specific, likely reflecting the vulnerability of small, immature, and structurally abnormal tumor vessels to cavitation-generated mechanical stresses (102). Although the precise mechanism remains unresolved, proposed drivers include platelet aggregation triggered by exposure of extravascular tissue factor or basement membrane, inadequate pericyte support, or the activation of

ceramide-mediated cell-death pathways (100, 103, 104). This phenomenon has primarily been reported in studies combining cavitation with systemic therapies, where enhanced vascular permeability or immune-microenvironment modulation may augment treatment efficacy. The dependence of TTPL on acoustic pressure may relate to intratumoral vessel heterogeneity as small vessels (<50 μm) have been shown to respond at pressures around 1 MPa, while larger vessels require substantially higher pressures (>2 MPa) to exhibit flow disturbances (105). Previous studies in this field have relied on custom single-element transducers built specifically for animal experiments, which lack clinical regulatory approval and are difficult to adapt for human use. In **Chapter 4** we demonstrate the first implementation of long cycle treatment pulses through a clinical scanner which allows for dynamic beamforming and steering, enhancing clinical translation. In **Chapter 5**, we investigate how acoustic pressure influences the spatial and temporal dynamics of this vascular response using CEUS.

### 1.3.4 *Theranostic potential of ultrasound microbubble cavitation treatments*

Contrast-enhanced ultrasound (CEUS) provides a unique opportunity for real-time monitoring during cavitation-based therapies because the same microbubble agents used for treatment also serve as imaging tracers. Despite this advantage, relatively few studies have incorporated CEUS to directly visualize cavitation-induced vascular effects as they occur, as these studies employ custom transducers to transmit cavitation treatments that are unable to simultaneously image. This capability is particularly important in cavitation treatments as many therapeutic protocols assume continuous microbubble recirculation into the tumor occurs, but cavitation-induced perfusion loss at higher acoustic pressures can significantly impact microbubble flow in tumor vessels. CEUS therefore offers a valuable feedback mechanism for assessing vascular status and guiding treatment parameters, or even in combination with cavitation-induced perfusion loss as a potential diagnostic scheme for HCCs. While passive cavitation detection is often used to monitor microbubble activity, inertial cavitation produces more complex vascular responses than broadband noise alone would suggest (106), underscoring the importance of imaging-based feedback in understanding and optimizing cavitation therapies.

## 1.4 RESEARCH OBJECTIVES

Facing the immense burden of liver cancer, the objective of this research is to improve the treatments of HCC and provide accurate monitoring of the outcomes with ultrasound and microbubbles. The works in this thesis outline a theranostic approach to HCC, by the development of quantitative tools with clinical CEUS data to cavitation treatments performed with clinically available technologies.

In **Chapter 2**, we establish a rigorous and repeatable CEUS framework for quantifying liver tumor perfusion that was much needed in this area. Clinical adoption of quantitative CEUS has been limited by inconsistent microbubble delivery, variable imaging parameters, and inadequate motion correction, all of which reduce repeatability for longitudinal monitoring and clinical adoption. Through standardized probe fixation, controlled bolus administration, and custom respiratory gating and motion compensation algorithms, we developed a comprehensive imaging and analysis protocol that yields highly repeatable bolus transit parameters from TIC analysis. We also assess the need for curve fitting when data collection is consistent, comparing extracted bolus perfusion metrics directly from TIC data and from a fitted lognormal curve.

Building on this rigorous and repeatable protocol, we implement the first quantitative version of CEUS LI RADS for HCC diagnosis in **Chapter 3**. Using patient data with confirmed HCC lesions (LI-RADS 5), we created an algorithm to quantify the two vascular features characteristic of HCC that are evaluated in CEUS LI-RADS: arterial phase hyperenhancement via rise time and washout via a term we titled relative degree of washout. In particular, the quantitative evaluation of washout from CEUS data was explored for the first time in this work. We illustrate how parametric processing enables synchronized region of interest manipulation and visualization of perfusion-based biomarkers, aiming to make significant strides toward computational CEUS assessment in clinical workflows that would lead to automated diagnosis.

In **Chapter 4**, we evaluate cavitation-based cancer therapies using clinically available microbubbles and a modified clinical ultrasound system, and we apply the quantitative CEUS tools we developed to assess resulting vascular changes. Importantly, this study employs the first use of

long (1000 cycle) pulses delivered by a clinical scanner for cavitation treatments. We explore the effect of two acoustic conditions and their effect on cavitation induced transient tumor perfusion loss (TTPL), drug extravasation via doxorubicin fluorescence, and changes to interstitial fluid pressure changes. We also describe a quantitative tool for assessing the degree of TTPL with maximum intensity projection time-area curve (MIP-TAC) analysis, a novel perfusion quantification technique that we developed, and how vascular changes to the tumor influence drug delivery. We demonstrate the limitations of PCD in describing cavitation-induced bioeffects and highlight the importance of real-time imaging feedback in cavitation treatments.

Motivated by our findings, in **Chapter 5** we examine how acoustic pressure shapes the spatial and temporal dynamics of TTPL. Using CEUS at multiple post treatment time points and our quantitative MIP TAC analysis, we characterize TTPL recovery over a previously unexplored sub hour timescale. We assess cavitation-induced damage with histological analyses to interpret the distinct vascular responses observed across pressure conditions and provide further insights towards a mechanistic understanding of TTPL.

In **Chapter 6** we describe on-going work investigating how ultrasound cavitation influences antitumor immunity, both alone and in combination with immune checkpoint inhibitors. This work provides the first demonstration that a single cavitation pulse can induce TTPL and explores whether TTPL susceptibility predicts ICI responsiveness. Using a transgenic mouse model that develops both HCC and intrahepatic cholangiocarcinoma (ICC) on a steatotic background, we evaluate these cavitation effects in a clinically relevant model and immune environment.

Finally, in **Chapter 7** we conclude this thesis with a summary of accomplishments and discuss future directions of this work. Through these investigations, we aim to create highly translatable therapies using ultrasound and microbubbles to address the growing challenge imposed by HCCs.

## 1.5 REFERENCES

1.Kinsey E, Lee HM. Management of Hepatocellular Carcinoma in 2024: The Multidisciplinary Paradigm in an Evolving Treatment Landscape. Cancers. 2024;16(3).
2.Brown RS, Jr., Lake JR. The survival impact of liver transplantation in the MELD era, and the future for organ allocation and distribution. American journal of transplantation : official journal of the American Society of Transplantation and the American Society of Transplant Surgeons. 2005;5(2):203-4.

3.Santucci C, Carioli G, Bertuccio P, Malvezzi M, Pastorino U, Boffetta P, et al. Progress in cancer mortality, incidence, and survival: a global overview. European journal of cancer prevention : the official journal of the European Cancer Prevention Organisation (ECP). 2020;29(5):367-81.
4.Kulik L, El-Serag HB. Epidemiology and Management of Hepatocellular Carcinoma. Gastroenterology. 2019;156(2):477-91.e1.
5.Carr RM, Oranu A, Khungar V. Nonalcoholic Fatty Liver Disease: Pathophysiology and Management. Gastroenterology clinics of North America. 2016;45(4):639-52.
6.Qiu S, Cai J, Yang Z, He X, Xing Z, Zu J, et al. Trends in Hepatocellular Carcinoma Mortality Rates in the US and Projections Through 2040. JAMA network open. 2024;7(11):e2445525.
7.Polpichai N, Maneenil C, Danpanichkul P, Rattananukrom C, Choudhury A, Wong YJ, et al. Current and new strategies for hepatocellular carcinoma surveillance. Gastroenterology report. 2025;13:goaf045.
8.Tanaka H. Current role of ultrasound in the diagnosis of hepatocellular carcinoma. Journal of medical ultrasonics (2001). 2020;47(2):239-55.
9.Averkiou MA, Bruce MF, Powers JE, Sheeran PS, Burns PN. Imaging Methods for Ultrasound Contrast Agents. Ultrasound in medicine & biology. 2020;46(3):498-517.
10.Averkiou MA, Juang EK, Gallagher MK, Cuevas MA, Wilson SR, Barr RG, et al. Evaluation of the Reproducibility of Bolus Transit Quantification With Contrast-Enhanced Ultrasound Across Multiple Scanners and Analysis Software Packages-A Quantitative Imaging Biomarker Alliance Study. Investigative radiology. 2020;55(10):643-56.
11.Wilson SR, Burns PN, Kono Y. Contrast-Enhanced Ultrasound of Focal Liver Masses: A Success Story. Ultrasound in medicine & biology. 2020;46(5):1059-70.
12.Cunha GM, Fowler KJ, Roudenko A, Taouli B, Fung AW, Elsayes KM, et al. How to Use LI-RADS to Report Liver CT and MRI Observations. Radiographics : a review publication of the Radiological Society of North America, Inc. 2021;41(5):1352-67.
13.Chernyak V, Fowler KJ, Do RKG, Kamaya A, Kono Y, Tang A, et al. LI-RADS: Looking Back, Looking Forward. Radiology. 2023;307(1):e222801.
14.Mitchell DG, Bruix J, Sherman M, Sirlin CB. LI-RADS (Liver Imaging Reporting and Data System): summary, discussion, and consensus of the LI-RADS Management Working Group and future directions. Hepatology (Baltimore, Md). 2015;61(3):1056-65.
15.Bartolotta TV, Terranova MC, Gagliardo C, Taibbi A. CEUS LI-RADS: a pictorial review. Insights into imaging. 2020;11(1):9.
16.Möller K, Görg C, Krix M, Jenssen C, Dong Y, Cui XW, et al. Washout on Contrast-Enhanced Ultrasound of Benign Focal Liver Lesions-A Review on Its Frequency and Possible Causes. Diagnostics (Basel, Switzerland). 2025;15(8).
17.Burak KW, Douglas L, Congly SE. Comparing Magnetic Resonance Imaging and Contrast-Enhanced Ultrasound (CEUS) for the Characterization of Nodules Found on Hepatocellular Carcinoma Surveillance: CEUS is Our Clear Choice. Journal of ultrasound in medicine : official journal of the American Institute of Ultrasound in Medicine. 2023;42(6):1175-80.
18.Hu J, Bhayana D, Burak KW, Wilson SR. Resolution of indeterminate MRI with CEUS in patients at high risk for hepatocellular carcinoma. Abdominal radiology (New York). 2020;45(1):123-33.
19.Rhim H, Lim HK. Radiofrequency ablation of hepatocellular carcinoma: pros and cons. Gut and liver. 2010;4 Suppl 1(Suppl 1):S113-8.
20.Song KD. Percutaneous cryoablation for hepatocellular carcinoma. Clinical and molecular hepatology. 2016;22(4):509-15.
21.Kallini JR, Gabr A, Salem R, Lewandowski RJ. Transarterial Radioembolization with Yttrium-90 for the Treatment of Hepatocellular Carcinoma. Advances in therapy. 2016;33(5):699-714.
22.Kotsifa E, Vergadis C, Vailas M, Machairas N, Kykalos S, Damaskos C, et al. Transarterial Chemoembolization for Hepatocellular Carcinoma: Why, When, How? Journal of personalized medicine. 2022;12(3).
23.Belghiti J, Kianmanesh R. Surgical treatment of hepatocellular carcinoma. HPB : the official journal of the International Hepato Pancreato Biliary Association. 2005;7(1):42-9.
24.Cho YK, Kim JK, Kim WT, Chung JW. Hepatic resection versus radiofrequency ablation for very early stage hepatocellular carcinoma: a Markov model analysis. Hepatology (Baltimore, Md). 2010;51(4):1284-90.
25.Sotiropoulos GC, Lang H, Frilling A, Molmenti EP, Paul A, Nadalin S, et al. Resectability of hepatocellular carcinoma: evaluation of 333 consecutive cases at a single hepatobiliary specialty center and systematic review of the literature. Hepato-gastroenterology. 2006;53(69):322-9.

26.de'Angelis N, Landi F, Carra MC, Azoulay D. Managements of recurrent hepatocellular carcinoma after liver transplantation: A systematic review. World journal of gastroenterology. 2015;21(39):11185-98.
27.Xu Z, Khokhlova TD, Cho CS, Khokhlova VA. Histotripsy: A Method for Mechanical Tissue Ablation with Ultrasound. Annual review of biomedical engineering. 2024;26(1):141-67.
28.Xu Z, Hall TL, Vlaisavljevich E, Lee FT, Jr. Histotripsy: the first noninvasive, non-ionizing, non-thermal ablation technique based on ultrasound. International journal of hyperthermia : the official journal of European Society for Hyperthermic Oncology, North American Hyperthermia Group. 2021;38(1):561-75.
29.Queen H, Ferris SF, Cho CS, Ganguly A. The Emerging Role of Histotripsy in Liver Cancer Treatment: A Scoping Review. Cancers. 2025;17(6).
30.Feng MY, Chan LL, Chan SL. Drug Treatment for Advanced Hepatocellular Carcinoma: First-Line and Beyond. Current oncology (Toronto, Ont). 2022;29(8):5489-507.
31.Peterson C, Denlinger N, Yang Y. Recent Advances and Challenges in Cancer Immunotherapy. Cancers. 2022;14(16).
32.El-Khoueiry AB, Sangro B, Yau T, Crocenzi TS, Kudo M, Hsu C, et al. Nivolumab in patients with advanced hepatocellular carcinoma (CheckMate 040): an open-label, non-comparative, phase 1/2 dose escalation and expansion trial. Lancet (London, England). 2017;389(10088):2492-502.
33.Yu Y. Molecular classification and precision therapy of cancer: immune checkpoint inhibitors. Frontiers of medicine. 2018;12(2):229-35.
34.Stride E. Physical Principles of Microbubbles for Ultrasound Imaging and Therapy. Cerebrovascular Diseases. 2009;27(Suppl. 2):1-13.
35.Leighton TG. The acoustic bubble. London: Academic Press; 1994.
36.Simpson DH, Chin CT, Burns PN. Pulse inversion Doppler: a new method for detecting nonlinear echoes from microbubble contrast agents. IEEE transactions on ultrasonics, ferroelectrics, and frequency control. 1999;46(2):372-82.
37.Brock-Fisher GA, Poland MD, Rafter PG. Means for increasing sensitivity in non-linear ultrasound imaging systems. Journal of the Acoustical Society of America. 1997;101:3240.
38.Mor-Avi V, Caiani EG, Collins KA, Korcarz CE, Bednarz JE, Lang RM. Combined assessment of myocardial perfusion and regional left ventricular function by analysis of contrast-enhanced power modulation images. Circulation. 2001;104(3):352-7.
39.Phillips PJ. Contrast pulse sequences (CPS): imaging nonlinear microbubbles. 2001 IEEE Ultrasonics Symposium Proceedings An International Symposium (Cat No01CH37263). 2001;2:1739-45 vol.2.
40.Lampaskis M, Averkiou M. Investigation of the relationship of nonlinear backscattered ultrasound intensity with microbubble concentration at low MI. Ultrasound in medicine & biology. 2010;36(2):306-12.
41.Bartolotta TV, Taibbi A, Midiri M, Lagalla R. Contrast-enhanced ultrasound of hepatocellular carcinoma: where do we stand? Ultrasonography (Seoul, Korea). 2019;38(3):200-14.
42.Christofides D, Leen E, Averkiou M. Automatic respiratory gating for contrast ultrasound evaluation of liver lesions. IEEE transactions on ultrasonics, ferroelectrics, and frequency control. 2014;61(1):25-32.
43.Christofides D, Leen EL, Averkiou MA. Improvement of the accuracy of liver lesion DCEUS quantification with the use of automatic respiratory gating. European radiology. 2016;26(2):417-24.
44.Tiyarattanachai T, Turco S, Eisenbrey JR, Wessner CE, Medellin-Kowalewski A, Wilson S, et al. A Comprehensive Motion Compensation Method for In-Plane and Out-of-Plane Motion in Dynamic Contrast-Enhanced Ultrasound of Focal Liver Lesions. Ultrasound in medicine & biology. 2022;48(11):2217-28.
45.Wan P, Chen F, Shao W, Liu C, Zhang Y, Wen B, et al. Irregular Respiratory Motion Compensation for Liver Contrast-Enhanced Ultrasound via Transport-Based Motion Estimation. IEEE transactions on ultrasonics, ferroelectrics, and frequency control. 2021;68(4):1117-30.
46.Averkiou M, Lampaskis M, Kyriakopoulou K, Skarlos D, Klouvas G, Strouthos C, et al. Quantification of tumor microvascularity with respiratory gated contrast enhanced ultrasound for monitoring therapy. Ultrasound in medicine & biology. 2010;36(1):68-77.
47.Strouthos C, Lampaskis M, Sboros V, McNeilly A, Averkiou M. Indicator dilution models for the quantification of microvascular blood flow with bolus administration of ultrasound contrast agents. IEEE transactions on ultrasonics, ferroelectrics, and frequency control. 2010;57(6):1296-310.
48.El Kaffas A, Sigrist RMS, Fisher G, Bachawal S, Liau J, Wang H, et al. Quantitative Three-Dimensional Dynamic Contrast-Enhanced Ultrasound Imaging: First-In-Human Pilot Study in Patients with Liver Metastases. Theranostics. 2017;7(15):3745-58.
49.Hudson JM, Karshafian R, Burns PN. Quantification of flow using ultrasound and microbubbles: a disruption replenishment model based on physical principles. Ultrasound in medicine & biology. 2009;35(12):2007-20.

50. Williams R, Hudson JM, Lloyd BA, Sureshkumar AR, Lueck G, Milot L, et al. Dynamic microbubble contrast-enhanced US to measure tumor response to targeted therapy: a proposed clinical protocol with results from renal cell carcinoma patients receiving antiangiogenic therapy. Radiology. 2011;260(2):581-90.
51. El Kaffas A, Hoogi A, Zhou J, Durot I, Wang H, Rosenberg J, et al. Spatial Characterization of Tumor Perfusion Properties from 3D DCE-US Perfusion Maps are Early Predictors of Cancer Treatment Response. Scientific reports. 2020;10(1):6996.
52. Lassau N, Coiffier B, Faivre L, Benatsou B, Bidault S, Girard E, et al. Study of Intrapatient Variability and Reproducibility of Quantitative Tumor Perfusion Parameters Evaluated With Dynamic Contrast-Enhanced Ultrasonography. Investigative radiology. 2017;52(3):148-54.
53. Lin L, Wang Y, Yan L, Li N, Tian X, Li Q, et al. Interobserver reproducibility of contrast-enhanced ultrasound in diabetic nephropathy. The British journal of radiology. 2022;95(1129):20210189.
54. Ryu H, Kim JH, Lee S, Han JK. Therapeutic response monitoring after targeted therapy in an orthotopic rat model of hepatocellular carcinoma using contrast-enhanced ultrasound: Focusing on inter-scanner, and inter-operator reproducibility. PloS one. 2020;15(12):e0244304.
55. Li Y, Chahal N, Senior R, Tang MX. Reproducible Computer-Assisted Quantification of Myocardial Perfusion with Contrast-Enhanced Ultrasound. Ultrasound in medicine & biology. 2017;43(10):2235-46.
56. Krolak C, Dighe M, Clark A, Shumaker M, Yeung R, Barr RG, et al. Quantification of Hepatocellular Carcinoma Vascular Dynamics With Contrast-Enhanced Ultrasound for LI-RADS Implementation. Investigative radiology. 2024;59(4):337-44.
57. Krolak C, Wei A, Shumaker M, Dighe M, Averkiou M. A Comprehensive and Repeatable Contrast-Enhanced Ultrasound Quantification Approach for Clinical Evaluations of Tumor Blood Flow. Investigative radiology. 2025;60(4):281-90.
58. Wildner D, Pfeifer L, Goertz RS, Bernatik T, Sturm J, Neurath MF, et al. Dynamic contrast-enhanced ultrasound (DCE-US) for the characterization of hepatocellular carcinoma and cholangiocellular carcinoma. Ultraschall in der Medizin (Stuttgart, Germany : 1980). 2014;35(6):522-7.
59. Christensen-Jeffries K, Couture O, Dayton PA, Eldar YC, Hynynen K, Kiessling F, et al. Super-resolution Ultrasound Imaging. Ultrasound in medicine & biology. 2020;46(4):865-91.
60. Jung EM, Weber MA, Jung F, Stroszczynski C. Super-resolution contrast-enhanced ultrasound (SR-CEUS) in solid organs. RoFo : Fortschritte auf dem Gebiete der Rontgenstrahlen und der Nuklearmedizin. 2026.
61. Kaiser U, Vehling-Kaiser U, Kück F, Gilanschah M, Jung F, Jung EM. Super-Resolution Contrast-Enhanced Ultrasound Examination Down to the Microvasculature Enables Quantitative Analysis of Liver Lesions: First Results. Life (Basel, Switzerland). 2025;15(7).
62. Lin F, Shelton SE, Espíndola D, Rojas JD, Pinton G, Dayton PA. 3-D Ultrasound Localization Microscopy for Identifying Microvascular Morphology Features of Tumor Angiogenesis at a Resolution Beyond the Diffraction Limit of Conventional Ultrasound. Theranostics. 2017;7(1):196-204.
63. Faccia M, Garcovich M, Ainora ME, Riccardi L, Pompili M, Gasbarrini A, et al. Contrast-Enhanced Ultrasound for Monitoring Treatment Response in Different Stages of Hepatocellular Carcinoma. Cancers. 2022;14(3).
64. Pinter M, Scheiner B, Peck-Radosavljevic M. Immunotherapy for advanced hepatocellular carcinoma: a focus on special subgroups. Gut. 2021;70(1):204-14.
65. Carmeliet P, Jain RK. Angiogenesis in cancer and other diseases. Nature. 2000;407(6801):249-57.
66. Majidpoor J, Mortezaee K. Angiogenesis as a hallmark of solid tumors - clinical perspectives. Cellular oncology (Dordrecht). 2021;44(4):715-37.
67. Hudson JM, Williams R, Lloyd B, Atri M, Kim TK, Bjarnason G, et al. Improved flow measurement using microbubble contrast agents and disruption-replenishment: clinical application to tumour monitoring. Ultrasound in medicine & biology. 2011;37(8):1210-21.
68. Lassau N, Koscielny S, Albiges L, Chami L, Benatsou B, Chebil M, et al. Metastatic renal cell carcinoma treated with sunitinib: early evaluation of treatment response using dynamic contrast-enhanced ultrasonography. Clinical cancer research : an official journal of the American Association for Cancer Research. 2010;16(4):1216-25.
69. Hudson JM, Bailey C, Atri M, Stanisz G, Milot L, Williams R, et al. The prognostic and predictive value of vascular response parameters measured by dynamic contrast-enhanced-CT, -MRI and -US in patients with metastatic renal cell carcinoma receiving sunitinib. European radiology. 2018;28(6):2281-90.
70. Munn LL. Aberrant vascular architecture in tumors and its importance in drug-based therapies. Drug discovery today. 2003;8(9):396-403.
71. Narang AS, Varia S. Role of tumor vascular architecture in drug delivery. Advanced drug delivery reviews. 2011;63(8):640-58.

72. Jain RK, Fenton BT. Intratumoral lymphatic vessels: a case of mistaken identity or malfunction? Journal of the National Cancer Institute. 2002;94(6):417-21.
73. Wagner M, Wiig H. Tumor Interstitial Fluid Formation, Characterization, and Clinical Implications. Frontiers in oncology. 2015;5:115.
74. Wiig H, Swartz MA. Interstitial fluid and lymph formation and transport: physiological regulation and roles in inflammation and cancer. Physiological reviews. 2012;92(3):1005-60.
75. Jain RK. Determinants of tumor blood flow: a review. Cancer research. 1988;48(10):2641-58.
76. Jain RK. Physiological barriers to delivery of monoclonal antibodies and other macromolecules in tumors. Cancer research. 1990;50(3 Suppl):814s-9s.
77. Jain RK. Transport of molecules, particles, and cells in solid tumors. Annual review of biomedical engineering. 1999;1:241-63.
78. Arias JL. Drug targeting strategies in cancer treatment: an overview. Mini reviews in medicinal chemistry. 2011;11(1):1-17.
79. Maeda H. Tumor-selective delivery of macromolecular drugs via the EPR effect: background and future prospects. Bioconjugate chemistry. 2010;21(5):797-802.
80. Merlin JL, Marchal S, Ramacci C, Notter D, Vigneron C. Antiproliferative activity of thermosensitive liposome-encapsulated doxorubicin combined with 43 degrees C hyperthermia in sensitive and multidrug-resistant MCF-7 cells. European journal of cancer (Oxford, England : 1990). 1993;29a(16):2264-8.
81. Monsky WL, Kruskal JB, Lukyanov AN, Girnun GD, Ahmed M, Gazelle GS, et al. Radio-frequency ablation increases intratumoral liposomal doxorubicin accumulation in a rat breast tumor model. Radiology. 2002;224(3):823-9.
82. Gerlini G, Tun-Kyi A, Dudli C, Burg G, Pimpinelli N, Nestle FO. Metastatic melanoma secreted IL-10 down-regulates CD1 molecules on dendritic cells in metastatic tumor lesions. The American journal of pathology. 2004;165(6):1853-63.
83. Sica A, Bronte V. Altered macrophage differentiation and immune dysfunction in tumor development. The Journal of clinical investigation. 2007;117(5):1155-66.
84. Thomas DA, Massagué J. TGF-beta directly targets cytotoxic T cell functions during tumor evasion of immune surveillance. Cancer cell. 2005;8(5):369-80.
85. Turk MJ, Guevara-Patiño JA, Rizzuto GA, Engelhorn ME, Sakaguchi S, Houghton AN. Concomitant tumor immunity to a poorly immunogenic melanoma is prevented by regulatory T cells. The Journal of experimental medicine. 2004;200(6):771-82.
86. Bader KB, Holland CK. Gauging the likelihood of stable cavitation from ultrasound contrast agents. Physics in medicine and biology. 2013;58(1):127-44.
87. Keller SB, Sheeran PS, Averkiou MA. Cavitation Therapy Monitoring of Commercial Microbubbles With a Clinical Scanner. IEEE transactions on ultrasonics, ferroelectrics, and frequency control. 2021;68(4):1144-54.
88. De Cock I, Zagato E, Braeckmans K, Luan Y, de Jong N, De Smedt SC, et al. Ultrasound and microbubble mediated drug delivery: acoustic pressure as determinant for uptake via membrane pores or endocytosis. Journal of controlled release : official journal of the Controlled Release Society. 2015;197:20-8.
89. Goertz DE, Todorova M, Mortazavi O, Agache V, Chen B, Karshafian R, et al. Antitumor effects of combining docetaxel (taxotere) with the antivascular action of ultrasound stimulated microbubbles. PloS one. 2012;7(12):e52307.
90. Ho Y-J, Wang T-C, Fan C-H, Yeh C-K. Spatially Uniform Tumor Treatment and Drug Penetration by Regulating Ultrasound with Microbubbles. ACS Applied Materials & Interfaces. 2018;10(21):17784-91.
91. Keller SB, Suo D, Wang YN, Kenerson H, Yeung RS, Averkiou MA. Image-Guided Treatment of Primary Liver Cancer in Mice Leads to Vascular Disruption and Increased Drug Penetration. Frontiers in pharmacology. 2020;11:584344.
92. Keller SB, Averkiou MA. The Role of Ultrasound in Modulating Interstitial Fluid Pressure in Solid Tumors for Improved Drug Delivery. Bioconjugate chemistry. 2022;33(6):1049-56.
93. Krolak C, De Koninck L, Gu S, Wang YN, Powers JE, Averkiou M. Ultrasound cavitation therapy: inducing tumor drug delivery and blood flow changes with clinical ultrasound tools. Journal of controlled release : official journal of the Controlled Release Society. 2026;393:114748.
94. Hu S, Zhang X, Unger M, Patties I, Melzer A, Landgraf L. Focused Ultrasound-Induced Cavitation Sensitizes Cancer Cells to Radiation Therapy and Hyperthermia. Cells. 2020;9(12):2595.
95. He Y, Yu M, Wang J, Xi F, Zhong J, Yang Y, et al. Improving the Therapeutic Effect of Ultrasound Combined With Microbubbles on Muscular Tumor Xenografts With Appropriate Acoustic Pressure. Frontiers in pharmacology. 2020;Volume 11 - 2020.

96. Hwang JH, Tu J, Brayman AA, Matula TJ, Crum LA. Correlation between inertial cavitation dose and endothelial cell damage in vivo. Ultrasound in medicine & biology. 2006;32(10):1611-9.
97. Clark A, Bonilla S, Suo D, Shapira Y, Averkiou M. Microbubble-Enhanced Heating: Exploring the Effect of Microbubble Concentration and Pressure Amplitude on High-Intensity Focused Ultrasound Treatments. Ultrasound in medicine & biology. 2021;47(8):2296-309.
98. Juang EK, De Koninck LH, Vuong KS, Gnanaskandan A, Hsiao C-T, Averkiou MA. Controlled Hyperthermia With High-Intensity Focused Ultrasound and Ultrasound Contrast Agent Microbubbles in Porcine Liver. Ultrasound in medicine & biology. 2023;49(8):1852-60.
99. Yudina A, de Smet M, Lepetit-Coiffé M, Langereis S, Van Ruijssevelt L, Smirnov P, et al. Ultrasound-mediated intracellular drug delivery using microbubbles and temperature-sensitive liposomes. Journal of Controlled Release. 2011;155(3):442-8.
100. Hu X, Kheirolomoom A, Mahakian LM, Beegle JR, Kruse DE, Lam KS, et al. Insonation of targeted microbubbles produces regions of reduced blood flow within tumor vasculature. Investigative radiology. 2012;47(7):398-405.
101. Liu Z, Gao S, Zhao Y, Li P, Liu J, Li P, et al. Disruption of tumor neovasculature by microbubble enhanced ultrasound: a potential new physical therapy of anti-angiogenesis. Ultrasound in medicine & biology. 2012;38(2):253-61.
102. Wang J, Zhao Z, Shen S, Zhang C, Guo S, Lu Y, et al. Selective depletion of tumor neovasculature by microbubble destruction with appropriate ultrasound pressure. International journal of cancer. 2015;137(10):2478-91.
103. El Kaffas A, Gangeh MJ, Farhat G, Tran WT, Hashim A, Giles A, et al. Tumour Vascular Shutdown and Cell Death Following Ultrasound-Microbubble Enhanced Radiation Therapy. Theranostics. 2018;8(2):314-27.
104. Zhao X, Pellow C, Goertz DE. Intravital imaging and cavitation monitoring of antivascular ultrasound in tumor microvasculature. Theranostics. 2023;13(1):250-66.
105. Zhao X, Wright A, Goertz DE. An optical and acoustic investigation of microbubble cavitation in small channels under therapeutic ultrasound conditions. Ultrasonics sonochemistry. 2023;93:106291.
106. Wu Q, Gray M, Smith CAB, Bau L, Cleveland RO, Coussios C, et al. Challenges in classifying cavitation: Correlating high-speed optical imaging and passive acoustic mapping of cavitation dynamics. The Journal of the Acoustical Society of America. 2024;156(5):3608-20.

# Chapter 2. A COMPREHENSIVE AND REPEATABLE CONTRAST-ENHANCED ULTRASOUND (CEUS) QUANTIFICATION APPROACH FOR CLINICAL EVALUATIONS OF TUMOR BLOOD FLOW

Connor Krolak, Angela Wei, Marissa Shumaker, Manjiri Dighe, Michalakis Averkiou

*Investigative Radiology. 2025 Apr 1;60(4):281-290.*

**Abstract**

*Objective:* The aim of this study is to define a comprehensive and repeatable contrast-enhanced ultrasound (CEUS) imaging protocol and analysis method to quantitatively assess lesional blood flow. Easily repeatable CEUS evaluations are essential for longitudinal treatment monitoring. The quantification method described here aims to provide a structure for future clinical studies.

*Materials and Methods:* This retrospective analysis study included liver CEUS studies in 80 patients, 40 of which contained lesions (primarily hepatocellular carcinoma, N=28). Each patient was given at least 2 injections of a microbubble contrast agent and 60 second continuous loops were acquired for each injection to enable evaluation of repeatability. For each bolus injection, 1.2 mL of contrast was delivered while continuous, stationary scanning was performed. Automated respiratory gating and motion compensation algorithms dealt with breathing motion. Similar in size regions of interest (ROI) were drawn around the lesion and liver parenchyma, and time-intensity curves (TIC) with linearized image data were generated. Four bolus transit parameters, rise time (*RT*), mean transit time (*MTT*), peak intensity (*PI*), and area under the curve (*AUC*) were extracted either directly from the actual TIC data or from a lognormal distribution curve fitted to the TIC. Inter-injection repeatability for each parameter was evaluated with coefficient of variation (COV). A 95% confidence interval was calculated for all fitted lognormal distribution curve coefficient of determination ($R^2$) values which serves as a data quality metric. One-sample t-tests were performed between values obtained from injection pairs and between the fitted lognormal distribution curve and direct extraction from the TIC calculation methods to establish injection independence and measurement precision respectively.

*Results:* Average inter-injection COV with both the fitted curve and direct calculation of *RT* and *MTT* were less than 21% while *PI* and *AUC* were less than 40% for lesion and parenchyma ROIs. The 95% confidence interval for the $R^2$ value of all fitted lognormal curves was [0.95, 0.96]. The one sample t-test for inter-injection value difference showed no significant differences, indicating there was no relationship between the order of the repeated bolus injections and the resulting parameters. The one sample t-test between the values from the fitted lognormal distribution curve and the direct extraction from the TIC calculation found no statistically significant differences ($\alpha = 0.05$) for all perfusion-related parameters except lesion and parenchyma *PI* and lesion *MTT*.

*Conclusions:* The scanning protocol and analysis method outlined and validated in this study provide easily repeatable quantitative evaluations of lesional blood flow with bolus transit parameters in CEUS data which were not available before. With vital features such as probe stabilization ideally performed with an articulated arm and an automated respiratory gating algorithm, we were able to achieve inter-injection repeatability of blood flow parameters which are comparable or surpass levels currently established for clinical 2D CEUS scans. Similar values and inter-injection repeatability were achieved between calculations from a fitted curve or directly from the data. This demonstrated not only the strength of the protocol to generate TICs with minimal noise, but also suggests that curve fitting might be avoided for a more standardized approach. Utilizing the imaging protocol and analysis method defined in this study, we aim for this methodology to potentially assist clinicians to assess true perfusion changes for treatment monitoring with CEUS in longitudinal studies.

## 2.1 INTRODUCTION

With a rapidly growing field of tumor therapies, particularly with systemic treatments such as immune checkpoint inhibitors (ICIs), early evaluation of tumor response is critical for improving patient outcomes. Currently, evaluation of tumor therapies in malignant lesions like hepatocellular carcinoma (HCC) rely on the modified Response Evaluation Criteria in Solid Tumors (mRECIST), which qualitatively evaluates tumor size and arterial enhancement with computed tomography (CT) or magnetic resonance imaging (MRI) (1). However, CT and MRI have notable disadvantages such as ionizing radiation and cost that limit frequent use for detection of early response. Additionally, and most important, their use of contrast agents which pass into the tissue interstitium limits their ability to quantify blood flow.

Contrast-enhanced ultrasound (CEUS) is an ideal alternative to evaluate tumor vasculature as microbubble contrast agents for ultrasound are pure blood pool agents comprised of tiny inert gas bubbles measuring 1-10$\mu$m in diameter. CEUS is also unique in that it has high temporal resolution, ease of use, and is safe and well tolerated (2-4). Accurate quantification of tumor blood flow with CEUS during the progression or regression of tumor angiogenesis would provide clinicians with the necessary metrics for frequent surveillance of tumors. Quantification of perfusion with CEUS evaluates image intensity throughout a video loop from a fixed plane. Temporal dynamics of contrast intensity within the tumor and surrounding organ are recorded to generate a time-intensity curve (TIC), which is then fitted to an indicator dilution model (5) mostly for reducing noise from the data and parameters related to blood flow and volume are extracted. Four of these bolus transit parameters explored in many quantitative CEUS studies (3, 6-14) are rise time (*RT*), mean transit time (*MTT*), peak intensity (*PI*), and area under the curve (*AUC*). Other parameters that related to the 4 listed above have also been suggested. Evaluation of these perfusion-related parameters over time could allow for quantitative evaluations of blood flow changes.

There have been a number of promising studies regarding quantification of perfusion-related parameters extracted from CEUS data, but lack of standardization and ambiguous measures of repeatability have limited clinical translation of these techniques. Various quantitative CEUS

clinical studies have been performed to characterize vascular dynamics in diabetic nephropathy (11), coronary artery disease (15), and various focal liver lesions (hepatocellular carcinoma, cholangiocarcinoma, liver metastases, etc.) (9, 13, 16, 17). Multiple groups have also developed advanced custom analysis software (8, 17-19) to perform quantitative evaluations of clinical CEUS data. Several investigators have quantified CEUS data to assess how changes in perfusion-related parameters relate to treatment outcomes in metastatic renal cell carcinoma (14, 20, 21), renal masses (22), and liver metastases (8, 9). Lassau et al. (18) have also investigated outcomes of antiangiogenic therapies in a large array of solid tumors (metastatic breast cancer, melanoma, renal cell carcinoma, colon cancer, gastrointestinal stromal tumors, and hepatocellular carcinoma) in comparison with quantitative perfusion-related CEUS parameters.

In an attempt to build confidence on CEUS quantification metrics, investigators have evaluated the repeatability and reproducibility of various perfusion metrics. As a note, repeatability refers to the likelihood that the same result is found when repeating a measurement whereas reproducibility refers to the ability that a different operator finds the same result. Inter-observer reproducibility (a metric combining user experience and subject variance) has been reported previously (11, 15) and intensity-based parameters were found to have the greatest intraclass correlation coefficients in these studies. Lassau et al. (10) measured bolus transit parameters with 2 CEUS scans per patient and with coefficient of variability (COV) measurements ranging from 53% to 87%, and found *MTT* to be the most reproducible but *AUC* to be the most predictive of response. Williams et al. (14) found that COV of parameters from repeated destruction measurements on the same plane to be 15%, while the bolus measurement inter-injection median percent difference ranged from 36% to 70%. El-Kaffas et al. (9) measured concordance correlation coefficient (CCC) using destruction replenishment (ranging from 0.95 to 0.97) and bolus techniques (ranging from 0.3 to 0.84), and found *AUC* and peak enhancement to be the most repeatable. Despite the significant contributions these studies have generated towards CEUS quantification in clinical data, the presented findings varied greatly from each other in terms of the approach and the evaluated metrics, and most importantly measured differing degrees of moderate repeatability.

Therefore, our objective in this study is to establish a comprehensive, standardized, and reproducible CEUS imaging protocol and analysis technique for the evaluation of liver tumor

perfusion, and with the prospect to further adjust and expand them in other tumors in the future. By stabilizing the transducer with an articulated arm and using a simple bolus delivery method in tandem with a simple scanning protocol and analysis, CEUS data from liver scans in 80 patients were collected and evaluated. We implemented automated respiratory motion compensation techniques and objective TIC analysis on linearized data with and without a fitted lognormal distribution curve and evaluated four significant bolus transit parameters (*RT*, *MTT*, *PI*, and *AUC*). Inter-injection repeatability was evaluated through COV where ranges were found to be comparable or better than those reported in current literature, reflecting the very accurate and highly repeatable results achieved in this study.

## 2.2 Materials and Methods

### 2.2.1 *Patient Population*

Our patient population was collected retrospectively from multiple institutional review board approved studies. A majority were collected from April 2021 to June 2022 (IRB ID: STUDY00012711), but others were included from previously published studies (6, 23-26). Patients with at least two CEUS loops each with the following criteria were included: (1) the scanning was stationary with only limited probe motion, (2) loop duration was at least 60s in order to capture data beyond the peak of the bolus (at least 50% decrease in magnitude from peak intensity), and (3) linearized data (removed logarithmic compression) was available for all loops. Exclusion criteria were: (1) poor depth penetration (not being able to image the tumor due to depth dependent attenuation), (2) loop duration shorter than 60s or that does not capture the peak of the portal phase, (3) probe movement that resulted in loss of the image plane, and (4) different scanner settings between injections (**Fig. 2.1**).

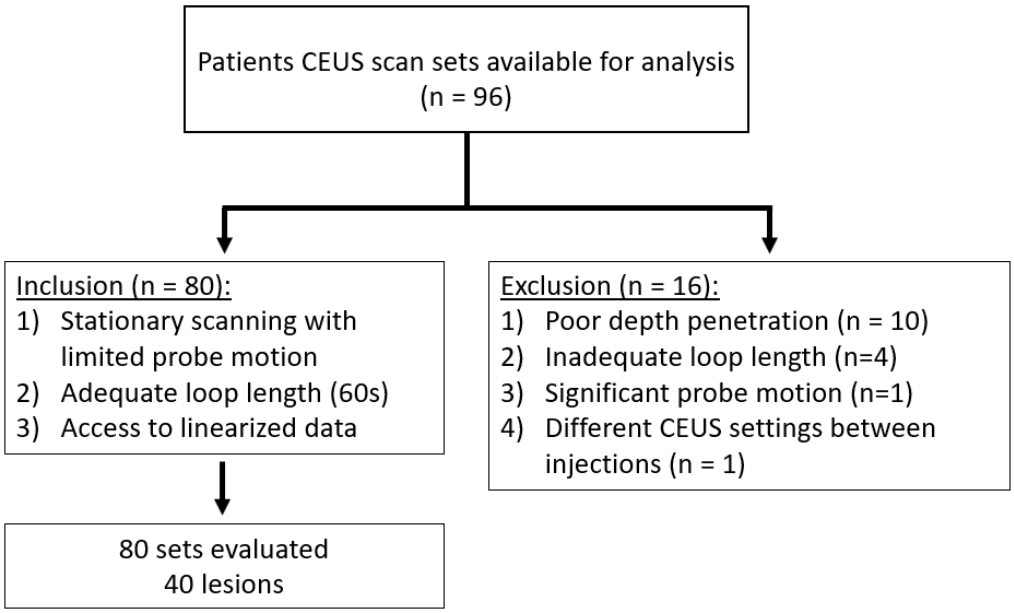


**Fig. 2.1**: A flowchart describing patient inclusion and exclusion criteria, and the resulting number of patient scan sets utilized in this study.

### 2.2.2 *Scanning Protocol*

All patients were scanned with a Philips scanner, either with the Philips EPIQ or Philips iU22 (Philips Medical Systems, Bothell, WA) in a contrast specific mode (amplitude modulation). Both systems utilized a low-frequency abdominal C5-1 transducer (side-side/contrast-fundamental imaging, contrast frequency: 1.7 MHz, mechanical index: 0.06). During the entire continuous scan, the probe was held at specific plane of the lesion and/or liver. In most of the scans, an articulated arm (Fisso, Baitella AG, Switzerland) fitted with a modified biopsy guide to act as a probe holder was employed to minimize probe motion and ensure the same plane was scanned over the duration of the loop (**Fig. 2.2a**). An aliquot of 1.2 mL of Lumason (called SonoVue outside the US) contrast agent (Bracco Suisse SA, Geneva, Switzerland) were pre-loaded into a line with a 3-way stop-cock, and delivered as a bolus with a 5 mL saline flush (**Fig. 2.2b**). A continuous cine loop was collected for a minimum of 60 seconds (2). The transducer was repositioned to a similar plane (slightly translated and/or rotated to account for small differences in repeated scans in longitudinal studies), and the process was repeated for a total of at least 2 injections. Since the patient population was taken from more than one study, only patients that strictly adhered to the above-described scanning protocol were included.

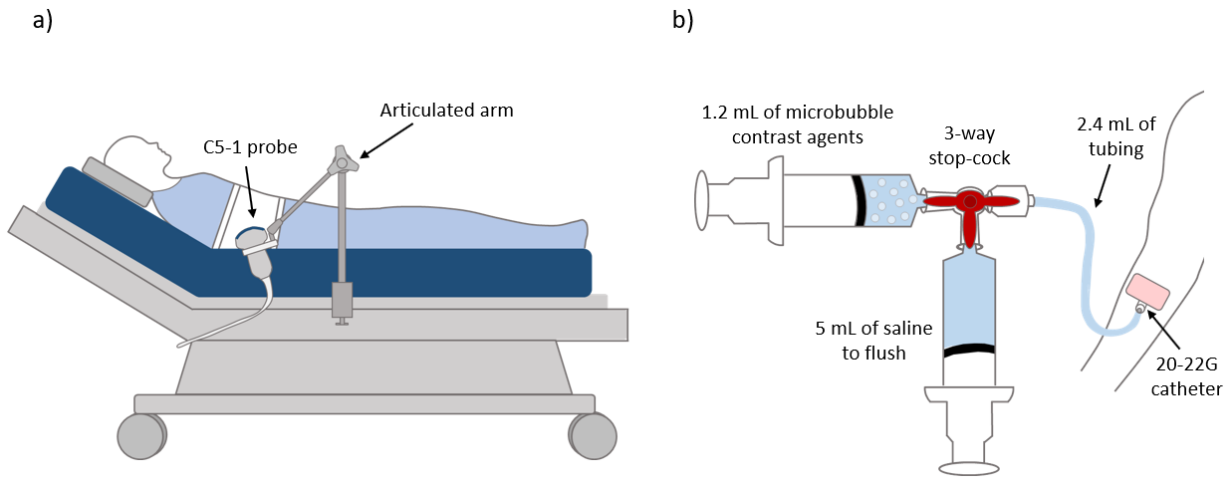


**Fig. 2.2**: (a) An example diagram of a patient being scanned, with the abdominal transducer (C5-1) attached to the articulated arm to maintain a single plane throughout the scan. (b) A schematic of the contrast agent injection setup with the 20-22G catheter, the 3-way stop-cock, the syringe with the microbubbles in line with the catheter tubing and the saline flush, at 90 degrees.

### 2.2.3 *Data Analysis*

CEUS image loops were extracted as native DICOM data and analyzed in a custom quantification tool developed by our group titled "qDicomUW" (16). Linearized data was accessed utilizing a proprietary data transformation script from Philips (Philips Healthcare, Bothell, WA). An automated respiratory gating (ARG) algorithm (23, 25) was utilized to eliminate out-of-plane motion. This algorithm requires a user-defined key frame at a specific point of the respiratory cycle (typically with an ideal view of the lesion). This algorithm forms a TIC from a region of interest (ROI) automatically selected around a continuous, bright, moving interface on the fundamental image of the key frame (**Fig 2.3**). The sinusoidal behavior of the TIC results from respiratory motion causing the interface captured by the ROI at the key frame to move in and out of the ROI, due to moving in and out of the scan plane. As determined from previous work (16, 25), all frames with greater than 15% intensity fluctuation from their local peaks of the TIC were eliminated to remove out-of-plane motion. A motion compensation algorithm utilizing two-dimensional normalized cross-correlation on the fundamental image of the respiratory gated frames was implemented and used to account for any residual translational motion (in-plane).

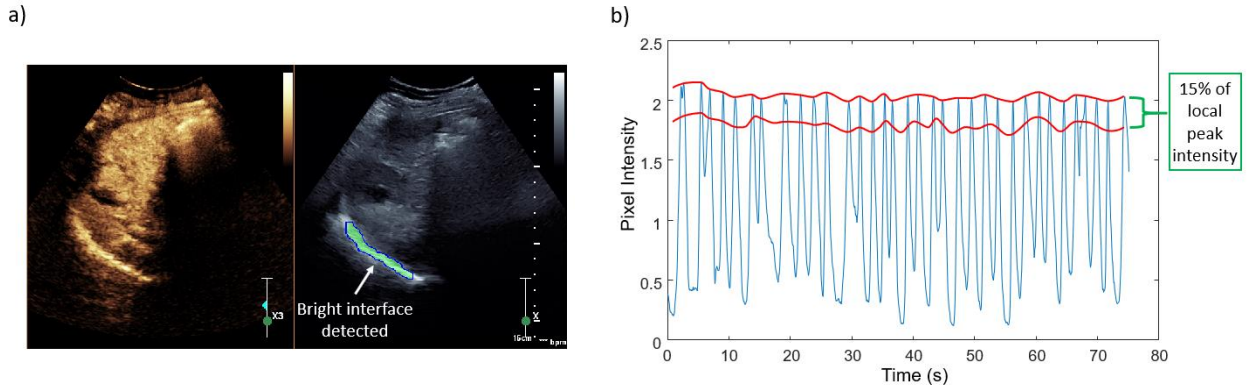


**Fig. 2.3**: a) A representative side-side ultrasound image, highlighting a bright interface in the fundamental image automatically identified by the automatic respiratory gating algorithm. (b) An example curve of the intensity tracked by the region of interest from (a) over time. Red lines encompass points within 15% of the intensity of the local peaks, or corresponding frames, that are preserved by ARG on the blue time-intensity curve.

### 2.2.4 *Patient Data Quantification*

After respiratory gating and motion compensation, a ROI was drawn around the feature to be analyzed (lesion or parenchyma) and the corresponding TIC was extracted (**Fig 2.4**). From the TIC the important perfusion-related parameters suggested by the Radiological Society of North America (RSNA) Quantitative Imaging Biomarkers Alliance (QIBA) CEUS committee (rise time—*RT*, mean transit time— *MTT*, peak intensity— *PI*, and area under the curve— *AUC*) were calculated. Points within the same respiration on the TIC were averaged to reduce the impact of noise on extracted bolus transit parameters. These two calculations schemes were performed on TICs extracted from both the lesion and the parenchyma ROI, and for each injection (**Fig. 2.5**). Images with ROIs are shown in **Fig. 2.5 (a, b, g, h)**, and extracted TICs with fitted curves up to the 50% intensity point noted with a magenta asterisk and the calculation of the bolus transit parameters from the fitted curve in **Fig. 2.5 (c, e, I, k)**. Raw TICs with the direct calculation of the bolus transit parameters are shown in **Fig. 2.5 (d, f, j, l)**. ROIs were drawn with synchronized ROIs on the fundamental side of the image for localization.

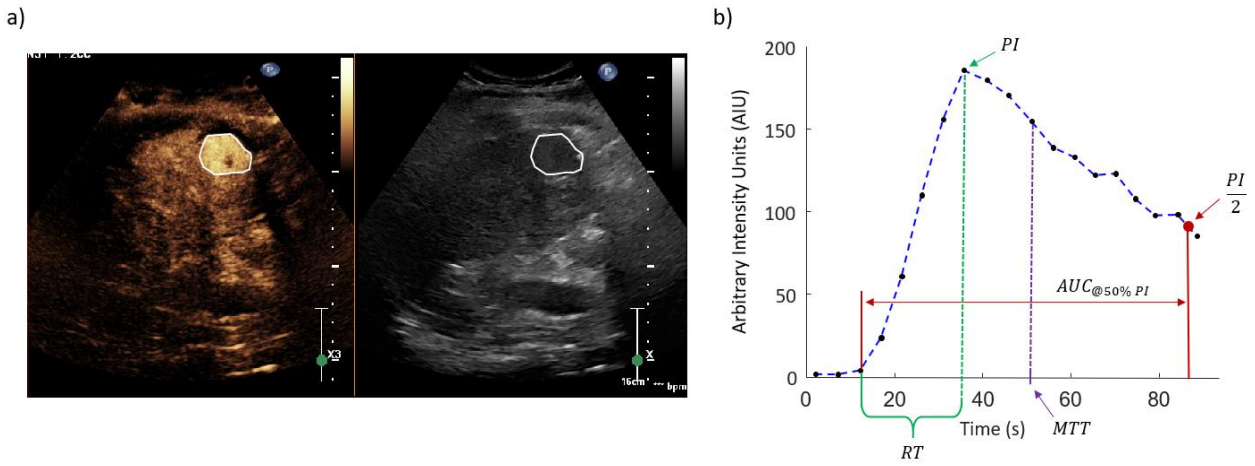


**Fig. 2.4**: (a) An example side-side ultrasound image with a region of interest drawn around the lesion in both the contrast and fundamental image. The extracted time-intensity curve is displayed in (b) after automated respiratory gating and motion compensation. Representative illustrations of where the four extracted bolus transit parameters (rise time – RT, mean transit time – MTT, peak intensity – PI, area under the curve – AUC) are calculated from the TIC are overlaid on the curve.

### 2.2.5 *Parameter extraction from a fitted lognormal distribution curve*

It has been common practice that a lognormal distribution curve is fitted on the TIC data to remove noise and enable the estimation of the CEUS perfusion-related parameters (3, 5) as recommended by RSNA/QIBA-CEUS. In previous studies, investigators have used different mathematical models for the fitted curve. However, following the recommendation of QIBA/CEUS, we use the lognormal distribution function whose mathematical form is shown below,

$$I(t) = \frac{AUC}{\sqrt{2\pi}\sigma(t-t_0)} e^{-([\ln(t-t_0)-\mu]^2)/(2\sigma^2)} + I_0, \quad t > t_0, \tag{1}$$

where $I(t)$ is the backscattered signal intensity, $I_0$ is the intensity offset (the intensity value before contrast arrival which may not be exactly zero), $t_0$ is the time delay, and μ and σ are the mean and standard deviation of the normal distribution of the logarithm of the independent variable t (time), respectively. Since we are only interested in the first pass of the bolus, we are not considering the influence of recirculation, and therefore the lognormal curve was fitted from the beginning of the scan to the first data point after the peak that is 50% of the peak intensity ($t_{PI/2}$). The 50% point is necessary to ensure a good quality of fit with the lognormal distribution function. This is an

important new element provided with our analysis that ensures recirculation does not influence the parameters and greatly contributes towards repeatability. *RT* was calculated analytically from the fitted curve as

$$RT = t_{max} - t_{start} = e^{\mu - \sigma^2}, \quad (2)$$

where $t_{max}$ is the time at the maximum value of the fitted curve, $t_{start}$ is the time of the first arrival of contrast. $t_{start}$ was calculated for each TIC by performing a backwards iterating slope calculation between values starting at the maximum value until the slope was an extremely small value (< 0.01). The scan time of the first value with a slope smaller than this condition was defined $t_{start}$. $t_{start}$ is equivalent to $t_0$ in eqn. (1). This right side of this equation is derived from the lognormal distribution where $\mu$ and $\sigma$ are the mean and standard deviation respectively (5). *PI* is simply the maximum value of the fitted curve. *MTT* and *AUC* are defined as:

$$AUC = \int_{t_{start}}^{t_{end}} I(t)\, dt \quad (3)$$

$$MTT = \frac{\int_{t_{start}}^{t_{end}} I(t) * t\, dt}{\int_{t_{start}}^{t_{end}} I(t)\, dt} \quad (4)$$

where $t_{end}$ is the last point to be included in the calculation. For $t_{end} \rightarrow \infty$, MTT is calculated explicitly as

$$MTT = e^{\mu + \sigma^2/2} \quad (5)$$

Since we are only considering the first pass (excluding recirculation), $t_{end}$ is the time when the intensity is 50% of *PI* and $t_{end} = t_{PI/2}$. The integral of $I(t)$ in eqns. (2)-(3) was computed utilizing the trapezoid rule. A coefficient of determination ($R^2$) was also calculated to evaluate quality of the fit. The current calculation of *MTT* also presents an important step towards standardization and contributes towards greater repeatability as there was confusion about the limits of integration in the past.

### 2.2.6 *Direct parameter extraction without curve fitting*

The 4 CEUS bolus transit parameters were also computed directly from the numerical image data (not the fitted curve as was described in the section above). Each of these metrics on an example TIC can be visualized in **Fig. 2.4b**. **Fig. 2.5** displays the TICs computed directly from image data from 2 subsequent injections on a patient for a lesion (**Fig. 2.5d,j**) and liver parenchyma (**Fig. 2.5f,l**), and the 4 CEUS perfusion-related parameters extracted directly from it. These metrics were very similar when extracted from the fitted lognormal distribution curve, as displayed for the lesion in **Fig. 2.5c,i** and parenchyma **Fig. 2.5e,k** and this provides a proof that the actual TIC data were of high quality and without excess noise.

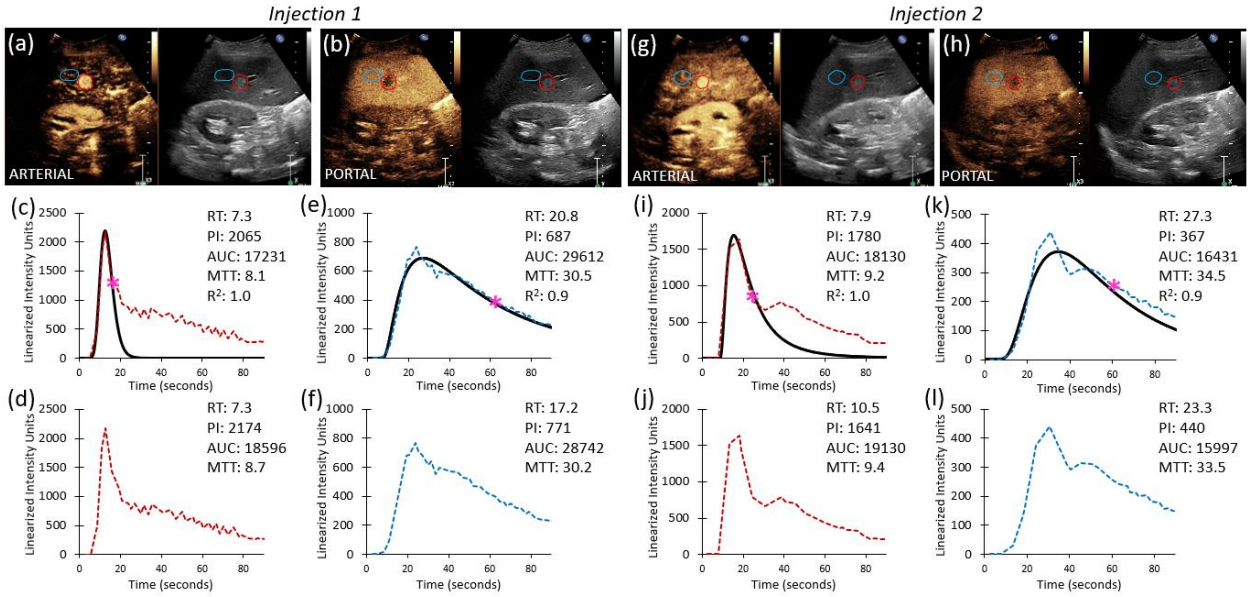


**Fig. 2.5**: Example side-side ultrasound images at the peak arterial (a,g) and portal (b,h) timepoints for two sequential injections on the same patient. Red regions of interest (ROI) are drawn around the lesion, while blue ROIs surround a uniform area of the liver parenchyma. Extracted time-intensity curves (TIC) for the lesion and liver parenchyma are red and blue respectively to match the corresponding ROIs (c-f and i-l). A black fitted lognormal curve is overlaid, and the four extracted bolus transit parameters (rise time – RT, mean transit time – MTT, peak intensity – PI, area under the curve – AUC) and $R^2$ values from the fitted curve are displayed in panels c,e,i, and k. A small magenta asterisk was overlaid to highlight the latest point of the TIC the lognormal distribution curve was fit to. The same extracted TICs without the fitted lognormal curve and with the four extracted bolus transit parameters calculated directly from the TIC are displayed below the lognormal evaluation in panels d,f,j, and l.

### 2.2.7 *In vitro evaluation*

To confirm and further validate trends observed in the extracted patient metrics from this analysis method, a controlled in vitro experiment was performed. A 1-way flow system with a tissue mimicking phantom established in previous work was utilized to evaluate the bolus dynamics of microbubble contrast agents, and data was collected as defined in this previous study (3). CEUS image loops were collected and analyzed with the same tools as the clinical study here, with linearized TICs extracted from a ROI centered in the tube (**Fig. 2.6a, b**). No ARG or motion compensation was necessary as there was no respiratory motion. The four CEUS perfusion-related parameters (*RT*, *MTT*, *PI*, and *AUC*) were extracted from both the fitted lognormal curve and directly from the TIC as done in the clinical work.

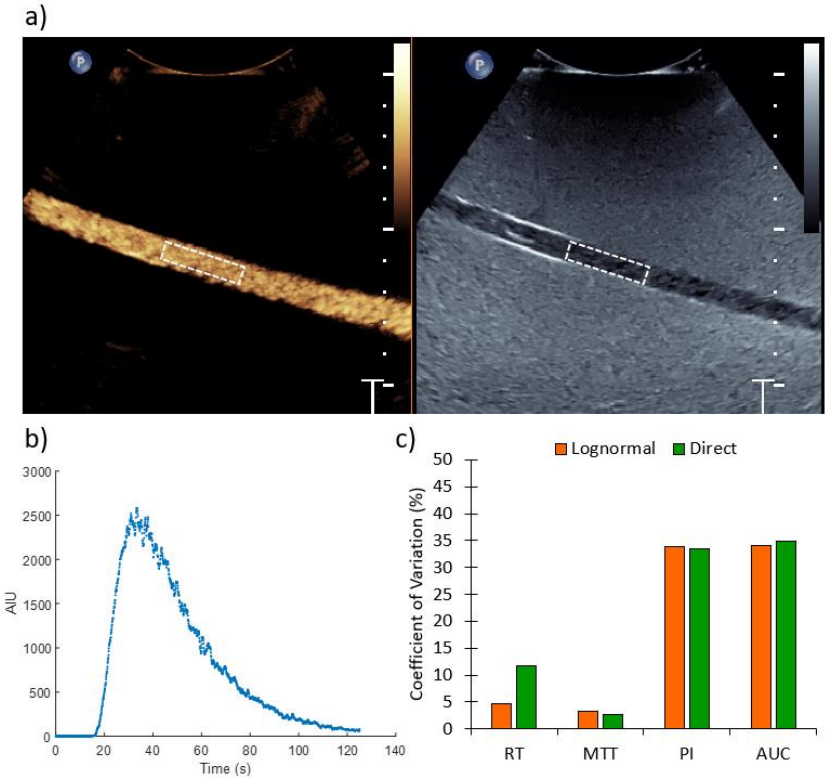


**Fig. 2.6**: (a) A representative side-side ultrasound image of the in-vitro phantom setup, with a white dashed region of interest (ROI) drawn in the center of the tube. (b) The example linearized time-intensity curve extracted from this ROI. (c) A bar plot of the average inter-injection coefficient of variation (COV) for the four extracted bolus transit parameters (rise time – *RT*, mean transit time – *MTT*, peak intensity – *PI*, area under the curve – *AUC*), from the fitted lognormal curve and directly from extracted time-intensity curves.

### 2.2.8 *Statistical Analysis*

To evaluate the repeatability of extracted perfusion metrics in clinical data, the coefficient of variation (COV) between injections on the same patient were calculated for all parameters. The COV was calculated separately when using the fitted curve and when using the TIC data directly without a fitted curve. To establish the range for the quality of the fitted lognormal curve, a 95% confidence interval was performed across all lesion and all parenchyma $R^2$ values respectively. To demonstrate independence of the bolus injections, the difference between each bolus transit parameter from injections on the same patient calculated via the fitted lognormal curve was evaluated, and a one sample t-test was performed for these differences across all patients. To establish differences between the calculation schemes, the difference between each perfusion-related parameter from injections on the same patient calculated via the fitted lognormal curve and direct calculation (i.e., $RT_{lognormal} - RT_{direct}$) was performed, and a one sample t-test was conducted for these differences across all patients as well.

## 2.3 RESULTS

TICs with linearized data were analyzed and the four bolus transit parameters were calculated with both lognormal and direct calculation schemes, as demonstrated in **Fig. 2.5**. The extracted TICs and perfusion-related metrics were similar between injections and between calculation methods (with or without a fitted curve) for both the lesion and parenchyma ROIs. Two patient examples are highlighted in **Fig. 2.7**. As a reminder, the fitted curve is only up to the 50% intensity level and the 4 bolus transit metrics are calculated up to that time. The 2 curves (fitted model and actual data) are very similar up to the 50% time point and produce similar perfusion-related metrics. Despite minor differences, general agreement between the TICs and fitted lognormal curves are demonstrated here as well for both injections on each patient. High similarity in temporal dynamics of the TICs (influencing *RT* and *MTT*) is displayed between injections, while overall intensity of the TICs (influencing *PI* and *AUC*) exhibits more variability. Patient 2 injection 2 provides a representative example where selection of the peak differs slightly between the fitted lognormal curve and the TIC, the main source of variation between the two calculation methods.

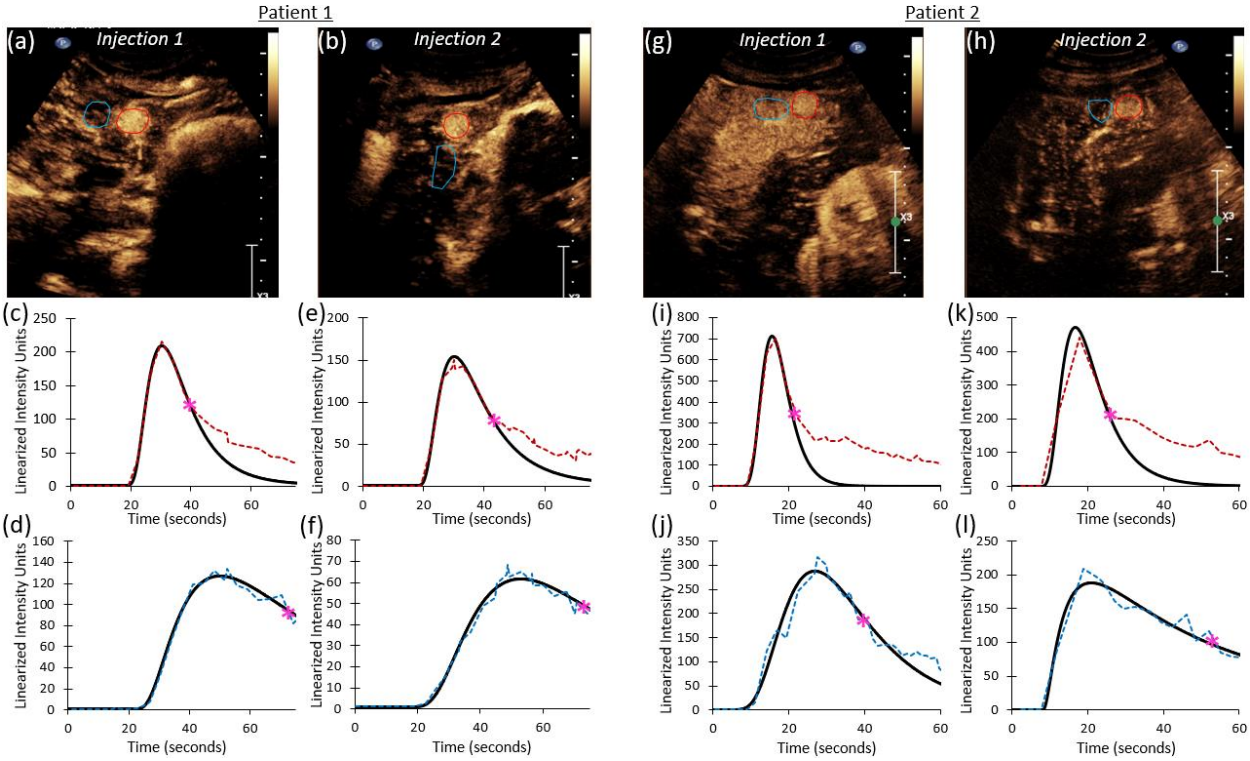


**Fig. 2.7**: Pairs of injections from two example patients utilized in this study. Contrast ultrasound images with red regions of interest (ROI) drawn around the lesion, and blue ROIs around a uniform area of liver parenchyma are display in panels a, b, g, and h. Extracted time-intensity curves (TIC) for the lesion and parenchyma which are red and blue respectively to match the corresponding ROIs overlaid with a black fitted lognormal curve are displayed for the tumor ROI in panels c, e, i and k and liver parenchyma ROI in panels d, f, j, and l. A small magenta asterisk was overlaid to highlight the latest point of the TIC the lognormal distribution curve was fit to.

Breakdown of average scan duration, liver lesion types, and lognormal $R^2$ are shown in **Table 2.1**. The 95% confidence interval for all fitted lognormal curves was [0.95, 0.96], with the lowest $R^2$ value for a TIC in this study being 0.85. As a measure of the repeatability of this standardized quantitative method, we present the average inter-injection COV for *RT*, *MTT*, *PI*, and *AUC* for lesions and parenchyma in **Fig. 2.8**. Standard error was displayed to capture the variability of these COV calculations. The one sample t-test performed on the inter-injection difference between extracted perfusion-related parameters for each patient showed no significant differences (**Table 2.2**). However, the one sample t-test between parameters generated from the fitted lognormal curve and the direct calculation demonstrated significant differences ($\alpha = 0.05$) for lesion *MTT* and *PI*, and for parenchyma *PI* (**Table 2.3**).

| Parameter | Details |
|---|---|
| Scan length | 84 ± 26.3 s |
| Lognormal $R^2$ | 0.956 [0.950, 0.960] |
| Lesion type | |
| Hepatocellular carcinoma | 28 |
| Metastasis | 10 |
| Focal nodular hyperplasia | 2 |

**Table 2.1**: A summary of characteristics of the patient dataset.

An example TIC extracted from CEUS data in the phantom is shown in **Fig. 2.6b**. We note that in such a phantom we get TICs which are very smooth and closely resemble theoretical bolus models previously suggested (5). Average inter-injection COVs for *RT*, *MTT*, *PI*, and *AUC* from the in vitro work are presented in **Fig. 2.6c**. We note that these values are very similar to those derived from the patient study in **Fig. 2.8**.

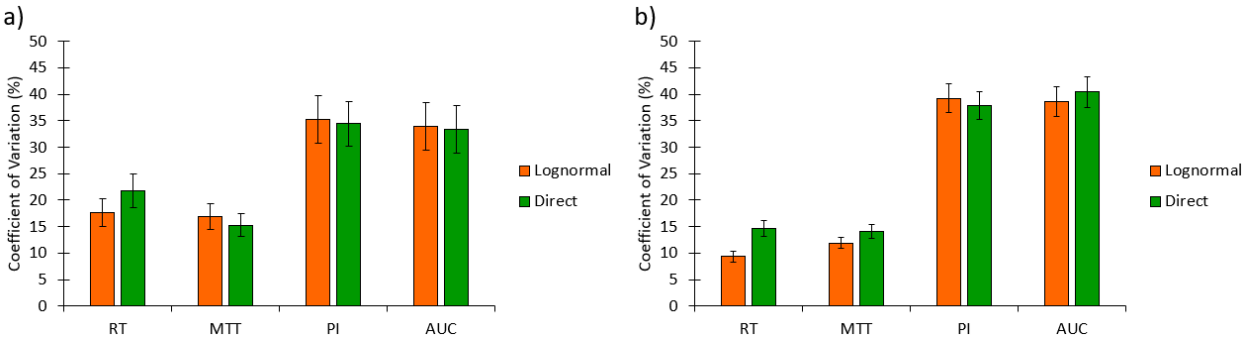


**Fig. 2.8**: Bars plot of the average inter-injection coefficient of variation (COV) for the four extracted bolus transit parameters (rise time – RT, mean transit time – MTT, peak intensity – PI, area under the curve – AUC), from the fitted lognormal curve and directly from extracted time-intensity curves and for evaluated lesions (a) and liver parenchyma (b). Standard error calculations are overlaid in error bars.

| | Bolus Transit Parameter | Mean Interinjection Difference | Standard Error of Interinjection Difference | *P* ($\alpha = 0.05$) |
|---|---|---|---|---|
| Lesion | *RT* | 0.7 | 0.9 | 0.40 |
| | *MTT* | 1.2 | 1.2 | 0.32 |
| | *PI* | −12.9 | 32.0 | 0.69 |
| | *AUC* | 1992.8 | 2409.4 | 0.41 |
| Parenchyma | *RT* | −0.4 | 0.6 | 0.48 |
| | *MTT* | −0.4 | 1.0 | 0.72 |
| | *PI* | 18.2 | 14.7 | 0.22 |
| | *AUC* | 530.9 | 593.0 | 0.37 |

**Table 2.2**: Results from one-sample t-tests performed on the inter-injection difference between the four extracted bolus transit parameters (rise time – RT, mean transit time – MTT, peak intensity – PI, area under the curve – AUC) for the lesion and liver parenchyma. No statistically significant difference ($\alpha = 0.05$) was found for any parameter.

| | Bolus Transit Parameter | Mean Intermethod Difference | Standard Error of Intermethod Difference | *P* ($\alpha = 0.05$) |
|---|---|---|---|---|
| Lesion | *RT* | 0.1 | 0.3 | 0.74 |
| | *MTT* | −0.5 | 0.2 | 0.01 |
| | *PI* | −10.6 | 4.5 | 0.02 |
| | *AUC* | −209.8 | 114.6 | 0.41 |
| Parenchyma | *RT* | 0.6 | 0.4 | 0.09 |
| | *MTT* | −0.4 | 1.0 | 0.72 |
| | *PI* | −18.6 | 2.5 | 1E-11 |
| | *AUC* | 233.8 | 228.4 | 0.31 |

**Table 2.3**: Results from one-sample t-tests performed on the difference between the four extracted bolus transit parameters (rise time – RT, mean transit time – MTT, peak intensity – PI, area under the curve – AUC) for the lesion and liver parenchyma from the fitted lognormal curve and value calculated directly from the time-intensity curve (i.e., $RT_{lognormal} - RT_{direct}$). Statistically significant differences ($\alpha = 0.05$) were only found for lesion MTT, and lesion and parenchyma PI.

## 2.4 DISCUSSION

To ensure accurate and repeatable quantification of lesion or parenchymal perfusion with CEUS, standardized and controlled imaging protocol is critical. Generation of a meaningful TIC for a region of interest requires that it continuously images the same plane, and current freehand approaches introduce high risk for probe motion that cannot be recapitulated. Maintaining a

stationary image plane is also necessary to ensure that complex respiratory gating and motion compensation algorithms function properly as they assume that the probe has not shifted. Handheld scans with minimal probe motion can be achieved for short, continuous loops by experienced sonographers however longer loops lead to fatigue and scanning at the same plane may not be assured even with experienced sonographers. The use of an articulated arm to hold the imaging probe circumvents this barrier entirely and allows for systematic quantification of 2D CEUS data. With multiple degrees of freedom, the articulated arm does not limit CEUS data collection based on position or depth beyond the existing limitations of 2D CEUS probe positioning. Use of an articulated arm is especially beneficial when evaluating suspected HCCs with the Liver Imaging Reporting and Data System (LI-RADS) protocol that requires imaging the lesion to evaluate washout up to 5 minutes. Despite the benefits, there is a small added complexity introduced by the articulated arm which can be overcome with minimal training and further development of such devices for ease of use.

In clinical studies to evaluate abdominal lesions with CEUS, the microbubble contrast agent is primarily delivered with a bolus injection. However, many published clinical research studies especially in cardiology have also used a continuous infusion for the implementation of the destruction/replenishment protocol (not used in the present study). Many excellent studies have taken advantage of the removal of the cardio-pulmonary effect on microbubble transit to organs such as the liver achieved by destruction/replenishment protocols for evaluations of blood flow in clinical studies (9, 14, 27). This protocol allows repeated evaluations by simply destroying the agent and allowing it to re-perfuse multiple times. However, this technique requires use of a specialized infusion pump to continuously mix the agent and careful tuning of infusion speed to avoid needing a long time to reach steady state or a very high concentration of microbubbles delivered and leading to acoustic shadowing that can adversely impact accurate measures of blood volume (28). The simple bolus injection protocol can also be accurately repeated as long as certain standardization steps are taken. Those include (a) using a large intravascular catheter (20-22G) that is placed in the antecubital vein to avoid high injection pressure which can lead to bubble destruction in the catheter; (b) using a new vial of Lumason for each patient and with manual agitation between each injection; and (c) using a 3-way stop-cock system and saline flush. The repeatability of the bolus method after these simple standardization steps is demonstrated by the

lack of significant differences when comparing extracted perfusion-related metrics between injections on the same patient (**Table 2.2**).

Accurate quantification of 2D CEUS data requires minimizing the effects of respiratory motion which was achieved with our ARG and motion compensation algorithm. ARG was first used to remove images after out-of-plane motion, then motion compensation was performed to eliminate any remaining translational motion and improve TIC accuracy. The use of the articulated arm and these algorithms contributed to the high average $R^2$ value (0.96) found amongst all TICs fitted with a lognormal distribution curve (**Table 2.1**). Other groups have implemented advanced motion compensation algorithms with freehand scanning (17, 29), but their results have been impacted by occasional unwanted probe motion (e.g., sliding) that introduces changes of the scan plane during data collection and possibly due to using a less robust analysis.

The 4 specific bolus perfusion metrics we selected and their exact calculation approach were very important elements that led to excellent repeatability for the objective quantification of perfusion from CEUS data. The tumor and parenchyma ROIs were selected at comparable image depths, were similarly sized, and avoided major vessels. The resulting linearized TICs were then used to extract the bolus transit metrics either directly from the actual data or a fitted lognormal distribution curve. For the lognormal fitted curve, the point $t_{end}$ was automatically calculated as the first point after the maximum of the TIC at 50% of its magnitude. By fitting only up to this point, as the equation ideally models only the transit of a single bolus, we are able to omit the effects of recirculation in a systematic way. Similarly, bolus transit parameters such as *MTT* and *AUC* were calculated using eqns. 3-4 on both the raw TIC data and the fitted curve. This study is one of the first times that bolus metrics were evaluated directly from the data, as the data collection and processing components used in this study generated TICs without a significant amount of noise.

A significant point investigated in this study was the comparison of perfusion metrics extracted directly from the TIC data and from a curve fitted on the TIC data. The specific mathematical function of the fitted curve to be used for quantification has been a standardization barrier over the years and one main source of differences between groups. Despite attempts to connect blood flow with indicator dilution models, the most important reason for using such models is the elimination

of data noise. Fitted curves based on indicator dilution like the lognormal distribution, the Gamma variate, lagnormal distribution and even empirical models have been previously suggested to remove excessive noise due to motion and other influences to the TIC (5). However, variation in curve fit models have also produced differences in results obtained by studies from different centers (2). RSNA/QIBA-CEUS suggests the use of the lognormal distribution model, but here we demonstrate that the lognormal distribution model and direct calculation of four bolus metrics produce similar results. With use of an articulated arm and the respiratory motion algorithms used in our analysis, resulting TICs have considerably less noise as indicated by the high average $R^2$ value of 0.96, allowing for bolus metrics to be extracted directly from the data. Differences in calculations of *RT*, *MTT*, *PI*, and *AUC* from the fitted lognormal curve and with direct calculation for the same lesions and regions of parenchyma were evaluated with a t-test (**Table 2.3**). There were no significant differences found except for lesion *MTT* and lesion and parenchyma *PI*. Lesion *MTT* was typically slightly smaller in the fitted curve calculation than the calculation directly from the TIC, attributed to the fitted lognormal curve being more heavily weighted to capture the rapid enhancement exhibited by the lesion. The lesion and parenchyma *PI* were slightly smaller with the fitted lognormal evaluation as the peak of the fitted curve is typically less than the absolute max data point extracted for *PI* in the direct method. This simple calculation of the peak intensity in the direct method is more susceptible to noise and could easily be improved in future work. Despite finding statistically significant differences between calculation schemes for these three metrics, the mean inter-method differences found for these variables are not scientifically relevant as their magnitude is very small compared to the ranges of these parameters. As demonstrated by the extremely similar inter-injection average COVs, the repeatability of the two calculation methods is approximately the same. However, one important use of a fitted curve is a means to evaluate quality of the data. Currently, $R^2$ assesses data quality using a fitted curve, despite there not being a universally accepted value to determine whether data should or should not be quantified. As automation continues to improve, metrics determining calculation quality will become increasingly important. Therefore, future studies could investigate the generation of a new metric that does not rely on curve fitting to determine data quality, such as a measure of existing motion within the video loop similar to that typically used in motion compensation algorithms. Despite the minor benefits of the fitted curve calculation in accounting for noise in the TIC, lack of standardization in curve fitting in the field and a lack of a universal bar to determine if data is

adequate for quantification (which could be more easily overlooked in a fitted curve than raw TIC data), use of a fitted curve could introduce greater variability in CEUS evaluations amongst research groups. Reflected by the very high degree of similarity in extracted parameters between the calculation schemes, use of the collection and analysis techniques defined here with the direct calculation method provide the desired perfusion metrics while avoiding these possible sources of variability.

This study focused on evaluating the repeatability of quantitative perfusion-related parameters from CEUS data with a standardized imaging protocol and analysis method. Average inter-injection COV for *RT* and *MTT* were found to be 15-21% and 9-15% for evaluated lesion and parenchyma respectively. Meanwhile, average inter-injection COV for *PI* and *AUC* were at 33-35% and 38-40% for the lesion and parenchyma respectively. The considerably smaller magnitude COV of temporal metrics (*RT* and *MTT*) than the amplitude metrics (*PI* and *AUC*) is likely a result of inherent variability in intensity measurements collected with CEUS, even in carefully controlled in-vitro studies (3, 7, 30). The COVs for each metric was very similar (~1-3%) when computed with the fitted lognormal curve and direct calculations on the TIC. Inter-injection COV of parenchyma *RT* had the largest difference between the two calculation schemes at 6%, which is likely due to the crude evaluation of the peak in the direct method (see Fig. 7, patient 2, injection 2 – tumor). The repeatability of these metrics is critical for designating what constitutes a true change in longitudinal evaluations of tumor blood flow in possible future studies utilizing this tool, as only changes to parameters greater than the COVs evaluated here would be considered true therapy-induced changes. The high repeatability of these four parameters could achieve the necessary sensitivity and accuracy for treatment monitoring with CEUS, but would require evaluation in treatment monitoring studies.

Inter-injection COVs in vitro between direct and lognormal evaluation were extremely similar or identical for all but *RT* where the direct calculation average COV was a little higher, likely a result of the residual oscillatory noise impacting the accuracy of the identification of the peak of the curve in the direct calculation on the TIC. Additionally, these COVs of the 4 CUES perfusion parameters (*RT*, *MTT*, *PI*, and *AUC*) were quite similar between the in vitro and in vivo studies (Fig. 6c and Fig. 8). Specifically, the temporally-based metrics (*RT* and *MTT*) were less than 20%

and the amplitude-based ones (*PI* and *AUC*) were less than 40%. Considering the simple nature of a single tube in a controlled in vitro environment, we assume that the COVs calculated present the best-care scenario. The fact that the in vivo COV values are only slightly higher is a confirmation that our protocol and analysis has eliminated most of the confounding variability.

While other groups have evaluated variability in clinical studies, they have found differing degrees of repeatability and reproducibility from our study and each other. Lassau et al. (10) evaluated reproducibility and intra-patient variability of CEUS bolus transit parameters in 60 patients with a variety of lesions and treatments, with pairs of CEUS scans taken at baseline, 15 days, and 1 month after initiation of treatment. Variability between CEUS pairs was measured with COV and found to be 54%, 53%, 87%, and 61% for *RT*, *MTT*, *PI*, and *AUC*, respectively. Similar to our study, the time-based metrics (*RT* and *MTT*) were found to be more reproducible than intensity-based ones (*PI* and *AUC*), but at a higher magnitude. Possible sources of the increased variability are motion during scanning, the linearization scheme, the fitted curve used, or possible influence of recirculation.

Williams et al. (14) studied repeatability of CEUS perfusion in 17 renal cell carcinoma patients with both destruction-replenishment and bolus methods, each with 2 bolus injections followed by 7 evaluations made during a 12-minute infusion. Destruction-replenishment was highly reproducible with a COV of 15%, which the authors attributed to all measurements occurring in a single infusion and scan plane. Bolus reproducibility evaluated with median inter-injection percent difference was found to be 36%, 56%, 49%, and 70% for *RT*, *MTT*, *PI*, and *AUC*, respectively. The trend in variability of these parameters (temporally-based metrics exhibiting greater repeatability than intensity-based ones) is similar to our findings and those of Lassau et al. (10), but higher than their destruction-replenishment results which the authors accredit to inhomogeneity in evaluated scan planes.

El-Kaffas et al. (9) explored repeatability of 3D CEUS in 11 patients with liver metastases with destruction-replenishment and bolus methods, each with a 3-minute infusion followed by two bolus injections. Destruction-replenishment was found to be highly repeatable with concordance correlation coefficients (CCCs) of 0.97 and 0.95 for relative blood velocity and flow, respectively.

For bolus injections, CCCs were found to be 0.74, 0.30, 0.84, and 0.84 for *RT*, *MTT*, *PI*, and *AUC*, respectively. The findings of destruction-replenishment compared to bolus are similar to those found by Williams et al. (5) and observed in our study, but the inverse trend was found for bolus parameters (intensity-based parameters were more repeatable). This could possibly be attributed to variation in a patient's ability to hold their breath as instructed or low volume rate (~1 Hz) which could have greater influence on the time-based dynamics.

Our standardized imaging method and analysis has potential for augmenting and possibly improving the clinical evaluation of longitudinal perfusion changes through quantification of CEUS data, but there are some limitations. The potential for any variability arising from different imaging sessions on different days and/or performing the exam at different centers was not evaluated in the present study. Despite utilizing a large number of patients, the evaluated lesions were primarily HCCs. Future studies using this technique in other lesions or organs could experience unique challenges which could influence the results, and would need to be investigated. Another limitation of this approach is the use of 2D CEUS, which restricts evaluation of lesions to a single plane per injection. Solid tumors are heterogenous and their vascular patterns could vary between planes. The use of 3D CEUS, which is beginning to become clinically available, could resolve this issue by capturing the entirety of the tumor. However, a major limitation at the current time for 3D CEUS is the ability to collect and save data at an ample volume rate (10 Hz).

A primary motivation for developing standardized and repeatable perfusion quantification methods is to be able to use them in longitudinal studies to evaluate tumor perfusion changes resulting from treatment and predict response at an earlier timepoint. Aspects of this method could be applied to other tumors such as kidney, prostate, and breast which have been explored with CEUS as well (10, 31-35), with careful consideration of the challenges unique to each of these tumors. Application of this work is also not limited solely to cancer. Investigators utilizing CEUS have made excellent advances in areas such as organ transplant perfusion (36), diabetes (37), inflammatory bowel disease (38, 39), peripheral artery disease (40, 41), and atherosclerotic plaque damage (42, 43) which could potentially utilize aspects of the method described here (use of articulated arm, injection technique, ARG, perfusion metric calculations) when applicable to the

obstacles exclusive to these environments to augment current approaches with a systematic quantification scheme.

In conclusion, we have presented a comprehensive imaging protocol and analysis method for the evaluation of tumor and organ perfusion with CEUS. Key elements of our methodology are the fixation of the probe, treatment of out-of-plane motion with respiratory gating, treatment of in-plane motion with motion compensation, standardized delivery of a bolus injection, selection of a standard model for curve fitting of the TICs, and identification of the perfusion-related important bolus metrics. With a patient study (N=80), we evaluated repeatability via inter-injection variability, where average COV of *RT* and *MTT* were less than 21% while *PI* and *AUC* were less than 40%. Interestingly, the COV of the bolus metrics from the patient study was very similar even when evaluating a simple flow phantom, and thus demonstrating that most sources of variability have been eliminated and the robustness of our method. Our imaging protocol and analysis method generated good quality TIC data evidenced by a high quality of fit ($R^2$=0.96) when the produced TICs were fitted to a lognormal distribution model. Furthermore, we demonstrated that curve fitting may be eliminated and the perfusion metrics may be extracted directly from the TIC data. There was no significant difference of the perfusion metrics when extracted with or without curve fitting. The comprehensive CEUS perfusion quantification methodology presented here provides highly repeatable perfusion metrics which could potentially be sensitive enough for evaluating therapy treatment outcomes in longitudinal studies.

## 2.5 REFERENCES


1. Josep ML, Riccardo L. mRECIST for HCC: Performance and novel refinements. Journal of Hepatology. 2020;72(2):288-306.
2. Averkiou MA, Bruce MF, Powers JE, et al. Imaging Methods for Ultrasound Contrast Agents. Ultrasound Med Biol. 2020;46(3):498-517.
3. Averkiou MA, Juang EK, Gallagher MK, et al. Evaluation of the Reproducibility of Bolus Transit Quantification With Contrast-Enhanced Ultrasound Across Multiple Scanners and Analysis Software Packages-A Quantitative Imaging Biomarker Alliance Study. Invest Radiol. 2020;55(10):643-56.
4. Wilson SR, Burns PN, Kono Y. Contrast-Enhanced Ultrasound of Focal Liver Masses: A Success Story. Ultrasound Med Biol. 2020;46(5):1059-70.
5. Strouthos C, Lampaskis M, Sboros V, et al. Indicator dilution models for the quantification of microvascular blood flow with bolus administration of ultrasound contrast agents. IEEE Trans Ultrason Ferroelectr Freq Control. 2010;57(6):1296-310.
6. Averkiou M, Lampaskis M, Kyriakopoulou K, et al. Quantification of tumor microvascularity with respiratory gated contrast enhanced ultrasound for monitoring therapy. Ultrasound Med Biol. 2010;36(1):68-77.
7. Dizeux A, Payen T, Barrois G, et al. Reproducibility of Contrast-Enhanced Ultrasound in Mice with Controlled Injection. Mol Imaging Biol. 2016;18(5):651-8.

8. El Kaffas A, Hoogi A, Zhou J, et al. Spatial Characterization of Tumor Perfusion Properties from 3D DCE-US Perfusion Maps are Early Predictors of Cancer Treatment Response. Sci Rep. 2020;10(1):6996.
9. El Kaffas A, Sigrist RMS, Fisher G, et al. Quantitative Three-Dimensional Dynamic Contrast-Enhanced Ultrasound Imaging: First-In-Human Pilot Study in Patients with Liver Metastases. Theranostics. 2017;7(15):3745-58.
10. Lassau N, Coiffier B, Faivre L, et al. Study of Intrapatient Variability and Reproducibility of Quantitative Tumor Perfusion Parameters Evaluated With Dynamic Contrast-Enhanced Ultrasonography. Invest Radiol. 2017;52(3):148-54.
11. Lin L, Wang Y, Yan L, et al. Interobserver reproducibility of contrast-enhanced ultrasound in diabetic nephropathy. Br J Radiol. 2022;95(1129):20210189.
12. Ryu H, Kim JH, Lee S, Han JK**.** Therapeutic response monitoring after targeted therapy in an orthotopic rat model of hepatocellular carcinoma using contrast-enhanced ultrasound: Focusing on inter-scanner, and inter-operator reproducibility. PLoS One. 2020;15(12):e0244304.
13. Wildner D, Pfeifer L, Goertz RS, et al. Dynamic contrast-enhanced ultrasound (DCE-US) for the characterization of hepatocellular carcinoma and cholangiocellular carcinoma. Ultraschall Med. 2014;35(6):522-7.
14. Williams R, Hudson JM, Lloyd BA, et al. Dynamic microbubble contrast-enhanced US to measure tumor response to targeted therapy: a proposed clinical protocol with results from renal cell carcinoma patients receiving antiangiogenic therapy. Radiology. 2011;260(2):581-90.
15. Li Y, Chahal N, Senior R, Tang MX**.** Reproducible Computer-Assisted Quantification of Myocardial Perfusion with Contrast-Enhanced Ultrasound. Ultrasound Med Biol. 2017;43(10):2235-46.
16. Krolak C, Dighe M, Clark A, et al. Quantification of Hepatocellular Carcinoma Vascular Dynamics With Contrast-Enhanced Ultrasound for LI-RADS Implementation. Invest Radiol. 2024;59(4):337-44.
17. Tiyarattanachai T, Turco S, Eisenbrey JR, et al. A Comprehensive Motion Compensation Method for In-Plane and Out-of-Plane Motion in Dynamic Contrast-Enhanced Ultrasound of Focal Liver Lesions. Ultrasound Med Biol. 2022;48(11):2217-28.
18. Lassau N, Bonastre J, Kind M, et al. Validation of dynamic contrast-enhanced ultrasound in predicting outcomes of antiangiogenic therapy for solid tumors: the French multicenter support for innovative and expensive techniques study. Invest Radiol. 2014;49(12):794-800.
19. Mischi M, Kuenen MP, Wijkstra H**.** Angiogenesis imaging by spatiotemporal analysis of ultrasound contrast agent dispersion kinetics. IEEE Trans Ultrason Ferroelectr Freq Control. 2012;59(4):621-9.
20. Hudson JM, Williams R, Lloyd B, et al. Improved flow measurement using microbubble contrast agents and disruption-replenishment: clinical application to tumour monitoring. Ultrasound Med Biol. 2011;37(8):1210-21.
21. Lassau N, Koscielny S, Albiges L, et al. Metastatic renal cell carcinoma treated with sunitinib: early evaluation of treatment response using dynamic contrast-enhanced ultrasonography. Clin Cancer Res. 2010;16(4):1216-25.
22. Hudson JM, Bailey C, Atri M, et al. The prognostic and predictive value of vascular response parameters measured by dynamic contrast-enhanced-CT, -MRI and -US in patients with metastatic renal cell carcinoma receiving sunitinib. European Radiology. 2018;28(6):2281-90.
23. Christofides D, Leen E, Averkiou M**.** Automatic respiratory gating for contrast ultrasound evaluation of liver lesions. IEEE Trans Ultrason Ferroelectr Freq Control. 2014;61(1):25-32.
24. Christofides D, Leen E, Averkiou MA**.** Evaluation of the Accuracy of Liver Lesion DCEUS Quantification With Respiratory Gating. IEEE Trans Med Imaging. 2016;35(2):622-9.
25. Christofides D, Leen EL, Averkiou MA**.** Improvement of the accuracy of liver lesion DCEUS quantification with the use of automatic respiratory gating. Eur Radiol. 2016;26(2):417-24.
26. Leen E, Kumar S, Khan SA, et al. Contrast-enhanced 3D ultrasound in the radiofrequency ablation of liver tumors. World J Gastroenterol. 2009;15(3):289-99.
27. Hudson JM, Karshafian R, Burns PN**.** Quantification of flow using ultrasound and microbubbles: a disruption replenishment model based on physical principles. Ultrasound Med Biol. 2009;35(12):2007-20.
28. Dietrich CF, Averkiou M, Nielsen MB, et al. How to perform Contrast-Enhanced Ultrasound (CEUS). Ultrasound Int Open. 2018;4(1):E2-e15.
29. Wan P, Chen F, Shao W, et al. Irregular Respiratory Motion Compensation for Liver Contrast-Enhanced Ultrasound via Transport-Based Motion Estimation. IEEE Trans Ultrason Ferroelectr Freq Control. 2021;68(4):1117-30.

30. Gauthier M, Leguerney I, Thalmensi J, et al. Estimation of intra-operator variability in perfusion parameter measurements using DCE-US. World J Radiol. 2011;3(3):70-81.
31. Huang H, Zhu Z-Q, Zhou Z-G, et al. Contrast-enhanced transrectal ultrasound for prediction of prostate cancer aggressiveness: The role of normal peripheral zone time-intensity curves. Scientific Reports. 2016;6(1):38643.
32. Huang X, Wang N, Liu L, et al. Pre-operative Prediction of Invasiveness in Renal Cell Carcinoma: The Role of Conventional Ultrasound and Contrast-Enhanced Ultrasound. Ultrasound Med Biol. 2023;49(9):2169-76.
33. Ioannidis GS, Goumenakis M, Stefanis I, et al. Quantification and Classification of Contrast Enhanced Ultrasound Breast Cancer Data: A Preliminary Study. Diagnostics (Basel). 2022;12(2).
34. Li J, Huang X, Wang L, et al. Role of Contrast-Enhanced Ultrasound With the Enhancement Pattern and Qualitative Analysis for Differentiating Hypovascular Solid Renal Lesions. Ultrasound Med Biol. 2024;50(2):295-303.
35. Sharma A, Grover SB, Mani C, Ahluwalia C**.** Contrast enhanced ultrasound quantitative parameters for assessing neoadjuvant chemotherapy response in patients with locally advanced breast cancer. Br J Radiol. 2021;94(1121):20201160.
36. Fischer K, Ohori S, Meral FC, et al. Testing the Efficacy of Contrast-Enhanced Ultrasound in Detecting Transplant Rejection Using a Murine Model of Heart Transplantation. Am J Transplant. 2017;17(7):1791-801.
37. Yang F, Jiang L, Ma Y, et al. Quantitative assessment of early kidney injury using high frame rate contrast-enhanced ultrasonography in a rabbit model of diabetic nephropathy. Med Ultrason. 2024;26(1):7-14.
38. Lu C, Gui X, Chen W, et al. Ultrasound Shear Wave Elastography and Contrast Enhancement: Effective Biomarkers in Crohn's Disease Strictures. Inflamm Bowel Dis. 2017;23(3):421-30.
39. Medellin A, Merrill C, Wilson SR**.** Role of contrast-enhanced ultrasound in evaluation of the bowel. Abdom Radiol (NY). 2018;43(4):918-33.
40. van Helvert M, Engelhard S, Voorneveld J, et al. High-frame-rate contrast-enhanced ultrasound particle image velocimetry in patients with a stented superficial femoral artery: a feasibility study. Eur Radiol Exp. 2022;6(1):32.
41. Wu Y, Tian S, Li C, et al. Predictive Value of Contrast-Enhanced Ultrasound in Chemical Lumbar Sympathectomy for End-Stage Arteriosclerosis Obliterans of the Lower Extremities. Pain Ther. 2022;11(1):209-23.
42. Belcik JT, Xie A, Muller M, Lindner JR**.** Influence of Atherosclerotic Risk Factors on the Effectiveness of Therapeutic Ultrasound Cavitation for Flow Augmentation. J Am Soc Echocardiogr. 2024;37(1):100-7.
43. Ran X, Niu GC, Shao YH, et al. Contrast-enhanced ultrasound evaluation of renal perfusion before angioplasty and its predictive value for hypertension. Technol Health Care. 2024;32(2):963-76.

# Chapter 3. QUANTIFICATION OF HEPATOCELLULAR CARCINOMA VASCULAR DYNAMICS WITH CONTRAST-ENHANCED ULTRASOUND FOR LI-RADS IMPLEMENTATION

Connor Krolak, Manjiri Dighe, Alicia Clark, Marissa Shumaker, Raymond Yeung, Richard G. Barr, Yuko Kono, Michalakis Averkiou

*Investigative Radiology. 2024 Apr 1;59(4):337-344.*

**Abstract**

*Objective:* The aim of this study is to describe a comprehensive contrast-enhanced ultrasound (CEUS) imaging protocol and analysis method to implement CEUS LI-RADS (Liver Imaging Reporting and Data System) in a quantifiable manner. The methods which are validated with a prospective single center study aim to simplify CEUS LI-RADS evaluation, remove observer bias and could potentially improve the sensitivity of CEUS LI-RADS.

*Materials and Methods:* This prospective single center study enrolled patients with hepatocellular carcinoma (HCC) (April 2021 – June 2022, N=31, mean age ± SD: 67 years ± 6, 24 men/7 women). For each patient, at least 2 CEUS loops spanning over 5 minutes were collected for different lesion scan planes utilizing an articulated arm to hold the transducer. Automatic respiratory gating and motion compensation algorithms removed errors due to breathing motion. The long axis of the lesion was measured in the contrast and fundamental images to capture nodule size. Parametric processing of time-intensity curve (TIC) analysis on linearized data provided quantifiable information of the wash-in and washout dynamics via rise time (RT) and degree of washout (DW) parameters extracted from the TIC, respectively. A Welch's t-test was performed between lesion and parenchyma RT for each lesion to confirm statistically significant differences. P-values for bootstrapped 95% confidence intervals of the relative degree of washout (rDW), ratio of DW between the lesion and surrounding parenchyma, were computed to quantify lesion washout. Coefficient of variation (COV) of RT, DW, and rDW was calculated for each patient between injections for both the lesion and surrounding parenchyma to gauge reproducibility of these

metrics. Spearman's rank correlation tests were performed between size, RT, DW, and rDW values to evaluate statistical dependence between the variables.

*Results:* Average lesion diameter was 23 mm (SD: ±8 mm). The RT for all lesions, capturing arterial phase hyperenhancement (APHE), was shorter than that of surrounding liver parenchyma ($p<0.05$). All lesions also demonstrated significant ($p<0.05$) but variable levels of washout at both 2-minute and 5-minute timepoints, quantified in rDW. The COV of RT for the lesion and surrounding parenchyma were both 11%, and the COV of DW and rDW at 2 and 5 minutes ranged from 22-31%. Statistically significant relationships between lesion and parenchyma RT and between lesion RT and lesion DW at the 2 and 5-minute timepoints were found ($p<0.05$).

*Conclusions:* The imaging protocol and analysis method presented provide robust, quantitative metrics that describe the dynamic vascular patterns of LI-RADS 5 lesions classified as HCCs. The RT of the bolus transit quantifies the APHE and the DW and rDW parameters quantify the washout from linearized CEUS intensity data. This unique methodology is able to implement the CEUS-LIRADS scheme in a quantifiable manner for the first time and remove its existing issues of currently being qualitative and suffering from subjective evaluations.

## 3.1 INTRODUCTION

Hepatocellular carcinoma (HCC) is the most common primary liver malignancy, and liver cancer is the second leading cause of cancer-related deaths globally (1). The disease has a high mortality rate that can be partly attributed to a delay in diagnosis and compromised hepatic function due to underlying liver diseases, limiting treatment options.

Currently, the state-of-the-art diagnostic metric for HCC in high-risk patients is LI-RADS (Liver Imaging Reporting and Data System), a qualitative image assessment used to evaluate tumor malignancy through analysis of lesion blood flow (2-4). HCC is diagnosed by the arterial phase hyperenhancement (APHE) and its relative washout compared to parenchyma in the late phase as seen on computed tomography (CT) or magnetic resonance imaging (MRI) in addition to other ancillary features (5). However, these blood flow characteristics can also be observed in real-time with contrast-enhanced ultrasound (CEUS), which utilizes a blood pool contrast agent consisting of 1-10 $\mu$m gas microbubbles that are detectable in the microcirculation. These blood flow patterns specific to HCC and unique to CEUS have been thoroughly described qualitatively in CEUS LI-RADS (6, 7). Despite the use of greyscale ultrasound for lesion detection and surveillance and the advantageous features of CEUS with the use of an intravascular agent and real-time imaging, the American Association for the Study of Liver Diseases (AASLD) recommends contrast CT or MRI as the first test of vascular characteristics (8, 9). Even though CEUS LI-RADS also defines unique vascular features to identify HCCs, wash-in and washout criteria are based on subjective assessment and hypothetical time-intensity curves (TICs) that are not generated in clinical practice. Although CEUS LI-RADS has high specificity, its moderate sensitivity and subjective evaluation could potentially be improved through the quantification of the vascular patterns defined in CEUS LI-RADS to promote its use as a first line vascular diagnostic option.

Prior studies quantifying CEUS data for HCC have utilized user-defined regions of interest (ROI) applied directly to CEUS loops to generate TICs, and subsequently performed curve-fit to extract perfusion-based parameters to attempt to differentiate HCCs (10-13). However, limitations of these prior studies include the inability to capture late washout due to bubble destruction from 5-minute continuous imaging or excessive respiratory motion. Motion compensation algorithms

have been developed to mitigate respiratory motion in and out-of-plane (14, 15), but these algorithms have only been utilized in continuous scans exclusively evaluating less than 2-minute TICs. Currently, no studies have attempted to implement the CEUS LI-RADS scheme through quantification. To address the current subjectivity in CEUS LI-RADS evaluations, a comprehensive standardized method to scan HCC patients to quantitatively capture APHE and also provide information relating to onset and degree of washout is needed.

The main objective of our study is to define an approach to quantify the parameters utilized in CEUS LI-RADS. The key elements of this approach are: (a) a scanning protocol for CEUS evaluation of HCCs that limits bubble destruction; (b) use of an articulated arm for holding the probe to register and compensate for transducer motion; and (c) a perfusion quantification algorithm utilizing parametric processing in order to measure the transit of a contrast bolus in the HCC vasculature. With a prospective single center study of patients with confirmed HCC lesions, we collected CEUS loops and quantified the vascular patterns of HCCs. Our quantification method consists of parametric processing of TICs to provide rise time (RT) and degree of washout (DW) metrics to capture the APHE and the washout parameters present in CEUS LI-RADS. Through quantification of these vascular characteristics and analysis utilizing parametric images, this process aims to assist in removing any subjectivity and inter-observer bias that might be present in the current qualitative implementation of LI-RADS.

## 3.2 Materials and Methods

### 3.2.1 *Patient HCC Data Collection*

Our institutional review board approved this prospective cross-sectional study (IRB ID: STUDY00012711), and contrast-enhanced ultrasound (CEUS) was performed in 31 HCC patients, from April 2021 to June 2022. Inclusion criteria include at least one lesion confirmed to be LI-RADS LR-5 by prior CT or MRI performed within 1 month of the ultrasound scan with no contraindication to CEUS (**Fig. 3.1**). All patients were above 18 years of age and written informed consent was provided. Patient demographics are listed in **Table 3.1**. The lesions were first identified in conventional B-mode ultrasound performed on a Philips EPIQ (Philips Medical Systems, Bothell, WA) with a C5-1 transducer (center frequency: 1.7 MHz, contrast mechanical

index: 0.06, contrast estimated peak negative pressure: 78 kPa, fundamental mechanical index: 0.05, fundamental estimated peak negative pressure: 65 kPa). The transducer was then spatially fixed with an articulated arm (Fisso, Baitella AG, Switzerland) (**Fig 3.2a**). The arm can be positioned anywhere on the patient that the sonographer would be able to scan freehand. A 1.2 mL bolus of Lumason contrast agent (Bracco Suisse SA, Geneva, Switzerland) followed by a 5 mL saline flush was intravenously injected, and a 5-minute intermittent video loop was collected while scanning the liver with a contrast-specific mode (amplitude modulation). The reported size distribution of Lumason microbubbles is 5.89 ± 3.07 μm diameter (mean ± SD) (16). In order to limit microbubble destruction, scanning was performed continuously for the first 90 seconds, and only for 15 seconds at the 2, 3, 4, and 5-minute mark (**Fig 3.2b**). The transducer was then repositioned to a new tumor plane (translated and/or rotated) and the process was repeated for a second injection. Lesion sizes were measured with image calipers, and the long axis in the contrast and fundamental image were recorded for each injection and averaged. The smallest measured lesion diameter was 13 mm, confirming all lesions were larger than the 10 mm size necessary for HCC lesions according to CEUS LI-RADS.

| Characteristic | No. Patients |
|---|---|
| Sex | |
| Male | 24 (77%) |
| Female | 7 (23%) |
| Age (mean ± SD) | 67 ± 6 y |
| Lesion diameter (mean ± SD) | 23 ± 8 mm |
| Imaging modality used for LI-RADS classification | |
| MRI | 18 |
| CT | 13 |

LI-RADS, Liver Imaging Reporting and Data System; MRI, magnetic resonance imaging; CT, computed tomography.

**Table 3.1**: Descriptive characteristics of the study group

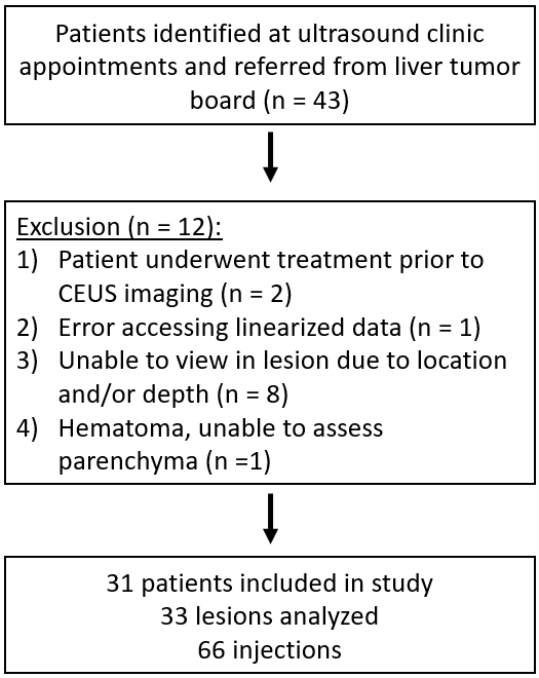


**Fig. 3.1**: Flowchart describing patient inclusion and exclusion criteria, and the resulting number of confirmed hepatocellular carcinoma (HCC) lesions utilized in this study.

### 3.2.2 *Quantitative HCC Analysis*

Analysis of HCC image loops, extracted as native DICOM data (17), was performed in a MATLAB based tool we developed titled "qDicomUW". Our tool operates on linearized data acquired via a proprietary data transformation script from Philips (Philips Healthcare, Bothell, WA). The DICOM loops from the 5-minute scan were first stitched together into a single loop where the time was continuously tracked even during the time when the scanner was frozen (this information is provided in the DICOM files). An automatic respiratory gating (ARG) algorithm (18, 19) formed a TIC from a generated ROI around a uniform bright interface in the fundamental image on a user-defined key frame with an optimal view of the lesion (**Fig. 3.2c,d**).

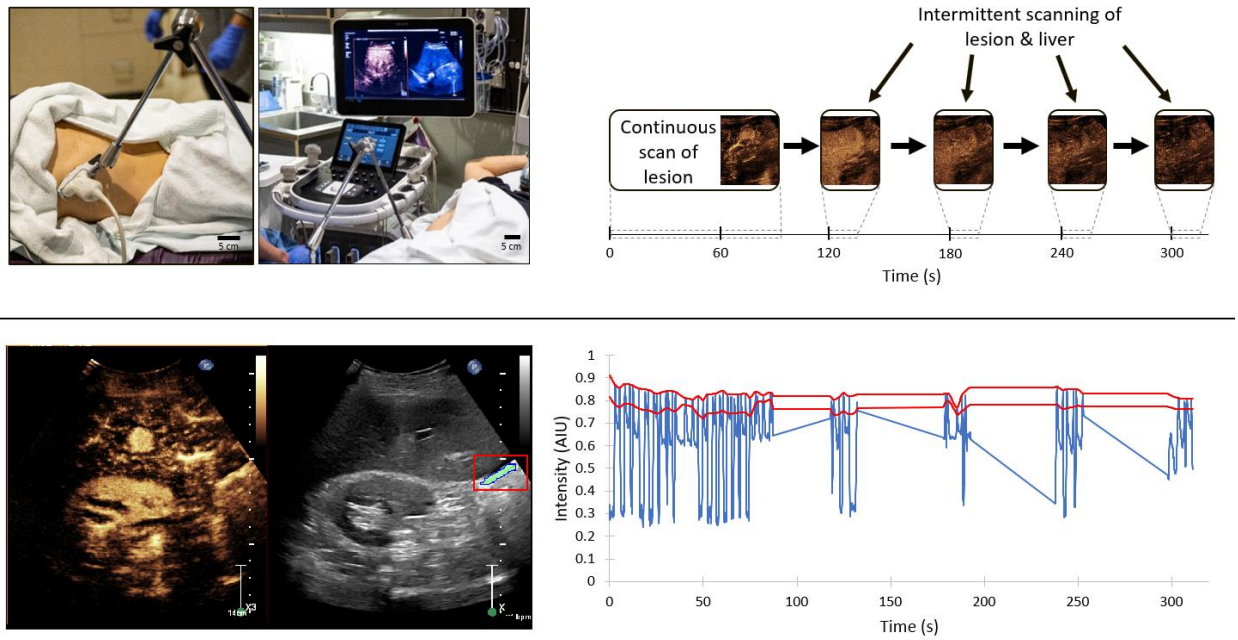


**Fig. 3.2**: Contrast-enhanced ultrasound data collection and processing overview. (a) Placement of an articulated arm holding an ultrasound probe onto to the patient. (b) A schematic illustrating the scanning sequence used for each injection. The contrast timer was started upon the injection of the bolus, at t = 0 on the time axis. A continuous 90 second capture was used to capture wash-in dynamics, and shorter (approximately 15 second) scans at 2, 3, 4, and 5 minutes were used to evaluate washout while limiting bubble destruction. (c) An example image with a bright moving feature automatically identified in the fundamental image to be tracked by the automatic respiratory gating (ARG) algorithm highlighted. (d) An example curve tracking the intensity of the region of interest (ROI) in (c) over time, and the corresponding frames that are preserved represented by the points on the blue time-intensity curve (TIC) within the red boundaries which correspond to a 15% intensity threshold to the local maxima of the TIC.

Variations in intensity in the TIC result from the bright interface moving in and out of the scan plane. Determined from previous work, a 15% intensity tolerance from the local maxima of the TIC was utilized to eliminate most of out-of-plane respiratory motion by removing frames where the intensity on the TIC fell below this threshold. To account for any remaining translation (in-plane motion), a motion compensation algorithm utilizing two-dimensional normalized cross-correlation on the fundamental image of the respiratory gated frames was used. The impact of ARG and motion compensation on the TIC extracted from a ROI around an HCC lesion is demonstrated in **Fig. 3.3a**. Oscillatory noise present in the TIC resulting from respiratory motion (**Fig. 3.3b**) is significantly reduced with ARG and motion compensation (**Fig. 3.3c**). Points within the same respiration were then averaged to smooth the TIC and further reduce the effect of motion noise on the extracted perfusion parameters (**Fig 3.3d**).

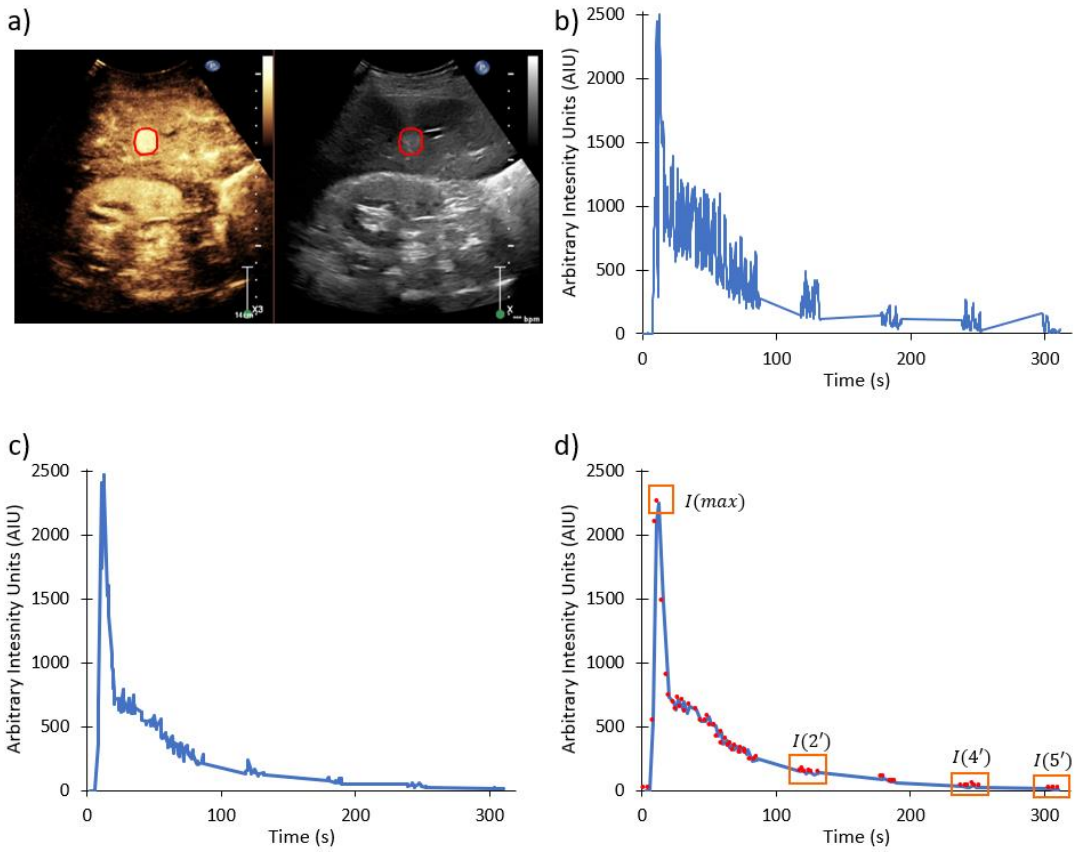


**Fig. 3.3**: Time intensity curve evolution with post-processing. (a) An example "side-side" image with a region of interest (ROI) drawn around the lesion in both the contrast and fundamental image. The extracted time intensity curve is shown in (b), after automated respiratory gating (ARG) and motion compensation in (c), and with ARG, motion compensation, and averaging of points per breathing cycle in (d). The intensity values utilized for degree of washout (DW) calculations are highlighted in (d).

A key aspect of our quantification algorithm is the use of parametric image processing, which calculates metrics throughout the duration of the loop across the whole image instead of only a single ROI. A 9-by-9-pixel (approximately 3x3 mm) ROI was translated in 3 pixel (approximately 1 mm) increments across the contrast image, and a TIC was generated for all ROIs from the ARG and motion compensated loop. The overlap of the ROI during the translation allowed for spatial averaging to further reduce noise due to motion without impacting feature resolution. To quantify the wash-in and washout dynamics associated with HCC lesions according to CEUS LI-RADS, $RT$ and $DW$ calculations were extracted from each TIC. $RT$ is defined as the elapsed time from when contrast first arrived in a ROI to its peak intensity. The $RT$ parameter provides information about the APHE as HCC lesions receive blood from the

hepatic artery tree as opposed to the surrounding liver where the portal vein supplies most of the blood volume. During an intravenous bolus injection, contrast first arrives to the liver from the hepatic artery and causes the early enhancement in HCC lesions, known as APHE. After a short delay, contrast arrives through the portal vein which primarily drives enhancement in the liver. This difference in wash-in dynamics between HCCs and the surrounding liver, or APHE, can be captured with $RT$. $DW$ can be calculated for any time point after the peak and attention is paid to 2-minute and 5-minute washout following the CEUS LI-RADS algorithm. When the contrast signal intensity of the liver ROI was very low and less than an acceptable threshold (3.5 linear intensity units above the noise floor at the 5-minute mark), the 4-minute was used instead. $DW$ was calculated for both the 2 and 5-minute washout for each TIC, defined as,

$$DW(t) = \frac{I(\max)}{I(t)} \quad (1)$$

where $I(t)$ is the linearized mean intensity at time $t$, and $t = 2'$ or $5'$ (**see Fig 3.3d**). Parametric images for $RT$ and $DW(2')$ and $DW(5')$ were generated for all injections. User-defined ROIs were then drawn around the lesion and liver parenchyma and automatically co-registered in all different types of images (fundamental, contrast and parametric), allowing for robust ROI placement and fine tuning. Mean and standard deviation values were calculated for each parametric image within these ROIs. $RT$, $DW(2')$, and $DW(5')$ values were averaged across injections for the same lesion. Relative degree of washout ($rDW$) at 2- and 5-minute washout was computed by the ratio between the mean tumor and liver parenchyma $DW$ defined as:

$$rDW = \frac{DW_{tumor}}{DW_{parenchyma}} \quad (2)$$

### 3.2.3 *Statistical Analysis*

To establish statistically significant differences in tumor and parenchyma $RT$, a Welch's t-test ($p<0.05$) was performed for each patient. For $rDW$ variability, data size was equalized utilizing bootstrapping methods (20), and a 95% confidence interval was calculated along with a respective p-value to ensure $rDW$ values were statistically significantly different than 1, or that washout of the lesion had occurred. The p-value was calculated as the following (21):

$$P = \exp(-0.717 * \left|\frac{LN(rDW_{avg})}{SE}\right| - 0.416 * \left|\frac{LN(rDW_{avg})}{SE}\right|^2) \quad (3)$$

To evaluate the reproducibility of these metrics, coefficient of variation (COV) was calculated for $RT$, $DW$, and $rDW$ between injections on the same patients and then averaged. A Spearman's rank correlation test to evaluate statistical dependence was performed between size, $RT$, $DW$, and $rDW$ values.

## 3.3 RESULTS

### 3.3.1 *Qualitative evaluation with CEUS images*

Conventional qualitative LI-RADS evaluation may be performed by inspecting contrast images at key time points from the 5-minute scan that highlight important vascular features of the HCCs and surrounding liver. **Fig. 3.4** shows two patient examples where the lesion is identified by a red ROI and sampled parenchyma with a white ROI. First, the APHE of the lesion is distinctly visualized as contrast initially arrives from the hepatic artery supply (**Fig. 3.4a,d**). Next, peak portal supply displays vascularization of the surrounding liver parenchyma as a majority of its vascular volume stems from the portal vein (**Fig. 3.4b,e**). At the 5-minute timepoint, mild or moderate inhomogeneous washout of the lesion as compared to the surrounding liver can be seen (**Fig. 3.4c,f**).

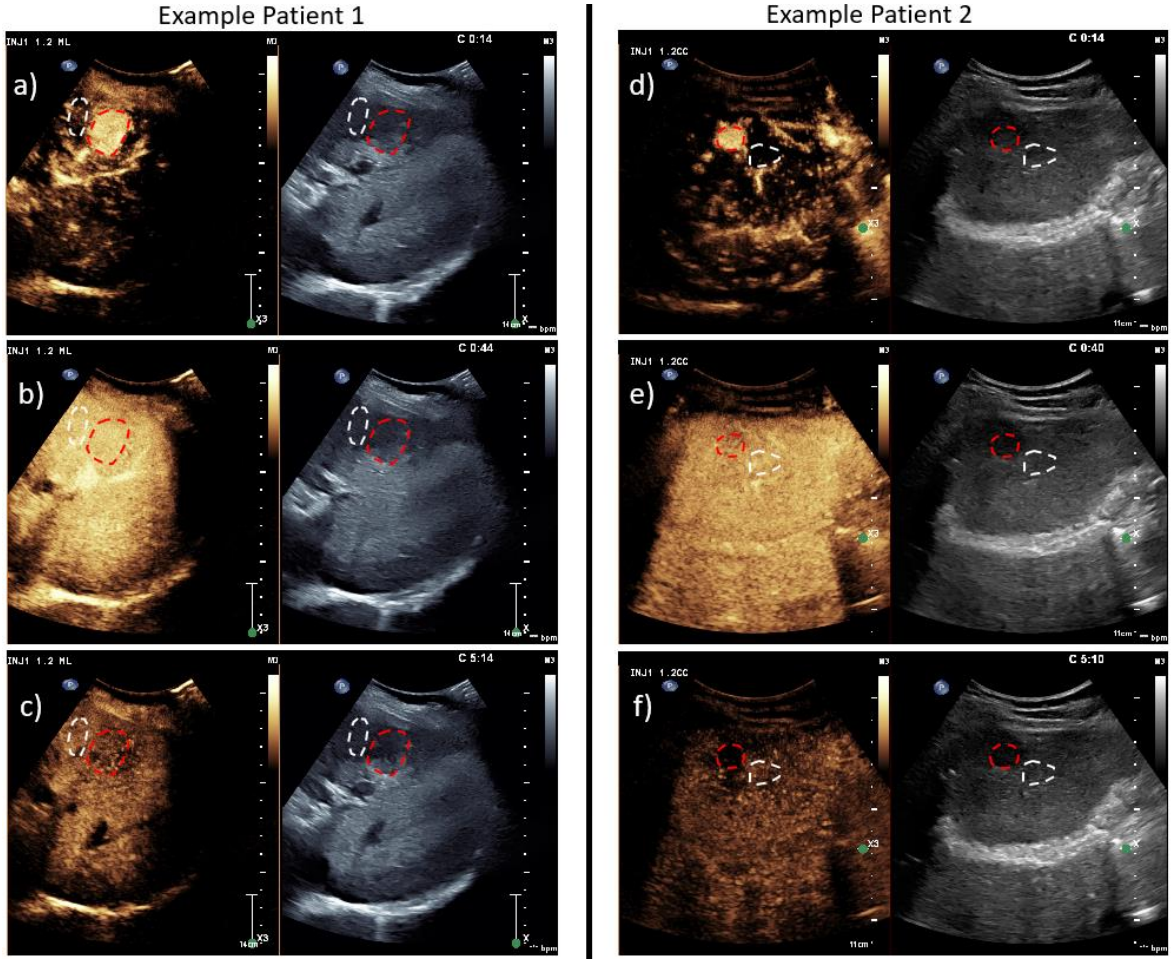


**Fig. 3.4**: Contrast-enhanced ultrasound (CEUS) and conventional B-mode images for two example hepatocellular carcinoma (HCC) patients at three timepoints throughout the scan: the peak of the arterial phase (a,d), the peak of the portal phase (b,e), and the late phase (c,f). The red regions of interests (ROIs) are placed around the lesion, while the white ROIs are placed at a similar depth as the lesion and sample the surrounding parenchyma.

### 3.3.2 *Parametric Processing*

Parametric images for $RT$, $DW(2')$ and $DW(5')$ were generated for all injections to capture the wash-in and washout vascular dynamics of HCCs identified by LI-RADS and visualized qualitatively in the CEUS data (**Fig. 3.5**). The parametric images shown in **Fig. 3.5** are from the same lesions shown in **Fig. 3.4** and present information from the whole 5-minute loops as a single image, and also have a red ROI surrounding the lesion and a white ROI around a homogenous portion of the parenchyma. $RT$ of each 9x9 pixel ROI's TIC captures the early wash-in of the HCC lesion compared to its surrounding liver (**Fig. 3.5a,d**). The tumor shows as a lower value in the parametric image (blue tumor versus green-yellow parenchyma),

demonstrating its shorter $RT$ and hence APHE. The degree of washout, $DW$, which is a ratio of the average linearized tumor peak intensity and parenchyma intensity at the 2-minute (**Fig. 3.5b,e**) or 5-minute (**Fig. 3.5c,f**) timepoint of each TIC in accordance with CEUS LI-RADS, captures and quantifies the washout characteristic of these tumors. In both patients, washout of the lesion can be visualized with greater $DW$ parametric values (red/yellow) in comparison to lower $DW$ values of the surrounding parenchyma (blue).

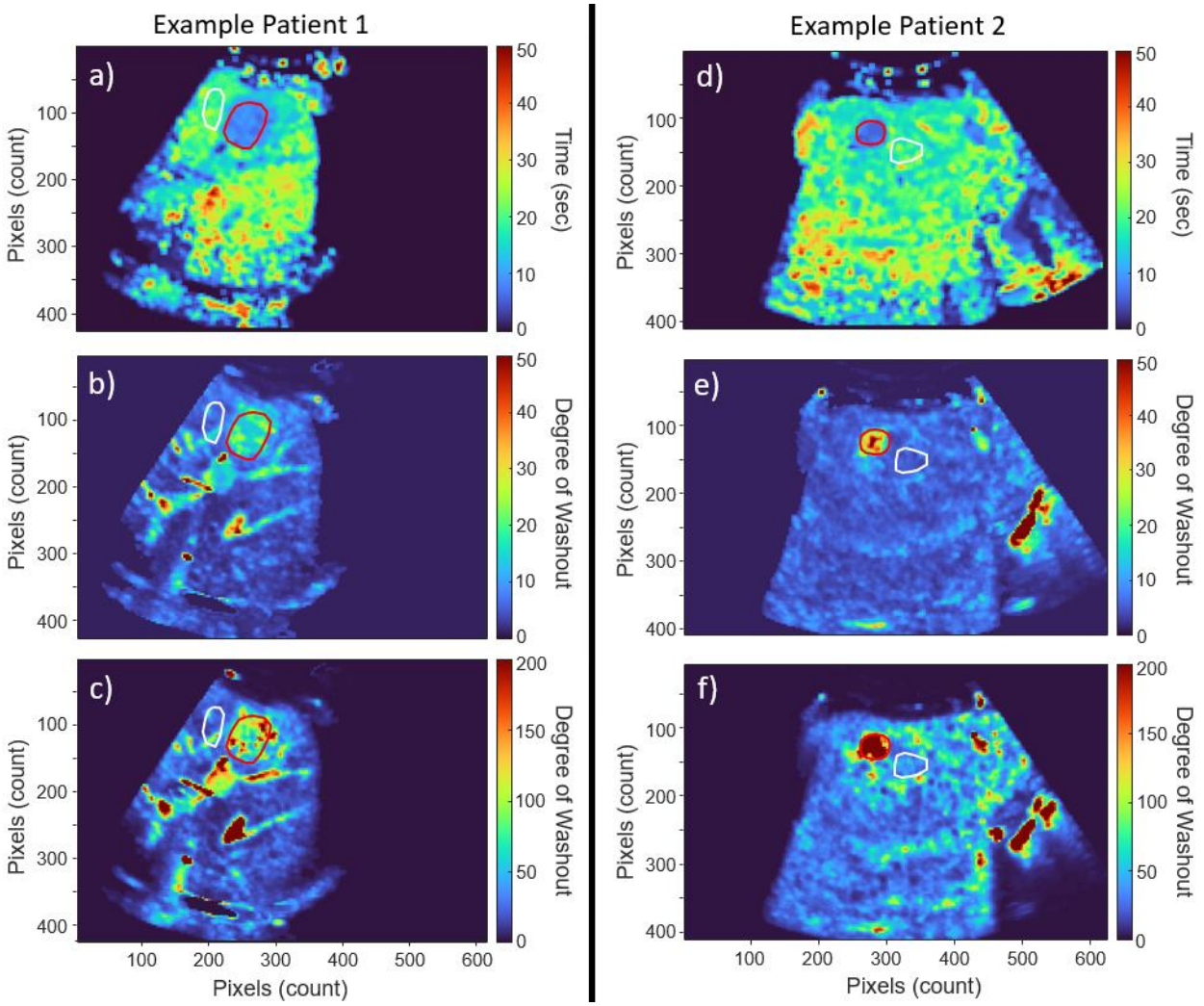


**Fig. 3.5**: Parametric images of rise time ($RT$) and degree of washout ($DW$) for the same two example patients used in Fig. 2.4. $RT$ is shown in (a,d), $DW$ at 2 minutes is shown in (b,e), and $DW$ at 5 minutes is shown in (c,f). The red regions of interests (ROIs) are placed around the lesion, while the white ROIs are placed at a similar depth as the lesion and sample the surrounding parenchyma.

### 3.3.3 *Quantification of Vascular Parameters*

Wash-in of the evaluated HCCs from all patients was captured through $RT$ for both the lesion and surrounding liver parenchyma (**Fig. 3.6**). Notably, the lesion $RT$ was considerably smaller and statistically different ($p<0.05$) than the surrounding parenchyma for all lesions and indicates that APHE is present, an anticipated and required criteria for a lesion to be categorized as LR-5 (22).

The relative degree of washout $rDW$ at both 2-minutes and 5-minutes, are displayed in **Fig. 3.7a and 3.7b**, respectively, for all patients. The dotted grey lines present at an $rDW$ value of 1 indicate the threshold for the lesion to have washout relative to the surrounding parenchyma. All lesions presented a relative degree of washout value that was significantly greater than 1 ($p < 0.05$) at both the 2 and 5-minute timepoints, capturing the characteristic feature of washout required for LR-5 classified HCCs. The dotted blue lines were placed an $rDW$ value of 4, as this represents a 6-decibel difference in intensity and is where washout could be visualized qualitatively. This threshold could be used to stratify $rDW$ values into mild and moderate degrees. The patients in **Figs. 3.4 and 3.5** correspond to patients 10 and 23 in **Figs. 3.6 and 3.7**.

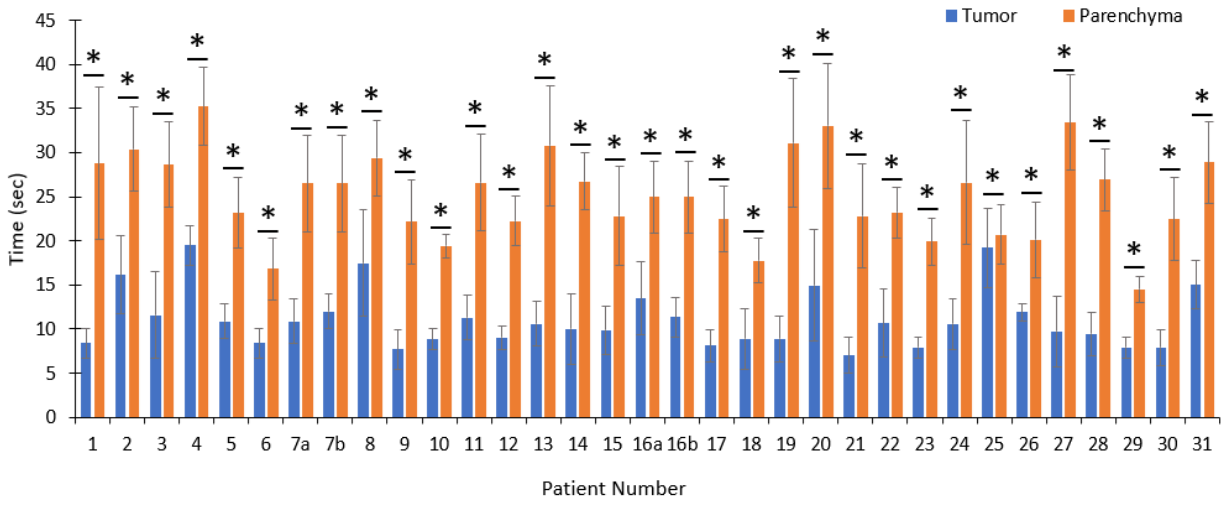


**Fig. 3.6**: Bar plots of rise time ($RT$) values extracted from all patients. (a) Average $RT$ of tumor (blue) and surrounding parenchyma (orange) for each patient. All tumor and parenchyma $RT$ pairs had a statistically significant difference (Welch's t-test, $p<0.05$).

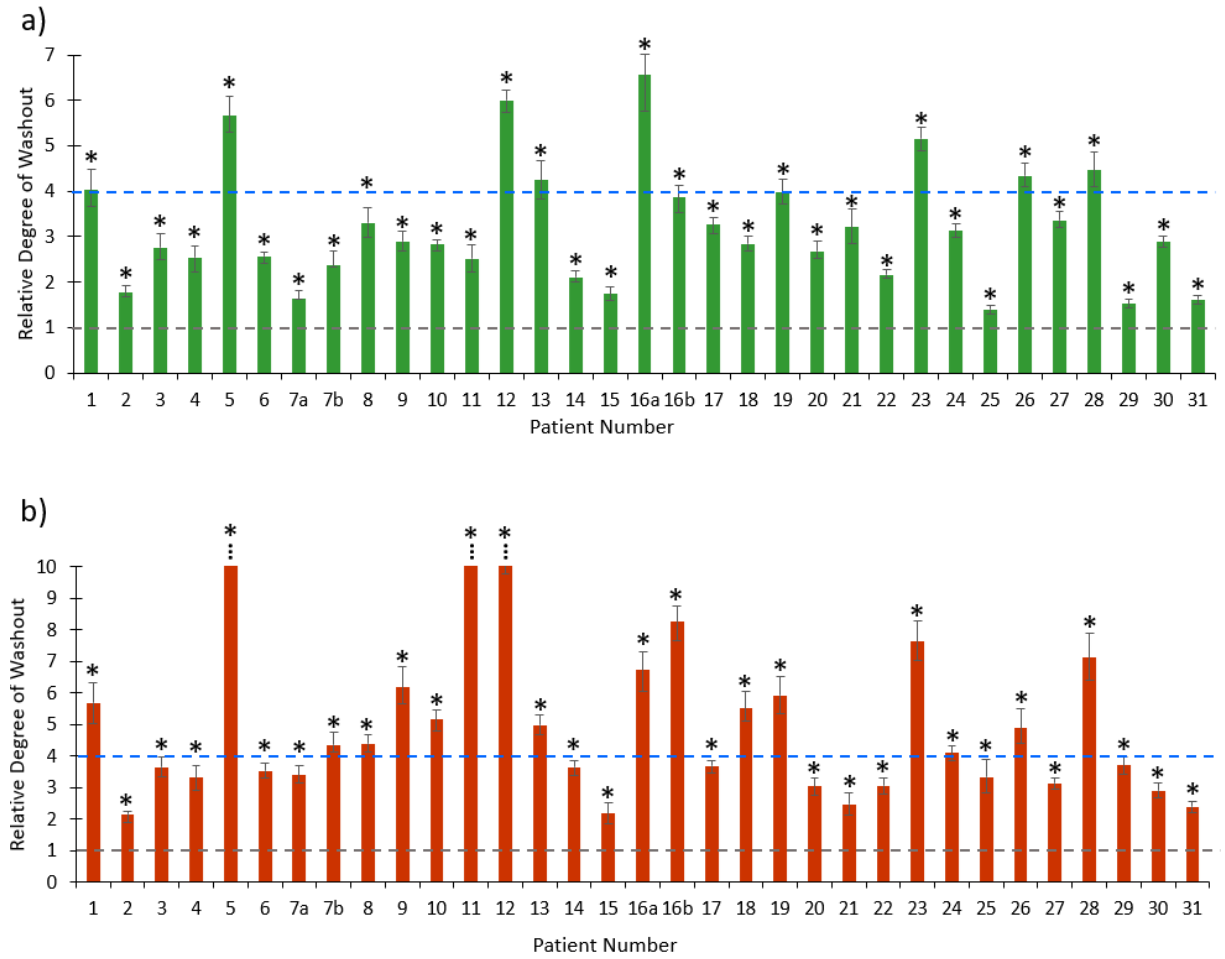


**Fig. 3.7**: Bar plots of relative degree of washout ($rDW$) values extracted from all patients. (a) $rDW$ values at the 2-minute timepoint. All lesions demonstrated statistically significant ($p<0.05$) washout ($rDW > 1$), represented by the grey dashed line. A threshold for stratifying mild and moderate washout is shown by the blue dashed line, placed at an $rDW$ value of 4 and corresponds to a 6-decibel difference. (b) $rDW$ at the 5-minute timepoint. All lesions still exhibited statistically significant washout ($p<0.05$), and the same grey and blue dashed lines are displayed.

As a measure of the reproducibility of our method, we present average inter-injection COV of $RT$ and $rDW$ for all patients in **Table 3.2**. The COV of $RT$ for the lesion and surrounding parenchyma was about 11% and the COV of $DW(2')$, $DW(5')$ , $rDW(2')$, and $rDW(5')$ were all 22-31%. Spearman's rank correlation results for size showed no significant relationship to our extracted perfusion parameters, and results are present in **Table 3.3**. However, Spearman's rank correlation found a significant relationship between lesion and parenchyma $RT$, and between lesion $RT$ and lesion $DW(2')$ and $DW(5')$ ($p < 0.05$), present in **Table 3.4**.

| | *RT* | *DW*(2′) | *DW*(5′) | *rDW*(2′) | *rDW*(5′) |
|---|---|---|---|---|---|
| HCC lesion COV | 11% | 29% | 31% | 28% | 30% |
| Parenchyma COV | 11% | 22% | 28% | | |

HCC, hepatocellular carcinoma; COV, coefficient of variation; *RT*, rise time; *DW*(2′), degree of washout at 2 minutes; *DW*(5′), degree of washout at 5 minutes; *rDW*(2′), relative degree of washout at 2 minutes; *rDW*(5′), relative degree of washout at 5 minutes.

**Table 3.2**: Average inter-injection coefficient of variation values

| | **Spearman Correlation Coefficient** | ***P* (α = 0.05)** |
|---|---|---|
| Lesion size and lesion *RT* | −0.13 | 0.47 |
| Lesion size and parenchyma *RT* | 0.11 | 0.55 |
| Lesion size and lesion *DW*(2′) | 0.25 | 0.16 |
| Lesion size and lesion *DW*(5′) | 0.17 | 0.35 |
| Lesion size and *rDW*(2′) | 0.26 | 0.15 |
| Lesion size and *rDW*(5′) | 0.26 | 0.14 |

No statistically significant results were observed ( $P < 0.05$).

*RT*, rise time; *DW*(2′), degree of washout at 2 minutes; *DW*(5′), degree of washout at 5 minutes; *rDW*(2′), relative degree of washout at 2 minutes; *rDW*(5′), relative degree of washout at 5 minutes.

**Table 3.3**: Spearman's rank correlation results utilizing lesion size.

| | **Spearman Correlation Coefficient** | ***P* (α = 0.05)** |
|---|---|---|
| Lesion *RT* and parenchyma *RT* | 0.49 | 0.003 |
| Lesion *RT* and lesion *DW*(2′) | −0.46 | 0.007 |
| Lesion *RT* and lesion *DW*(5′) | −0.61 | 0.0001 |
| Lesion *RT* and *rDW*(2′) | −0.26 | 0.15 |
| Lesion *RT* and *rDW*(5′) | −0.18 | 0.3 |

Significant results were observed for lesion rise time (*RT*) and parenchyma *RT*, and between lesion *RT* and lesion degree of washout at the 2-minute (*DW*(2′)) and 5-minute (*DW*(5′)) time points.

*rDW*(2′), relative degree of washout at 2 minutes; *rDW*(5′), relative degree of washout at 5 minutes.

**Table 3.4**: Spearman's rank correlation results between vascular parameters.

## 3.4 DISCUSSION

One key issue when implementing CEUS LI-RADS is the need to collect data from a single plane of the tumor over the course of 5 minutes, the specified time by LI-RADS. The use of the articulated arm to hold the transducer not only greatly assisted in the qualitative LI-RADS evaluation, but it also proved vital for the systematic quantification of 2D CEUS data. It enabled us to accurately track the lesion while moving due to respiration during the 5-minute scan and greatly improved the accuracy and reproducibility of our quantifiable metrics, namely $RT$, $DW$ and $rDW$. With several degrees of freedom, the articulated arm does not limit CEUS data collection based on position or depth beyond the existing limitations of CEUS (i.e. if the lesion can be scanned freehand then it is able to be scanned with the articulated arm). We opted for a scanning protocol that was not continuous over this time in order to preserve injected microbubbles. Intermittent scanning at each minute mark after the first 90 seconds was selected since the image intensity in the TIC is very slowly decreasing during the late portal phase. These intermittent captures were performed on the minute mark to ensure the capture the of 2-minute and 5-minute timepoints specified in CEUS LI-RADS for evaluating the washout. Use of other commercial microbubbles such as Sonazoid, which has a higher destruction threshold and persists in the liver longer, could allow for alterations to this scanning scheme. Previous CEUS quantification attempts for HCC with freehand scanning were limited to shorter continuous scan times that are inadequate for HCC characterization (12). The articulated arm alleviates the above challenges and allows for the proper correction of respiratory motion. In our analysis, automatic respiratory gating (19, 23) was first used to remove out-of-plane motion, and then motion compensation was performed to eliminate any remaining translational motion to enable the generation of accurate TICs. Other groups have implemented advanced motion compensation algorithms with freehand scanning (14, 15), but their results have been impacted by unwanted probe motion (e.g., sliding) that introduces changes of the scan plane during data collection.

Parametric processing generates images of a TIC (bolus transit) parameter, for example $RT$, by implementing the TIC analysis on all pixels instead of just an ROI. This process provides increased spatial information through better delineated feature boundaries and captures spatial variability via standard deviation of the user defined ROI. Through the overlapping of the 9x9

pixel ROIs performing TIC analysis, any residual effects of motion on the extracted values were reduced by averaging. The final parameter extraction is done by the segmentation of the tumor from all the available images: (a) the B-mode tissue image (when the tumor is visible), (b) the contrast image at the peak of the APHE, and (c) the parametric images of $RT$ and $DW$ (see **Figs. 3.4-3.5**). Our software allows the automatic placement and duplication of the selected ROI in all images, and by moving or adjusting a ROI in one image type the adjustment is translated in all.

In CEUS LI-RADS, APHE and washout are the two main qualitative metrics of HCC. The APHE of HCC is reasoned to be the result of its primary blood supply from the hepatic artery, unlike the rest of the liver which receives the majority of its blood from the portal vein (24, 25). This leads to HCC enhancing before the rest of the liver and it is accurately captured by the $RT$ parameter which provides a quantifiable measure of APHE. In all patients, $RT$ was significantly shorter for the tumor as compared to the surrounding liver, as expected. The higher variability in $RT$ of the liver parenchyma between patients compared to that of the HCC lesions can be attributed to varying degrees of cirrhosis, cardiac output, and differences in disease etiology. The slow HCC washout (26) has been challenging to observe in the past due to the necessary long evaluation, microbubble destruction, and difficulty to maintain the image plane. With the robustness of our imaging protocol, we were able to systematically quantify washout with $DW$ and $rDW$ for first time. A threshold at an $rDW$ value of 4, corresponding to a 6-decibel difference in intensity, was included to identify where qualitative visualization of washout could likely occur. This could be utilized to stratify values in mild and moderate degrees of washout, and could be explored more extensively in future quantitative studies. Washout in HCC is heterogenous as a result of variability in cellular differentiation, so lesions are more accurately evaluated on an individual basis relative to the surrounding liver and at early and late timepoints (6, 27).

This present study focused on the quantification of perfusion parameters in confirmed HCC lesions to ensure the technique provides consistent and expected results for the characterization of these tumors. We were able to robustly capture the APHE and washout of HCCs with the quantifiable measures of $RT$, $DW$ and $rDW$. To evaluate the inter-injection variability of these metrics, we calculated the COV between 2 injections, which for $RT$ was about 11% and for the

washout parameters was 22-31%. These COV ranges for temporal and intensity-based metrics are similar to those evaluated in previous in-vitro studies (28). The reproducibility of these metrics is critical for designating what constitutes a true change in longitudinal evaluations of tumor blood flow in possible future studies. The reproducibility of CEUS quantification metrics for the liver has also been the focus for recent Quantitative Imaging Biomarker Alliance (QIBA) of the Radiological Society of North America (RSNA) efforts (29).

Through quantification, we were also able to initially investigate how morphological and perfusion characteristics attributed to HCC are related in clinical data. No significant relationships were found between size and any extracted perfusion metrics (**Table 3.3**), a similar result to other CEUS studies evaluating perfusion in HCC (30). However, significant dependence between perfusion metrics were observed (**Table 3.4**). Lesion $RT$ and parenchyma $RT$ showed a significant relationship ($p < 0.05$), suggesting that greater arterialization of the liver, possibly resulting from a higher degree of cirrhosis, is also reflected in HCC lesions. Significant relationships between lesion $RT$ and lesion $DW(2')$ and $DW(5')$ were also observed ($p < 0.05$), indicating the $RT$ could act as a predictor for the magnitude and onset of washout, a parameter that is much more challenging to visualize. These initial observations could be explored further in larger clinical studies, incorporating disease etiology and cirrhosis grading.

Another key element of our quantification approach is the elimination of the need to use a curve fit model during TIC analysis. Typical TIC analysis requires the use of a curve fit model based on indicator dilution in order to remove excessive noise due to motion and other factors in the TICs (31). The use of curve fit models has been the source of differences between the results of different sites/vendors (28). Since our method produces TICs with very little noise due to the use of the articulated arm and the motion compensation post-processing, the quantifiable metrics for the HCC vascular patterns, i.e., $RT$ and $rDW$, are extracted directly from the actual data. A step towards standardization is the use of parametric processing for calculating the quantifiable metrics. Instead of analyzing just two ROIs in the contrast image, the whole image is processed and with possible future advances in artificial intelligence and machine learning, automatic segmentation of the lesion might be feasible. These elements combined can lead to automated LI-RADS implementation.

In future work we also aim to apply this technique to LR-3 and LR-4 patients (who do not have confirmed HCC) and follow them with the current standards (LI-RADS) over time, to evaluate the sensitivity and specificity of our method and its ability to identify early HCCs. For example, LR-4 lesions which have no APHE with the current qualitative implementation might actually have measurable APHE (deduced from $RT$). In addition, LR-3 and LR-4 lesions with no washout of any type, when qualitatively evaluated, might actually have measurable washout according to the $DW$ and $rDW$ metrics which would classify them as LR-5, leading to earlier diagnosis. Beyond HCC, recent successful developments with immune checkpoint inhibitors (ICIs) allow for better outcomes for advanced stage HCC patients (32), and robust and precise treatment monitoring for patients undergoing systemic immunotherapy is essential. Our method is ideally positioned to evaluate changes in the tumor vascular patterns in patients undergoing therapies that may alter the tumor vasculature to accurately monitor response. Assessment of tumor blood flow changes in response to therapy with the methods described in the present study may also be performed for other tumors besides HCC.

This newly defined method has potential for augmenting and possibly improving the clinical evaluation of CEUS LI-RADS through quantification, but there are also some limitations. A limitation of CEUS is penetration depth, which can make evaluation of deep lesions challenging. Although this problem was more prominent in the past, newer scanners have extended CEUS penetration depth to 15 cm or more. Microbubble sensitivity is also expected to increase in the future with the use of monodisperse microbubbles currently being evaluated (33, 34) to address the penetration issue. Another limitation of this technique is the lack of standardization of machine settings among commercial ultrasound scanners. Differences in scanner settings (nonlinear pulsing scheme, gain, dynamic range, etc.) can result in producing different TICs and possibly influencing the perfusion metrics derived from them. Comparison of these perfusion metrics across scanners remains challenging (28). Finally, despite our robust imaging protocol and analysis method, evaluating a 2D scan plane of the lesion is another limitation. HCCs and many other solid tumors are heterogenous masses and their dynamic vascular patterns may be different in different planes. We currently address this issue by repeating the injection and evaluating different planes. 3D CEUS could overcome these limitations by capturing the whole

tumor and such technology is now starting to be clinically available. A major limitation at the present time is that collecting and saving 3D CEUS data in 10 Hz volume rates over 5 minutes is not clinically available.

In conclusion, we have developed a robust and reproducible scanning protocol and analysis method for the quantitative assessment of the dynamic vascular patterns of HCCs from CEUS for implementing CEUS LI-RADS quantitatively. We were able to quantitatively capture APHE through $RT$, a required CEUS feature for HCC diagnosis with CEUS LI-RADS. Importantly, we also quantified the washout of these lesions through $DW$ and $rDW$, a parameter which was previously only evaluated qualitatively in CEUS LI-RADS. Through this quantitative parametric analysis, we aim to reduce subjectivity of ROI selection, assist in removing observer bias, and provide metrics to clinicians to potentially improve the sensitivity of CEUS LI-RADS.

## 3.5 ACKNOWLEDGMENTS

Research was supported from the Brotman Baty Institute (BBI 683886 CC12), the National Center for Advancing Translational Sciences of the National Institutes of Health under award number TL1TR002318 (Krolak), and the National Institute of Biomedical Imaging and Bioengineering of the National Institutes of Health under award number R01EB032655. We also acknowledge the support of Dr. Thanasis Loupas with discussions on motion compensation and Gerald Harrison with the extraction of linearized data from native DICOM files, both from Philips Healthcare.

## 3.6 REFERENCES

1. McGlynn KA, Petrick JL, El-Serag HB**.** Epidemiology of Hepatocellular Carcinoma. Hepatology. 2021;73 Suppl 1(Suppl 1):4-13.
2. Hu J, Bhayana D, Burak KW, Wilson SR**.** Resolution of indeterminate MRI with CEUS in patients at high risk for hepatocellular carcinoma. Abdom Radiol (NY). 2020;45(1):123-33.
3. Mitchell DG, Bruix J, Sherman M, Sirlin CB**.** LI-RADS (Liver Imaging Reporting and Data System): summary, discussion, and consensus of the LI-RADS Management Working Group and future directions. Hepatology. 2015;61(3):1056-65.
4. Chernyak V, Fowler KJ, Do RKG, et al. LI-RADS: Looking Back, Looking Forward. Radiology. 2023;307(1):e222801.
5. Cunha GM, Fowler KJ, Roudenko A, et al. How to Use LI-RADS to Report Liver CT and MRI Observations. RadioGraphics. 2021;41(5):1352-67.
6. Bartolotta TV, Terranova MC, Gagliardo C, Taibbi A**.** CEUS LI-RADS: a pictorial review. Insights Imaging. 2020;11(1):9.

7. Wilson SR, Feinstein SB. Introduction: 4th Guidelines and Good Clinical Practice Recommendations for Contrast Enhanced Ultrasound (CEUS) in the Liver-Update 2020 WFUMB in Cooperation with EFSUMB, AFSUMB, AIUM and FLAUS. Ultrasound Med Biol. 2020;46(12):3483-4.
8. Burak KW, Douglas L, Congly SE. Comparing Magnetic Resonance Imaging and Contrast-Enhanced Ultrasound (CEUS) for the Characterization of Nodules Found on Hepatocellular Carcinoma Surveillance: CEUS is Our Clear Choice. J Ultrasound Med. 2023;42(6):1175-80.
9. Hu J, Burrowes DP, Caine BA, et al. Nodules Identified on Surveillance Ultrasound for HCC. Journal of Ultrasound in Medicine. 2023;42(6):1181-90.
10. Egger C, Goertz RS, Strobel D, et al. Dynamic contrast-enhanced ultrasound (DCE-US) for easy and rapid evaluation of hepatocellular carcinoma compared to dynamic contrast-enhanced computed tomography (DCE-CT)--a pilot study. Ultraschall Med. 2012;33(6):587-92.
11. Peng S, Ding H, Fu T, et al. Savitzky-Golay filter based contrast-enhanced ultrasound quantification in hepatic tumors: Methodology and its correlation with tumor angiogenesis. Clin Hemorheol Microcirc. 2019;73(2):271-82.
12. Wildner D, Pfeifer L, Goertz RS, et al. Dynamic contrast-enhanced ultrasound (DCE-US) for the characterization of hepatocellular carcinoma and cholangiocellular carcinoma. Ultraschall Med. 2014;35(6):522-7.
13. Yue WW, Wang S, Xu HX, et al. Parametric imaging with contrast-enhanced ultrasound for differentiating hepatocellular carcinoma from metastatic liver cancer. Clin Hemorheol Microcirc. 2016;64(2):177-88.
14. Tiyarattanachai T, Turco S, Eisenbrey JR, et al. A Comprehensive Motion Compensation Method for In-Plane and Out-of-Plane Motion in Dynamic Contrast-Enhanced Ultrasound of Focal Liver Lesions. Ultrasound Med Biol. 2022;48(11):2217-28.
15. Wan P, Chen F, Shao W, et al. Irregular Respiratory Motion Compensation for Liver Contrast-Enhanced Ultrasound via Transport-Based Motion Estimation. IEEE Trans Ultrason Ferroelectr Freq Control. 2021;68(4):1117-30.
16. Keller SB, Sheeran PS, Averkiou MA. Cavitation Therapy Monitoring of Commercial Microbubbles With a Clinical Scanner. IEEE Trans Ultrason Ferroelectr Freq Control. 2021;68(4):1144-54.
17. Dietrich CF, Averkiou MA, Correas JM, et al. An EFSUMB introduction into Dynamic Contrast-Enhanced Ultrasound (DCE-US) for quantification of tumour perfusion. Ultraschall Med. 2012;33(4):344-51.
18. Christofides D, Leen E, Averkiou M. Automatic respiratory gating for contrast ultrasound evaluation of liver lesions. IEEE Trans Ultrason Ferroelectr Freq Control. 2014;61(1):25-32.
19. Christofides D, Leen EL, Averkiou MA. Improvement of the accuracy of liver lesion DCEUS quantification with the use of automatic respiratory gating. Eur Radiol. 2016;26(2):417-24.
20. Haukoos JS, Lewis RJ. Advanced statistics: bootstrapping confidence intervals for statistics with "difficult" distributions. Acad Emerg Med. 2005;12(4):360-5.
21. Altman DG, Bland JM. How to obtain the P value from a confidence interval. Bmj. 2011;343:d2304.
22. Kim TK, Noh SY, Wilson SR, et al. Contrast-enhanced ultrasound (CEUS) liver imaging reporting and data system (LI-RADS) 2017 - a review of important differences compared to the CT/MRI system. Clin Mol Hepatol. 2017;23(4):280-9.
23. Averkiou M, Lampaskis M, Kyriakopoulou K, et al. Quantification of tumor microvascularity with respiratory gated contrast enhanced ultrasound for monitoring therapy. Ultrasound Med Biol. 2010;36(1):68-77.
24. Fournier LS, Cuenod CA, de Bazelaire C, et al. Early modifications of hepatic perfusion measured by functional CT in a rat model of hepatocellular carcinoma using a blood pool contrast agent. Eur Radiol. 2004;14(11):2125-33.
25. Choi J-Y, Lee J-M, Sirlin CB. CT and MR Imaging Diagnosis and Staging of Hepatocellular Carcinoma: Part II. Extracellular Agents, Hepatobiliary Agents, and Ancillary Imaging Features. Radiology. 2014;273(1):30-50.
26. Wilson SR, Burns PN, Kono Y. Contrast-Enhanced Ultrasound of Focal Liver Masses: A Success Story. Ultrasound Med Biol. 2020;46(5):1059-70.
27. Bhayana D, Kim TK, Jang HJ, et al. Hypervascular liver masses on contrast-enhanced ultrasound: the importance of washout. AJR Am J Roentgenol. 2010;194(4):977-83.
28. Averkiou MA, Juang EK, Gallagher MK, et al. Evaluation of the Reproducibility of Bolus Transit Quantification With Contrast-Enhanced Ultrasound Across Multiple Scanners and Analysis Software Packages-A Quantitative Imaging Biomarker Alliance Study. Invest Radiol. 2020;55(10):643-56.
29. RSNA 2023;Pages. Accessed at https://qibawiki.rsna.org/index.php/Ultrasound_CEUS_BC.

30. Yang D, Li R, Zhang X-H, et al. Perfusion Characteristics of Hepatocellular Carcinoma at Contrast-enhanced Ultrasound: Influence of the Cellular differentiation, the Tumor Size and the Underlying Hepatic Condition. Scientific Reports. 2018;8(1):4713.
31. Strouthos C, Lampaskis M, Sboros V, et al. Indicator dilution models for the quantification of microvascular blood flow with bolus administration of ultrasound contrast agents. IEEE Trans Ultrason Ferroelectr Freq Control. 2010;57(6):1296-310.
32. Pinter M, Scheiner B, Peck-Radosavljevic M**.** Immunotherapy for advanced hepatocellular carcinoma: a focus on special subgroups. Gut. 2021;70(1):204-14.
33. Frinking P, Segers T, Luan Y, Tranquart F**.** Three Decades of Ultrasound Contrast Agents: A Review of the Past, Present and Future Improvements. Ultrasound Med Biol. 2020;46(4):892-908.
34. Stride E, Segers T, Lajoinie G, et al. Microbubble Agents: New Directions. Ultrasound Med Biol. 2020;46(6):1326-43.

# Chapter 4. ULTRASOUND CAVITATION THERAPY: INDUCING TUMOR DRUG DELIVERY AND BLOOD FLOW CHANGES WITH CLINICAL ULTRASOUND TOOLS

Connor Krolak, Lance De Koninck, Sherry Gu, Yak-Nam Wang, Jeffry E Powers, Michalakis Averkiou

*Journal of Controlled Release. 2026 Feb 23; Vol 393.*

**Abstract**

Hepatocellular carcinoma (HCC), the fourth leading cause of cancer-related deaths, remains difficult to treat due to underlying liver disease, abnormal tumor vasculature, elevated interstitial fluid pressure (IFP), and immune suppression. We developed a theranostic approach using ultrasound cavitation with a clinical scanner and FDA-approved microbubbles to enhance vascular permeability and drug delivery in HCC. Acute experiments were performed in a subcutaneous HCC mouse model using a modified Philips EPIQ scanner and S5–1 phased-array probe under two conditions: moderate (1.6 MPa) and high (2.2 MPa) peak negative pressures. Contrast-enhanced ultrasound was acquired before, during, and after treatment, and vascular changes were quantified using a novel maximum intensity projection time area curve (MIP-TAC) analysis. Passive cavitation detection monitored microbubble activity. Doxorubicin extravasation, IFP (with a pressure catheter), and histology were assessed. Both ultrasound conditions induced transient tumor perfusion loss and reduced IFP without significant tissue damage or hemorrhage. The high-pressure treatment caused the greatest perfusion loss, whereas enhanced doxorubicin delivery occurred under moderate pressure. This result is likely due to excessive tumor perfusion loss in the high-pressure group, impeding further drug transport. These results demonstrate the feasibility of therapeutic cavitation with longer than previously evaluated acoustic pulses (1000 cycles) on a clinical scanner and clinically-approved microbubbles in HCC. Moderate-pressure cavitation maximized drug extravasation, underscoring the need to balance transient tumor perfusion loss with drug delivery. This clinically translatable strategy has potential to improve therapeutic outcomes in human HCC.

## 4.1 INTRODUCTION

Hepatocellular carcinoma (HCC) is the seventh most commonly occurring cancer and fifth leading cause of cancer-related deaths [1]. Despite advancements in interventional cancer therapies and plethora of systemic drug options, poor prognosis persists partially due to delays in diagnosis, pre-existing liver disease, and a lack of currently effective treatments. Risk factors for this disease include Hepatitis B and C, alcoholic liver disease, and non-alcoholic steatohepatitis. As a result, conventional treatments are limited by existing damage to the surrounding liver, and more targeted treatments are necessary.

Ultrasound-mediated microbubble cavitation, or the use of focused ultrasound and microbubbles, presents a controlled and targeted approach able to modulate the tumor microenvironment [2–5]. Cavitation, or the rapid expansion and contraction of microbubbles in response to ultrasound, can mechanically interact with surrounding tissues to induce a wide array of bioeffects. Interestingly, the unique vascular network found within tumors, particularly the small, immature, and improperly developed vessels, have been found to be more susceptible to mechanical stimuli induced by microbubble cavitation, and several works have observed alterations in blood flow over a variety of pressures [6–8]. Studies have also demonstrated that these events can be tumor specific, sparing surround tissues [9].

However, transient hypoxia alone can introduce a more proliferative phenotype in residual tumor cells [10,11], indicating that cavitation treatments could benefit from use in tandem with another anti-tumor approach. Typically, highly angiogenic tumors like HCC experience enhanced permeability and retention which contribute to increased interstitial fluid pressure [12]. This pressure differential creates a gradient that limits drug penetration within the tumor, contributing to their reduced efficacy. Fortunately, ultrasound cavitation treatments have also demonstrated the ability to improve drug penetration into solid tumors [7,13–16], possibly resulting from mechanical modulations of the tumor microenvironment. However, the extent of these cavitation treatments in terms of their ability to alter tumor blood flow and impact drug uptake is a complex phenomenon that could be further characterized to optimize treatments, and clinical translation of many existing studies is partly limited by use of specialized experimental hardware.

Diagnostic ultrasound scanners are very prevalent in clinical diagnosis, but are highly optimized in terms of their parameter space (beamforming, number of cycles, pressure/voltage, and frequency) for imaging in humans. Despite not being able to produce pulses which induce bioeffects with ultrasound alone, such as ablation in high-intensity focused ultrasound, these systems are able to be modified to supply pressures which can result in inertial cavitation of microbubbles [7,17–20]. Implementation of microbubble cavitation treatment schemes on diagnostic probes would lead to further translation of this technique by using existing hardware already found clinically, and use a single system for both therapy and imaging and thus converting the clinical scanner to a theranostic device.

Furthermore, ultrasound images may be quantified and provide perfusion metrics for tumors and organs. Currently, quantitative contrast-enhanced ultrasound (CEUS) perfusion evaluations of bolus injections are typically performed with time-intensity curve (TIC) analysis [21–23]. This data is often fitted to an indicator dilution model [24] to remove noise, and metrics related to blood flow and volume are extracted. However, TIC analysis averages intensity of all pixels within a region of interest (ROI), and it struggles to differentiate between reduction in intensity and the spatial distribution of signal within the ROI. In addition, intensity-based TIC metrics have demonstrated a high degree of variability even in repeated injections [25,26], furthering this issue. Quantitative CEUS studies assessing blood flow changes to cavitation treatments have suggested that perfused area evaluated at the peak of the bolus have been reported to be more sensitive as compared to standard bolus parameters [27,28]. However, irregular tumor vasculature can exhibit high variability in blood flow in different regions of the tumor [29,30], and cavitation treatments have been shown to nonuniformly influence flow rates within the tumor [8] suggesting that evaluating tumor perfusion loss from cavitation treatments at a single point in time may not contain comprehensive information of the tumor blood volume. Super-resolution techniques have been implemented to more accurately evaluate tumor perfusion changes [31], but clinical translational of these techniques is limited due to the influence of respiratory motion and the low volume rates available on clinical systems. Therefore, there is a need for a quantitative technique to evaluate the spatial extent and modulation of tumor blood flow driven by these cavitation treatments utilizing standard clinical imaging techniques.

In this study, we evaluated how targeted ultrasound cavitation treatments performed with a clinical scanner and clinically approved microbubbles could be utilized to assist in the treatment of tumors. We aimed to develop a neoadjuvant therapy that could be used to target and improve therapeutic outcomes in detectable lesions in the early-to-immediate stages of the disease. We hypothesize that inertial cavitation (produced with microbubbles and long ultrasound pulses) induces changes to the tumor microenvironment and specifically to tumor blood perfusion, interstitial fluid pressure (IFP), and drug delivery. We evaluated those changes in a murine tumor model with an acute study. The implementation of the ultrasound conditions on a clinical scanner and real-time imaging of the process are novel elements that could lead to easier clinical translation. Additionally, we developed a novel quantification technique titled maximum intensity projection time-area curve analysis (MIP-TAC) for accurate tumor perfusion evaluations after cavitation treatments, that could also be utilized in future treatment monitoring studies. Our objective in this work is to assist in creating an image-guided, simple, and highly translatable theranostic technique for the treatment of human liver cancer.

## 4.2 MATERIALS AND METHODS

### 4.2.1 *Tumor cell line and mouse model preparation*

All animal protocols performed were approved by the Institutional Animal Care and Use Committee (IACUC) at the University of Washington, Seattle. This study used a human hepatocellular carcinoma line (HCC), specially HEPG2 (American Type Culture Collection, HB-8065), as a means of relating this work to previous and projected studies evaluating HCCs. Cells were cultured at 37 ◦C at 5% CO2, in Eagle's Minimum Essential Medium supplemented with 10% fetal bovine serum and 1% antibiotic/antimycotic.

In eight- to twelve-week-old athymic nude mice (Charles River Laboratories, Wilmington, MA), 2*106 HEPG2 cells suspended in 50 μL of phosphate buffered saline mixed with 50 μL of Matrigel were implanted in the hind flank with a 23G needle. Tumors were measured twice a week with a GE LogicBook XP (General Electric HealthCare, Chicago, IL, USA) which is a portable ultrasound scanner, and animals were recruited to the study once the maximum tumor diameter

was between 8 and 10 mm, or an approximate tumor volume of 80 mm3 from an ellipsoidal estimation. Representative tumor B-mode images and mouse tumor volume and weight by condition are shown in **Fig. 4.1**.

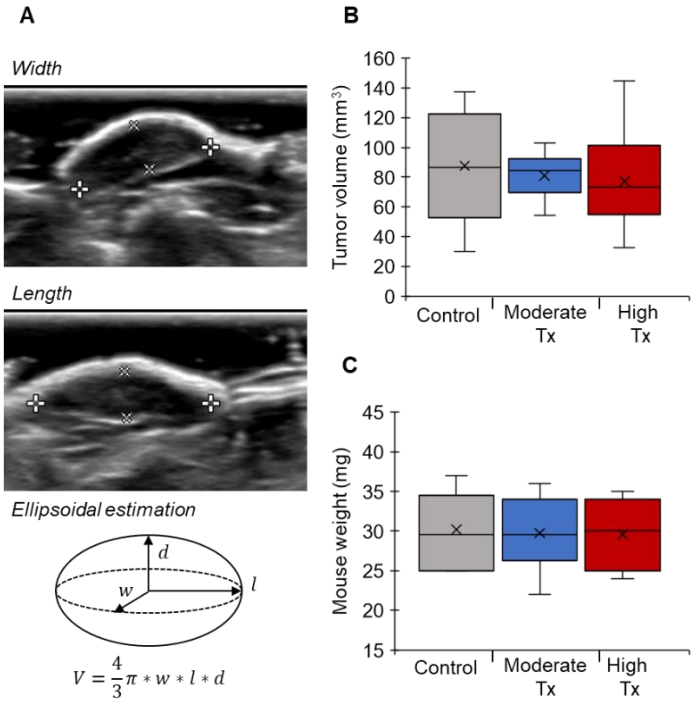


**Figure 4.1**: Tumor sizing across groups. (A) Example B-mode tumor images used for tumor sizing and recruitment, and ellipsoidal estimation utilized. (B) Box and whisker plots of recruited tumor volumes by condition. The "x" represents the mean value. (C) Box and whisker plots of recruited mouse weight by condition. The "x" represents the mean value.

### 4.2.2 *Drug and contrast agents*

Doxorubicin (doxorubicin hydrochloride) was utilized as the chemotherapeutic drug in this study primarily for its fluorescent nature. Dox was purchased (TCI America, Tokyo, Japan) and constituted in sterile saline at a concentration of 10 mg/mL, and mice received dosing at 30 mg/kg [7,16,32]. This high dose was established in previous works to ensure ample measurement sensitivity and the cardiotoxic risk of doxorubicin was not relevant due to the acute timeline employed here.

Lumason microbubbles (Bracco Suisse SA, Geneva, Switzerland), called SonoVue outside the United States, were utilized as the theranostic agent in this study due to its clinical approval for the characterization of focal liver lesions in the United States and in several countries across

Europe and Asia [33]. Microbubble dosing of 50 μL per injection was determined based upon previous work [7,34] to provide adequate signal without inducing acoustic shadowing, and this dosing scheme was employed for all microbubble injections. Repeated bolus injections were selected over infusion in order to eliminate the added complexity of infusions, navigate the small volumes allowed in small animals, and provide the most concentrated bubble delivery.

### 4.2.3 *Ultrasound parameters*

Acoustic conditions suitable for cavitation treatments were implemented on a Philips EPIQ scanner and S5–1 phased array (Philips Healthcare, Bothell, WA, USA). The treatment conditions in this work are a modified version of the scanner settings previously described [17]. Briefly, we modified the standard B-mode setting where instead of forming a sector scan with multiple lines, the center line is repeatedly transmitted at a specified pulse repetition frequency (PRF). Pulses were programmed with a frequency of 1.67 MHz (the lowest frequency that the S5–1 array could efficiently transmit), and duration of 1000 cycles. Peak negative pressures in the range of 0.3–2.5 MPa could be selected with the output knob. Two cavitation treatments were explored in this study: "moderate" (1.6 MPa peak negative pressure) and "high" (2.2 MPa peak negative pressure). The frequency and acoustic pressures selected are consistent with prior work investigating ultrasound and microbubble cavitation treatments in vivo [6,7,9,13,14,35–38]. To maximize inertial cavitation dose, we chose the highest possible PRF for those two acoustic pressures that were possible to implement on the specific scanner and while considering its hardware limitations (200 Hz PRF for the "moderate" and 10 Hz PRF for the "high"). A deep azimuthal focus (z = 13 cm) was selected to create a large focal region 65 mm from the probe, such that a majority of the tumor received the same acoustic pressure. High acoustic pressures, greatest number of cycles, and shortest pulse repetition times were employed in this study to maximize inertial cavitation dose based on its relationship with drug extravasation distance [14] and to explore cavitation-induced mechanical changes such as reduction of tumor IFP, which have primarily been observed at acoustic pressures at or above 1 MPa [39,40]. Bioheat simulations estimated only a 0.35°C and 0.07°C temperature rise in the moderate and high cavitation treatment conditions, respectively, suggesting the absence of any thermal effects of these treatments.

Simulated acoustic fields for the azimuthal and elevation planes of the S5–1 with a representative tumor are shown in **Fig. 4.2**. The field simulations are based on the angular spectrum method of the Fresnel diffraction approximation with 2D Fast Fourier Transforms.

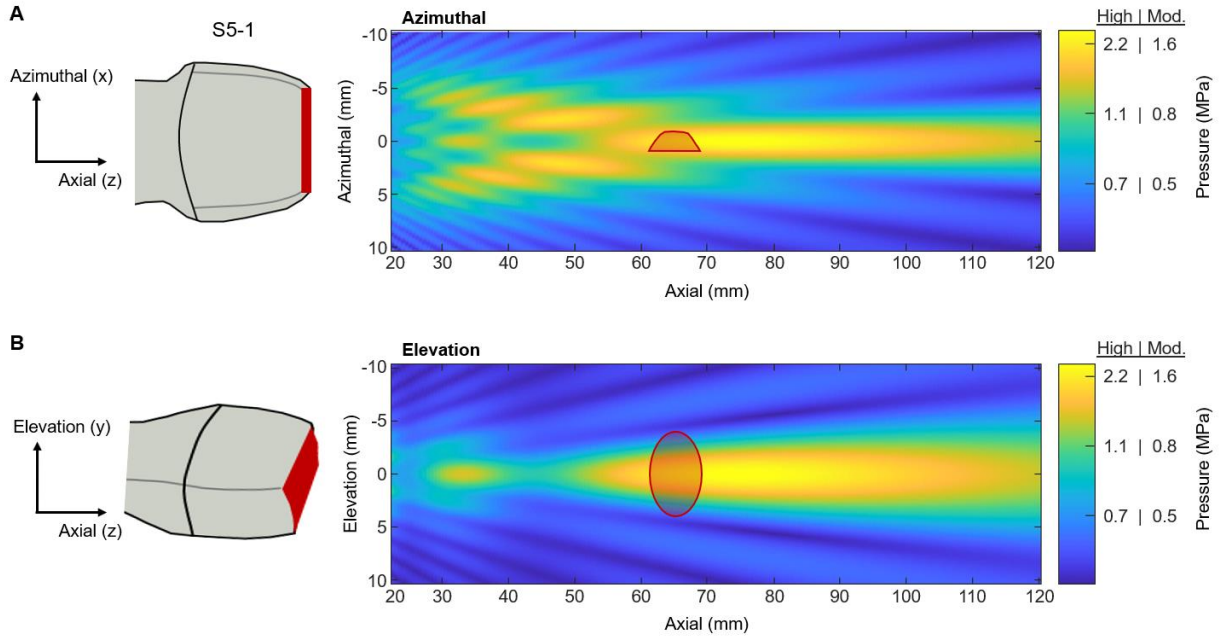


**Figure 4.2**: Simulations for treatment beamforming from the S5–1 phased array. (A) The 2-D azimuthal beam field with a representative 8 mm diameter tumor at 65 mm from the probe. Theoretical peak negative pressures for the high and moderate cavitation treatment condition are listed. (B) The 2-D elevation beam field with a representative 8 mm diameter tumor at 65 mm from the probe. Theoretical peak negative pressures for the high and moderate cavitation treatment condition are listed.

### 4.2.4 *Experimental setup and treatment procedure*

Two Philips ultrasound probes were employed in this study: one for cavitation treatment (EPIQ, S5–1) and one for small animal imaging (iU22, L12–5). A 5 MHz single element transducer (C308, Evident Scientific, Waltham, MA) was also used to perform passive cavitation detection (PCD) and evaluate cavitation in vivo. To account for the treatment beamforming and alignment of several probes to the tumor, a heated (37 ◦C) and degassed water tank setup was utilized (**Fig. 4.3**). Prior to experiments, the 2 probes and PCD transducer were co-aligned to the same 3-D position using a thin vertical wire target. First, the PCD transducer was aligned 5.1 cm (geometric focus) from the wire using a pulse-echo technique. The PCD transducer was then used as a receiver to align the S5–1 and L12–5 probes 6.5 and 2 cm from the wire, respectively, and to the same vertical

position as the PCD transducer. The position of the wire on the L12–5 image was recorded, after which the wire target was removed from the water tank. Mice were then anesthetized under 1.5–2% isoflurane and prepared with a 30G needle tail vein catheter. The mice were secured to a custom restraining board before being partially submerged in the water tank and positioned such that the center of the tumor coincided with the wire position on the L12–5 image.

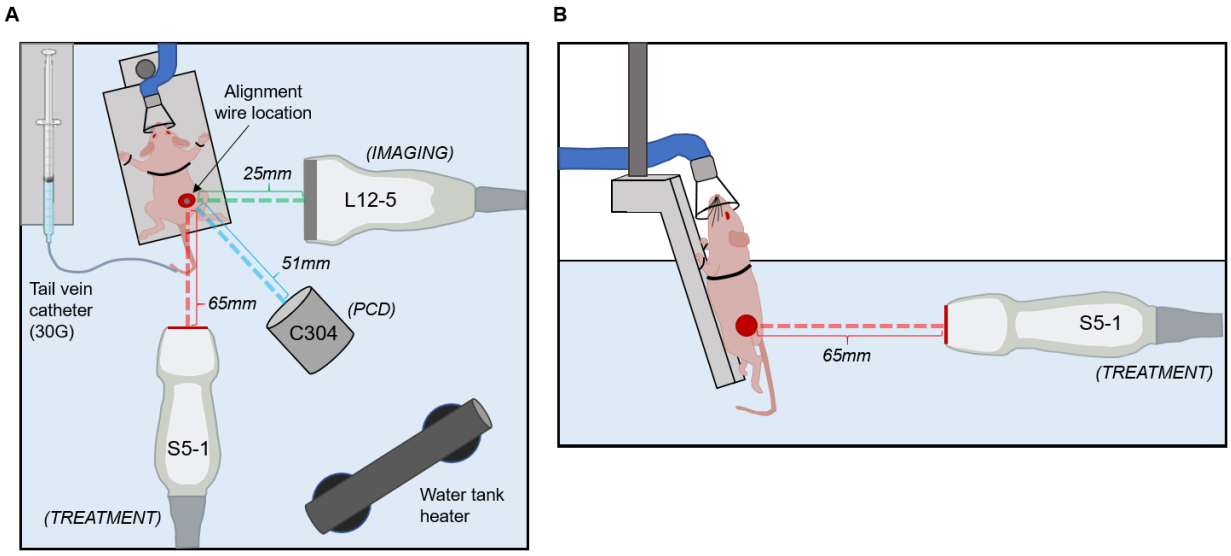


**Figure 4.3**: Schematic of heated water tank experimental setup. (A) A top-down view, illustrating the co-alignment of the treatment, imaging, and passive cavitation detecting probes. The red dot represents the subcutaneous tumor on the mouse. A black dot within the tumor indicates the location of the wire used to align the probes before the mouse was place with the center of the tumor in the same location. (B) A side view of the setup, illustrating the partial submersion of the mouse, and the alignment of the probe to the exact depth of the tumor.

Five groups of 8 mice (4 male, 4 female, total n = 40) were randomly divided into one of the following conditions: control (dox only), moderate cavitation, high cavitation, moderate cavitation + dox, and high cavitation + dox. An overview of the experimental timeline is shown in **Fig. 4.4**. A 50 µL bolus of microbubbles was delivered before cavitation treatments while the tumor was continuously scanned with CEUS (amplitude modulation, 4.1 MHz, 4 cycles, mechanical index = 0.06) to establish baseline tumor vascularity, titled "pre-treatment". A time-intensity curve was formed from a freeform polygon region of interest (ROI) of the tumor to determine when peak microbubble concentration within it had occurred, as illustrated in **Fig. 4.5**. Treatments were performed for a total of 30 s at the determined peak of the bolus, in alternating 5 s "on" and "off"

periods, and these treatments were repeated 4 times for each tumor. The rationale for the 5 s "on" duration is to ensure all microbubbles within the tumor are insonified long enough and destroyed. Complete microbubble destruction potentially occurs within 100 milliseconds but we selected 5 s to be overly conservative. The rationale for the 5 s "off" period is to allow time for surrounding circulating microbubbles to re-perfuse the tumor and be insonified based on our prior knowledge of the rise time of TICs from murine tumors being approximately 5 s. Mice in conditions with dox received the 30 mg/kg dose co-delivered with microbubbles evenly divided across the 4 treatment injections, delivered immediately after one another, approximately two minutes apart. A 50 µL bolus of microbubbles was also delivered after the cavitation treatments while CEUS was performed to evaluate the immediate tumor blood flow changes resulting from the treatment, titled "post-treatment". For a subset of mice (4 moderate, 4 high, total n = 8), PCD measurements were recorded using an oscilloscope (DPO 7054C Tektronix, Beaverton, OR, USA) with a segmented memory technique ("Fast Frame"). An external trigger from the EPIQ scanner triggered the oscilloscope to capture the scattered sound from all pulses within the first second of each treatment, sampled at 100 MS/ s. Before injecting microbubbles, PCD was recorded in each animal to establish a baseline signal.

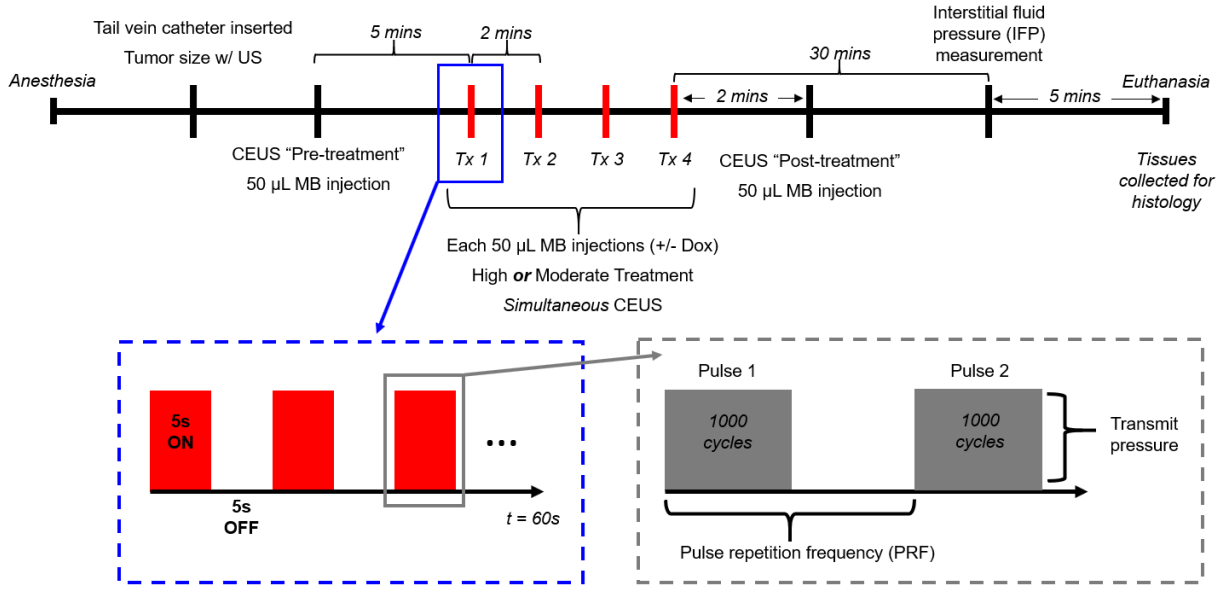


**Figure 4.4**: Experimental protocol overview. MB = microbubble, US = ultrasound, CEUS = contrast-enhanced ultrasound.

After removal from the water tank and 30 min after the last treatment, tumor interstitial fluid pressure measurements were made. A pressure catheter (SPR-671, ADInstruments Inc., Colorado Springs, CO, USA) was threaded through a thin-walled 19G needle and soaked in deionized water for 30 min before calibrating the baseline zero to be equal to atmospheric pressure (sensor held just below water surface). The catheter was then retracted into the needle and inserted into the center of the tumor with the help of ultrasound imaging. The needle was then removed from the tumor and the catheter measured the pressure for 30 s before being removed. Mice were sacrificed by isoflurane overdose and tissue was harvested for histological evaluation and to assess doxorubicin uptake into the tumor. The tumor was excised and cut into halves, where one half of the tumor was embedded into a block of optimal cutting temperature (OCT) compound and flash frozen to -80°C with cooled isopentane, and the other half was placed in a sealed tube. All tissue was stored at -80°C until analysis.

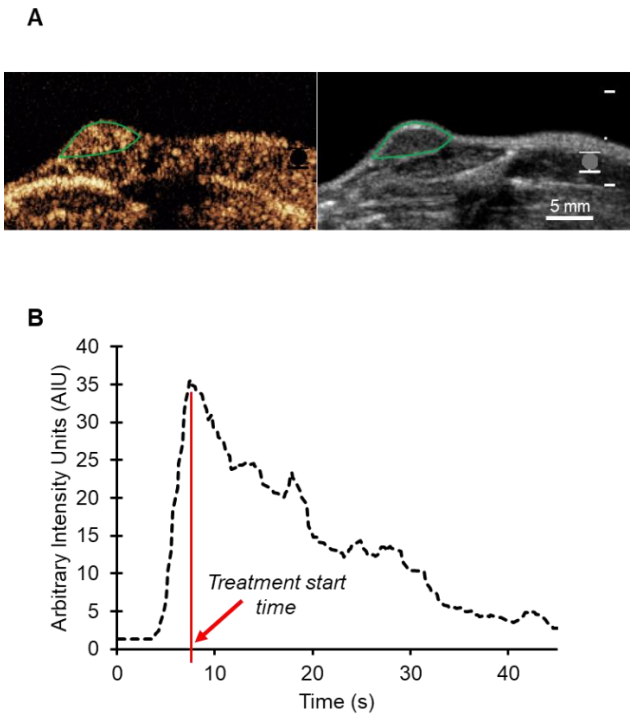


**Figure 4.5**: An example contrast-ultrasound side-side image of a tumor (A) and the resulting time-intensity curve (B) performed to determine treatment timing.

### 4.2.5 *CEUS quantification – Maximum intensity projection time-area curve analysis*

To quantitatively determine changes in transient perfusion loss within the tumor resulting from the cavitation treatment, a novel perfusion quantification algorithm was developed to evaluate the perfused area of tumors. Pre- and post-treatment CEUS loops were extracted from the ultrasound scanner, processed with Philips QLAB's super-resolution technique which performs maximum intensity projection (MIP) in combination with advanced motion compensation techniques and proprietary image processing that leads to higher spatial resolution [41,42]. A MIP loop consists of images where the brightest intensity is permanently persisted. The MIP loop was next analyzed with a MATLAB algorithm to produce a time-area curve (TAC) which displays the area of the tumor that received any microbubble signal as a function of time, and hence we will refer to this technique as MIP-TAC. A MIP-TAC displays the normalized perfused area as a function of time. The normalized perfused area is a value between 0 and 1, where 0 means that the tumor has no perfusion/blood flow and 1 means the tumor is fully perfused. The normalized perfused area is calculated by counting all pixels within the tumor ROI with signal above baseline noise, established by the average non-zero signal within the tumor ROI prior to contrast arrival, divided by the total number of pixels in the tumor. **Figure 4.6** provides CEUS and MIP images alongside the resulting TAC and MIP-TAC for the same tumor to assist with comprehension of this processing method. A sample MIP-TAC before and after treatment is shown in **Fig. 4.7**. From these MIP-TACs we then calculate the normalized perfusion loss as the difference between pre-treatment and posttreatment perfused area 15 s after contrast arrival (see green arrow in **Fig. 4.7**). The 15 s timepoint was selected as it is the approximate one-pass circulation time of blood in a mouse [43] to mitigate potential confounding of these metrics from differences in recirculating bubbles across mice, and to minimize smearing of contrast signal from maximum intensity projection over time due to respiratory motion. One mouse in both the moderate and high cavitation conditions was omitted from MIP-TAC analysis due to differences in imaging settings (digital gain and dynamic range).

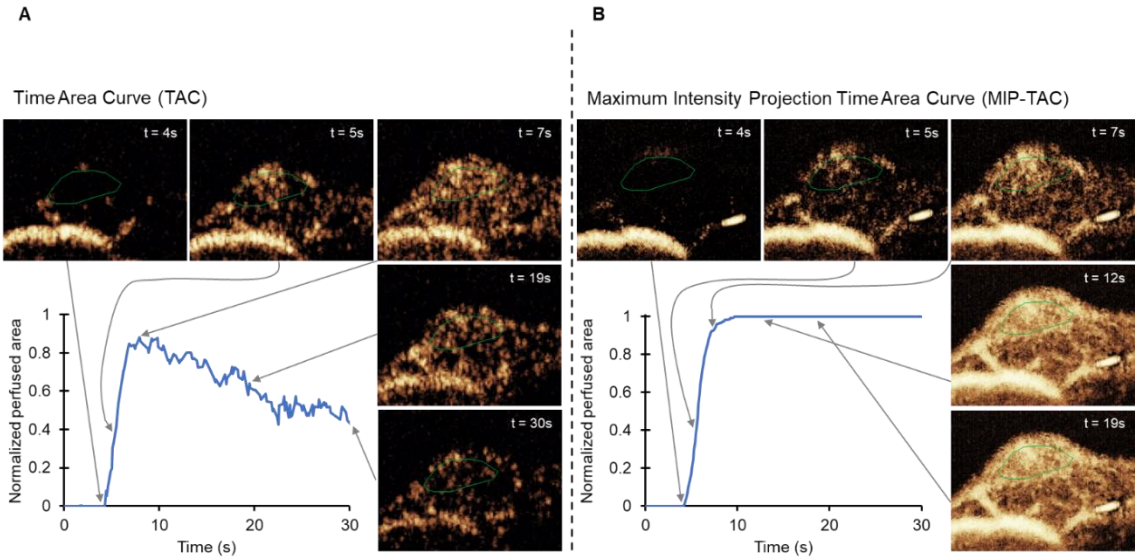


**Figure 4.6**: A visual aid for describing maximum intensity projection (MIP) time area curve (TAC) generation. (A) Contrast-enhanced ultrasound images (CEUS) at various times and the resulting TAC. (B) MIP images for the same tumor and resulting MIP-TAC.

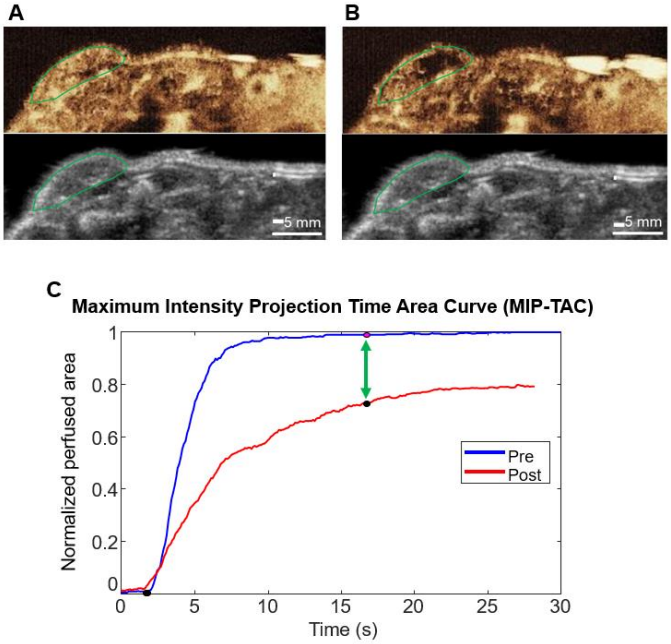


**Figure 4.7**: A representative example from the moderate condition illustrating maximum intensity projection time-area curve analysis (MIP-TAC). B-mode and MIP images before treatment (A) and after treatment (B) are shown. The tumor is outlined with a green line. (C) Normalized perfused area before (blue) and after (red) treatment. A value of 1 means the tumor is fully perfused and a value of 0 means that the tumor has no perfusion. The green arrow indicates the value of normalized perfusion 15 s after contrast arrival which is used to calculate the tumor perfusion loss metric.

### 4.2.6 *Passive cavitation analysis*

A custom MATLAB script was used to calculate the broadband energy of received scattered signals during cavitation treatments according to the method previously described [17]. Briefly, each waveform was first truncated to its pulse length (1000 cycles), the average magnitude of the waveform was removed, and then multiplied by a Blackman-Harris window. The one-sided power spectrum was then calculated, and broadband energy was collected above the third harmonic (to limit influence of the transmitted pulse) in the frequency range of 5–10 MHz (roughly the upper limit of the receiver bandwidth). Within this range, frequency bands centered on each harmonic and ultraharmonic with a bandwidth of 0.3 MHz were excluded while remaining bands were summed, resulting in the broadband energy per pulse.

### 4.2.7 *Histology and doxorubicin evaluations*

The frozen tissue in OCT blocks were sectioned at 5 μm with a cryostat (Leica CM1950, Leica Biosystems, Nussloch, Germany) and slides were imaged and stained on the same day. We used a custom filter cube with excitation = 470 nm, emission = 590 nm to assess doxorubicin distribution in the tumor using a fluorescence microscope (Nikon Eclipse Ti, Nikon Instruments, Tokyo, Japan) and microscope camera (Hamamatsu ORCA-Flash4.0 LT C11440-42 U, Hamamatsu Photonics, Shizuoka, Japan). All imaging was performed at the same settings (lamp brightness, exposure time, LUT, etc.). The images were qualitatively assessed, searching for an even distribution of fluorescence within cell nuclei throughout the tumor to indicate successful drug penetration. Sequential sections were stained with hematoxylin and eosin (H&E) and assessed for gross mechanical tissue damage using bright field microscopy (Nikon Eclipse 80i, Nikon Instruments, Tokyo, Japan). Three sections from each tumor were used for qualitative doxorubicin and H&E evaluations.

Doxorubicin uptake into the tumor and other harvested tissues was quantified as described previously [7,32]. Frozen tissue first was homogenized in RIPA buffer at 2% w/v concentration, then 200 μL of the homogenate was combined with 100 μL 10% v/v Triton X-100, 200 μL dH2O, and 1500 μL 0.75 N acidified isopropanol. The resulting 2 mL solution was centrifuged at 15,000g

for 20 min and stored at -80°C until analysis. Supernatant samples were loaded onto a 96-well plate for quantification and run alongside a calibration curve (7 known concentrations between 0 and 2.5 μg doxorubicin per mL, inclusive, added to untreated, processed tumor tissue) using a plate reader (Synergy Neo, BioTek Instruments Inc.) at excitation = 470 nm, emission = 590 nm. All samples were run on the same day and in duplicate. The magnitude of fluorescence was calibrated to the known curve to obtain the corresponding to doxorubicin concentration in each sample. To account for variations in tumor size between mice, doxorubicin fluorescent levels were normalized to tumor weights.

### 4.2.8 *Statistical analysis*

A two-sided Welch's t-test was used to evaluate statistical differences between the resulting tumor perfusion loss from the moderate and high cavitation treatment groups. A repeated measures ANOVA was utilized to identify statistically significant differences in tumor perfusion loss during treatment between the moderate and high cavitation groups. A Kruskal-Wallis with Dunn's post-hoc test was used for quantitative doxorubicin and interstitial fluid pressure measurements. For all analyses, the significance levels were set to 0.05.

## 4.3 RESULTS

### 4.3.1 *Quantification of tumor blood flow changes*

**Figure 4.8** depicts transient tumor perfusion loss throughout the treatment regime. In the moderate cavitation treatment (**Fig. 4.8A**), tumor blood flow persisted throughout all four treatments, with a gradual decrease observed in the center of the tumor. For the high cavitation treatment (**Fig. 4.8B**), nearly complete transient tumor perfusion loss was observed after the first cavitation treatment, and persisted in the following three treatments. Transient tumor perfusion loss throughout treatment in the high cavitation + dox and moderate cavitation + dox groups was quantified in **Fig. 4.9**. Normalized perfused area was calculated for each treatment injection at the time of the peak of the bolus. These normalized perfused areas were then subtracted from the pretreatment value, and averaged by group to generate the curves shown in **Fig. 4.9**. Significant reduction of tumor perfusion was observed after the first treatment in the high cavitation condition where the normalized perfused tumor area further decreased with ($p = 0.002$, repeated measures ANOVA).

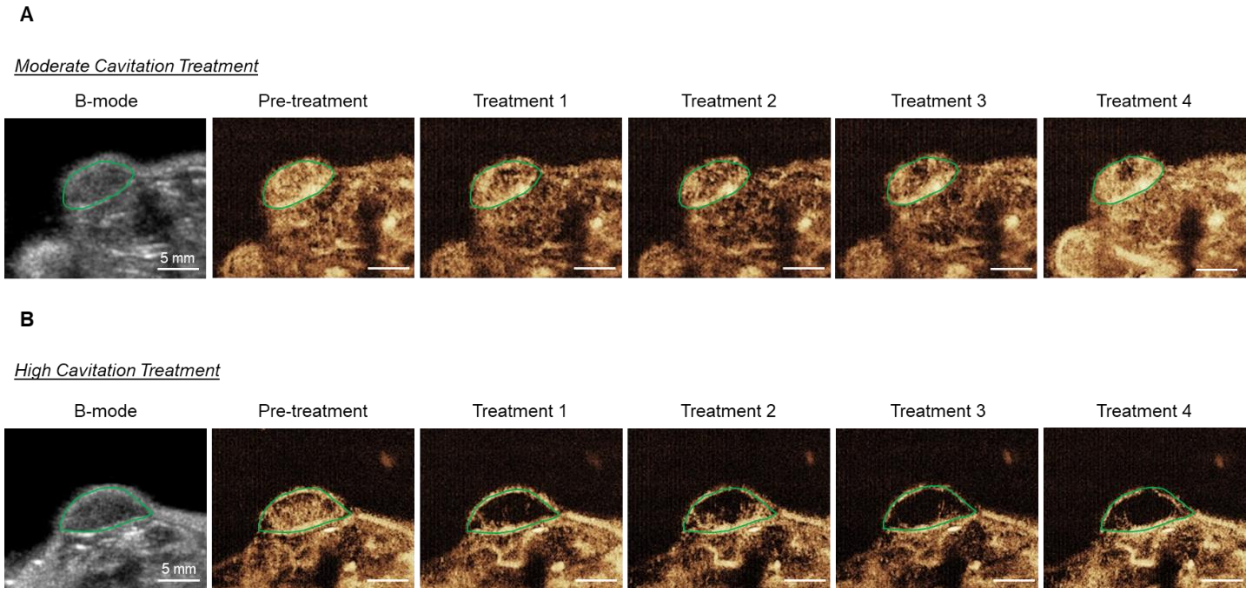


**Figure 4.8**: B-mode and maximum intensity projection (MIP) contrast-enhanced ultrasound (CEUS) images during treatment for the moderate cavitation (A) and high cavitation group (B).

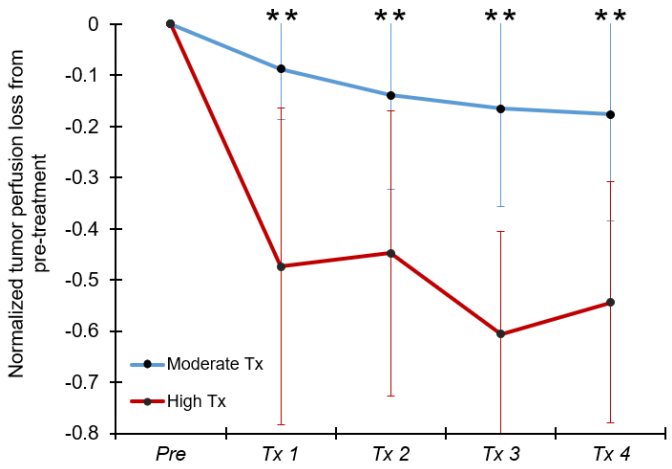


**Figure 4.9**: Normalized tumor perfusion loss across treatment injections. Average and standard deviation values exhibit the significant reduction in tumor blood volume in the high condition as opposed to the moderate condition (2-way repeated measures ANOVA, $p = 0.002$, 95% confidence interval of mean differences: [21.98, 53.71], Cohen's d effect size: 1.71, $n = 7$ per group). $^{**}p < 0.01$.

**Figure 4.10** illustrates the tumor blood flow changes resulting from all four cavitation treatments observed in this study. **Figure 4.10A** shows a representative control, while **Fig. 4.10B and C** show two representative pre- and post-treatment images for the moderate and high cavitation treatments respectively. In the moderate cavitation condition, a minor and heterogenous reduction in blood flow was observed. Meanwhile, a majority of the mice in the high cavitation condition exhibited

significant transient tumor perfusion loss. Normalized tumor perfusion loss demonstrated statistically significant differences ($p < 0.001$, two-sided Welch's t-test) between the cavitation treatments reflecting the qualitative observations (**Fig. 4.11**).

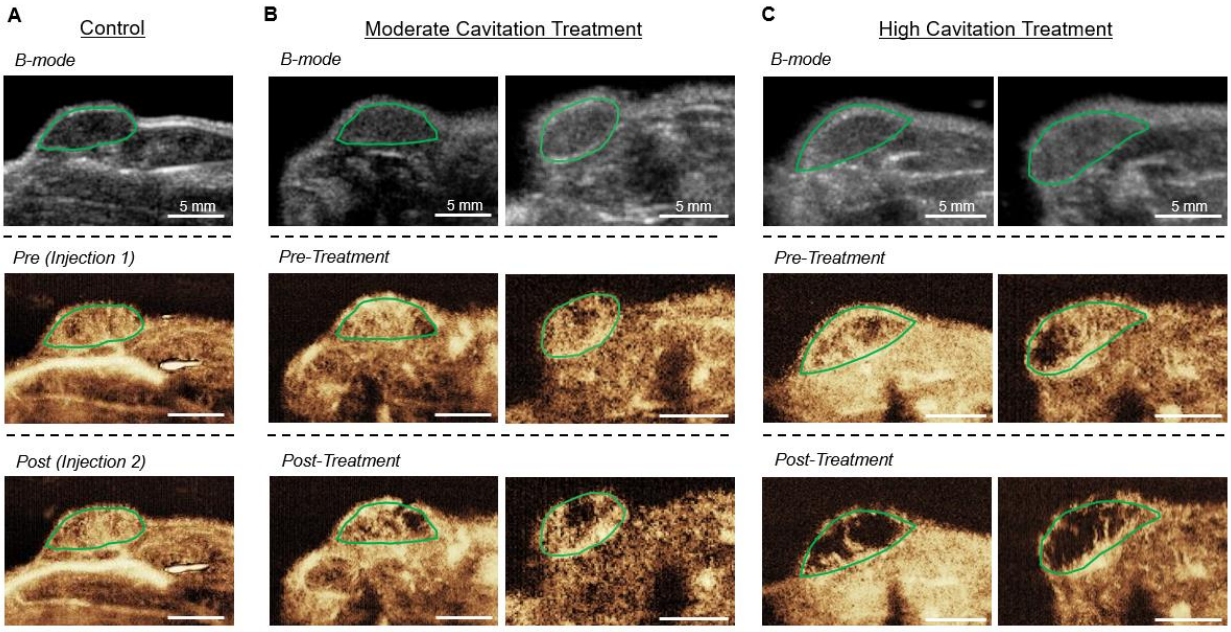


**Figure 4.10**: Examples of transient tumor perfusion loss alongside a representative control (A) in response to all four cavitation treatments with the moderate condition (B), and with the high condition (C). The top row shows the B-mode image, while the others are all MIP images, with the tumor outlined by the green region of interest.

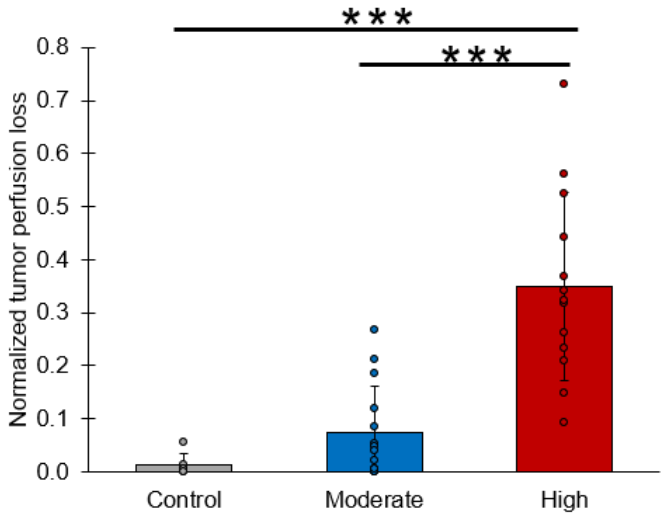


**Figure 4.11**: Normalized tumor perfusion loss in response to cavitation treatments. (A) Average value with standard deviation bars for tumor perfusion loss by treatment condition. The high cavitation treatment experienced a significantly larger degree of perfusion loss than the moderate condition and control (Kruskal-Wallis with Dunn's post-hoc, moderate-high $p < 0.001$, control-high $p < 0.001$, ranked $\varepsilon 2$ effect size: 0.627, $n = 15$ for the moderate and high conditions, $n = 8$ for the control group). *** $p < 0.001$.

### 4.3.2 *Evaluation of cavitation activity*

**Figure 4.12** shows the cavitation activity measured by PCD during treatments. **Figure 4.12A** is an example spectrum of the first transmitted pulse of a high cavitation treatment where harmonics, sub/ultraharmonics and elevated broadband energy are observed. The average ($n = 4$) broadband energy of the first 5 pulses during the high cavitation treatments is shown in **Fig. 4.12B**. Only the first few pulses generated broadband energy significantly greater than the zero level (baseline, no microbubbles), and by the third pulse broadband energy had returned to the zero level. The cavitation activity of the first pulse is further analyzed in **Fig. 4.12C**, which shows the average ($n = 3$) broadband energy of the first pulse of treatments 1 and 4 (see **Fig. 4.4**) for both the moderate and high cavitation conditions. In treatment 1, both moderate and high conditions generated elevated broadband energy above baseline, indicating cavitation treatments produced spectral components consistent with what is often referred to as inertial cavitation as we intended when selecting these conditions. The high cavitation condition produced an average broadband energy level 3.4 times greater than the broadband energy from the moderate condition. By treatment 4 the broadband energy is reduced, with the moderate condition reduced by an average of 1.6 times, and

the high condition reduced by an average of 2.5 times. This is likely due to the reduced number of scatterers in the tumor center (see **Fig. 4.8**), indicating PCD is also sensitive to transient tumor perfusion loss. However, PCD measurements may be sensitive to scattered signal from the tumor periphery, since broadband energy is still elevated in the high cavitation condition despite no microbubbles being present in the tumor center.

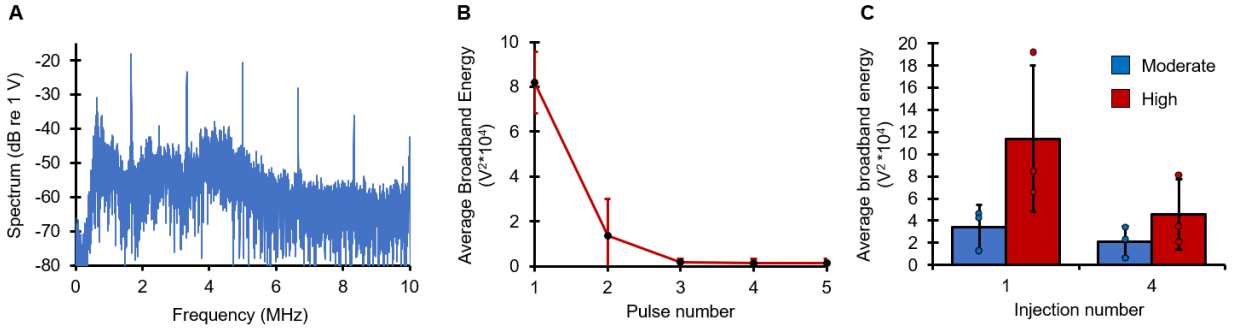


**Figure 4.12**: (A) An example spectrum of microbubble cavitation from passive cavitation detection. (B) Mean and standard deviation of average broadband energy in the first 5 treatment pulses for a subset of mice in the high cavitation treatment condition (n = 4). (C) Mean and standard deviation of average broadband energy for the first treatment pulse of injection 1 and 4 for both cavitation treatment groups (n = 3 per group).

### 4.3.3 *Doxorubicin and histological evaluations*

**Figure 4.13** shows representative qualitative doxorubicin extravasation images from each condition. The left column depicts representative full section dox images, with the middle and right columns highlighting interesting regions in the section. In qualitative observations, samples from the moderate cavitation group more consistently depicted a uniform distribution of red fluorescent dox positive nuclei throughout the tumor, and these samples matched higher relative quantitative values. **Figure 4.14** supplies quantitative dox results from all tumor tissue. Only the moderate cavitation treatment exhibited a significant increase in dox uptake compared to the control ($p = 0.024$, Kruskal-Wallis with Dunn's post-hoc), in agreement with qualitative evaluations. Finally, **Fig. 4.15** shows representative full section and zoomed in H&E images, where no significant ablative damage or hemorrhage was observed.

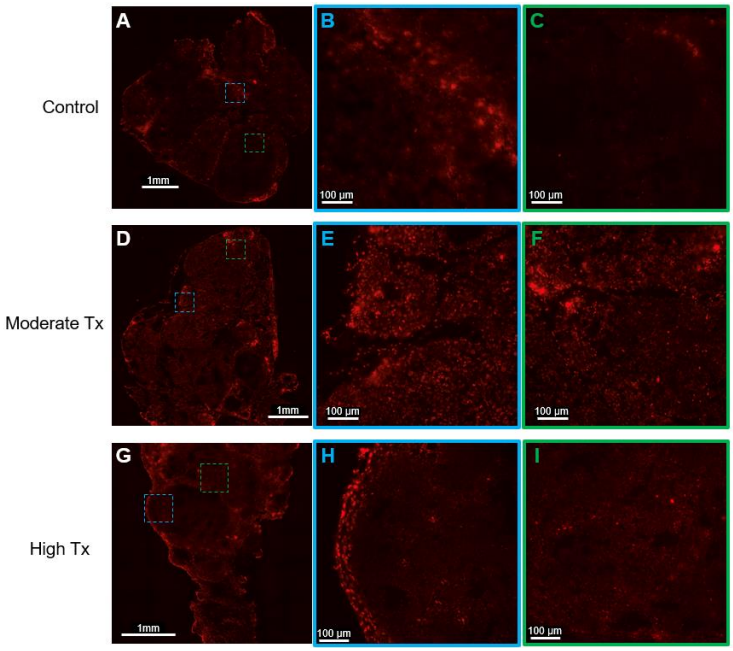


**Figure 4.13**: Representative fluorescent doxorubicin images. (A) A representative full section image and zoomed-in regions of interest (B, C) for the control condition. (D) A representative full section image and zoomed-in regions of interest (E, F) for the moderate cavitation condition. (G) A representative full section image and zoomed-in regions of interest (H, I) for the high cavitation condition.

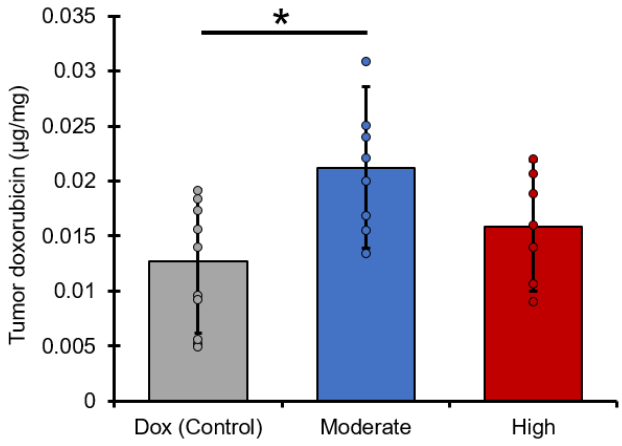


**Figure 4.14**: Quantitative tumor doxorubicin average and standard deviation by treatment condition. The moderate cavitation treatment demonstrated a significant increase of doxorubicin above the control (Kruskal-Wallis with Dunn's post-hoc, control-moderate $p = 0.024$, ranked $\varepsilon 2$ effect size: 0.21, $n = 8$ per group). *$p < 0.05$.

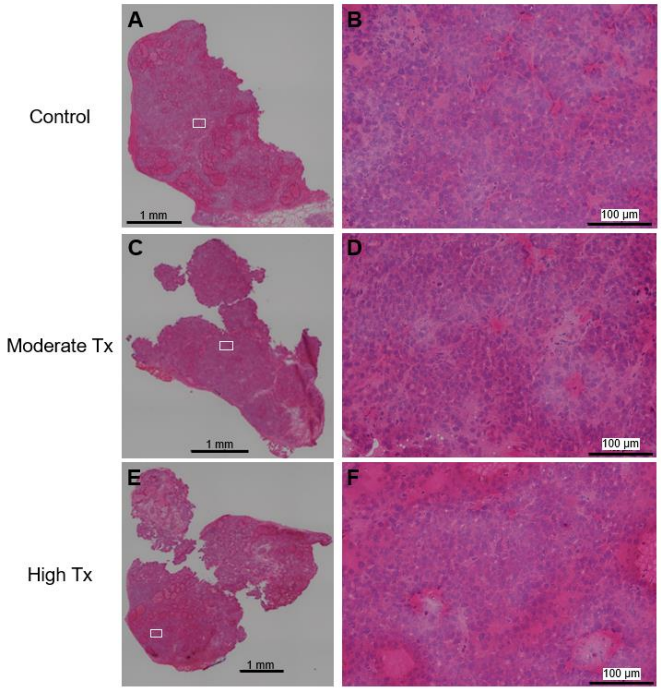


**Figure 4.15**: Representative hematoxylin and eosin (H&E) stained tumor sections. A representative full section image (A, C, E) and zoomed-in region of interest from that section (B, D, F) are shown for the control, moderate, and high cavitation treatment groups respectively. No significant ablative damage or hemorrhage was observed.

### 4.3.4 *Interstitial fluid pressure measurements*

**Figure 4.16** shows average IFP measurements by condition. There was a significant reduction ($p = 0.001$ and $p = 0.015$ for the moderate condition and high condition respectively) in IFP in both ultrasound cavitation conditions relative to the controls, despite all IFPs measured being very low, <10 mmHg. However, despite the vascular and drug differences between the ultrasound treatment conditions, no significant differences in IFP were recorded between the moderate and high conditions.

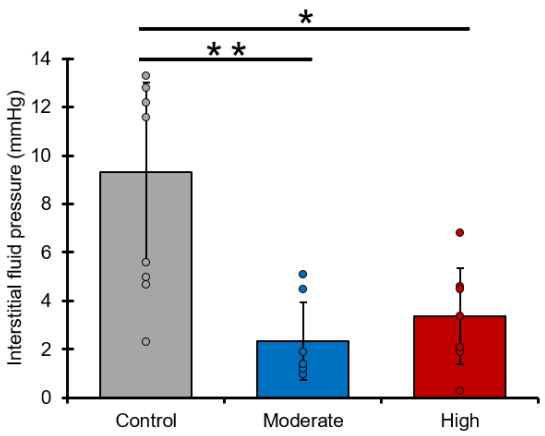


**Figure 4.16**: Average and standard deviation of interstitial fluid pressure measurements by treatment condition. A significant decrease in interstitial fluid pressure was observed in both the moderate ($p = 0.001$) and high ($p = 0.015$) cavitation treatment groups relative to the control group (Kruskal-Wallis with Dunn's post-hoc, ranked $\varepsilon 2$ effect size: 0.57, $n = 7$ per group). *$p < 0.05$, **$p < 0.01$.

## 4.4 Discussion

### 4.4.1 *Modulation of the tumor microenvironment*

In this work, we were able to perform ultrasound cavitation treatments with clinically approved microbubbles and a modified clinical scanner programmed to transmit long pulses (1000 cycles). We confirmed via passive cavitation detection that our programmed long ultrasound pulses produced spectral components consistent with what is often referred to as inertial cavitation. Recent work by Wu et al. has concluded that although the number of harmonics and presence of broadband content in received bubble signal increases with increasing bubble oscillation amplitude, these spectral components alone do not directly distinguish bubble dynamics due to multiple confounding factors such as the characteristics of the sensing element and the frequency of bubble collapse [44]. As a result, use of binary terms to define microbubble activity can potentially be misrepresentative, and as such we specified exactly which spectral components were measured to qualify our use of the term inertial cavitation, and also evaluated treatment through other relevant bioeffects such as transient tumor perfusion loss and drug extravasation. Previous works in this area use custom-built single-element transducers [13,14,35–37,45–51] designed for animal use and lack the regulatory approval for clinical use, and would be challenging to translate for human use. By implementing our treatment pulses on a phased array of a clinical scanner, we

can design dynamic beamforming and steering to account for variability in lesion location and depth in patient populations as opposed to custom transducers with a fixed focus. Two clinical probes were used in this study to allow for simultaneous treatment and imaging due to using a small animal tumor model, where the imaging must be performed at a higher frequency whereas the cavitation treatment must be at lower frequencies. However, both imaging and treatment could be performed at frequencies covered with the same probe in clinical abdominal imaging, thus converting a clinical scanner to a theranostic device. The use of small animals here introduced greater complexity than what would be necessary for human scanning.

### 4.4.2 *Microbubble cavitation-induced transient tumor perfusion loss*

As demonstrated by our results in **Figs. 4.8 and 4.9**, we induced transient tumor perfusion loss with our cavitation treatments. In order to evaluate these changes, we introduced a novel quantification technique for 2D CEUS. Standard time-intensity curve analysis [52–55], which averages brightness across all pixels within a ROI, was not ideal for assessing these transient tumor perfusion loss events where flow is halted to large regions of the tumor. Through the use of MIP-TAC analysis, we were able to capture the spatial and temporal dynamics of tumor perfusion loss resulting from cavitation treatments with bolus injections, compatible with standard clinical practices. Tortuous vessels rapidly formed within tumor which lack mature pericyte involvement exhibit slow velocities and poor perfusion in their center as opposed to the peripheral vessels, alongside an enhancement or reduction of tumor blood flow in response to cavitation treatment, depending on the acoustic conditions utilized [6–8,13,14,56]. Through the use of maximum intensity projection as opposed to perfused area evaluations made only at a specific time of the bolus transit, we were able to incorporate contributions of all these vessels for spatial evaluations. This quantitative technique could directly translate to 3D CEUS data to volumetrically evaluate tumor blood flow as hardware and imaging techniques advance.

Through inclusion of two ultrasound cavitation treatment conditions (2 acoustic pressures), we were able to initially investigate the relationship between transient tumor perfusion loss and the acoustic pressure. Importantly, this study uniquely incorporates real-time CEUS imaging during treatment, allowing for the evaluation of microbubble presence during and between treatments, enabling future optimization of cavitation treatments. We observed how the extent of tumor

perfusion loss scaled with acoustic pressure, as suggested in previous similar works [6,8,14,51], and consistently saw a significant difference between the two groups. We also performed four consecutive cavitation treatments with alternating five second “on” and “off” periods with simultaneous imaging to provide feedback about our treatment regime. The purpose of the five second off periods was to allow for residual microbubbles to recirculate into the tumor, to then cavitate to further treatment efficacy. However, we observed through both CEUS and PCD that very few microbubbles re-entered the tumor after the first five second treatment, and that nearly all the effect of the cavitation treatment occurred during the first sonication period (**Fig. 4.17**). Insonifying the tumor for 60 s with the 5 s on/off scheme was a conservative approach to leverage recirculating microbubbles, but the limited number of residual microbubbles in this small animal model after the first exposure was captured by both PCD and CEUS. However, despite its limited influence in this study, the relevance of recirculating microbubbles would likely be more significant in humans. Based on our readouts from PCD and CEUS, a more optimal treatment protocol could utilize a much shorter “on” period with no repeated firings, such as a single 1 s exposure. Similarly, the four repeated injections intended to each induce the same biological effect and increase drug penetration, compounding upon one another to allow for greater treatment efficacy. However, as depicted in **Figs. 4.8 and 4.9**, the high cavitation treatment caused a nearly complete cessation of flow within the tumor after the first treatment. Meanwhile the moderate cavitation treatment gradually decreased tumor blood flow, particularly in the center of the tumor. These results suggest that repeated sonications with a single bolus injection in a mouse model likely do not provide a significant enhancement of microbubble cavitation-induced bioeffects, and that the efficacy of repeated injections is diminished when significant tumor perfusion loss occurs.

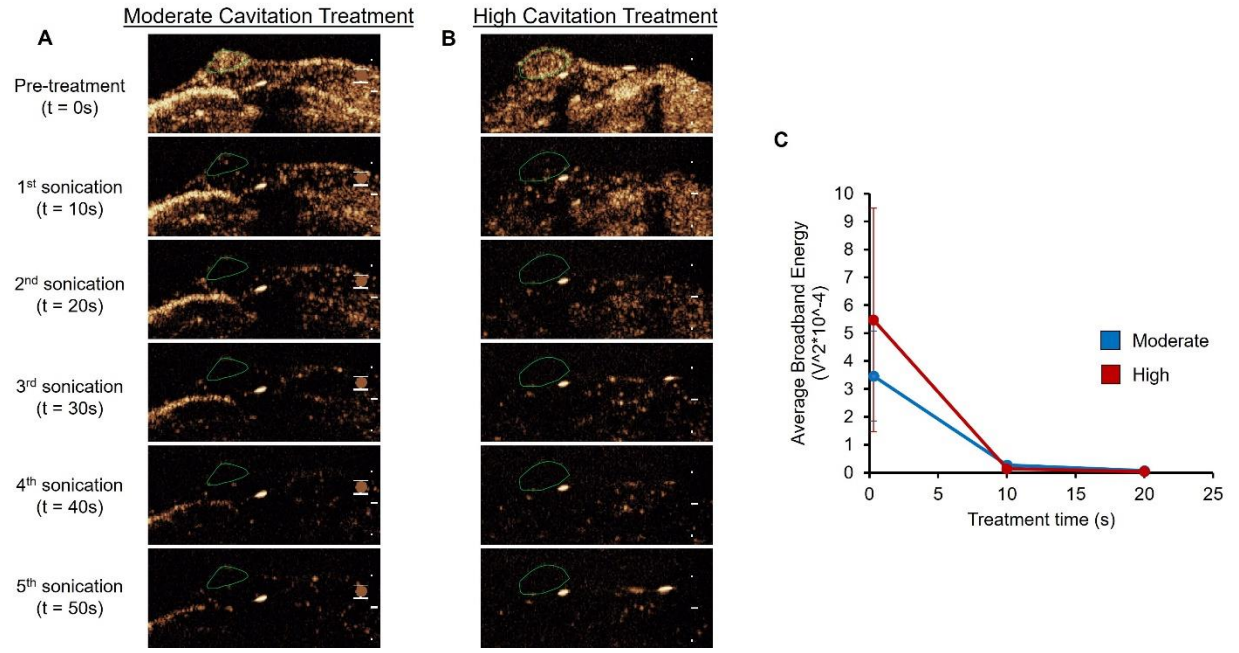


**Figure 4.17**: Contrast-enhanced ultrasound (CEUS) and passive cavitation detection (PCD) during a single cavitation treatment. Representative CEUS images taken immediately before treatments for the moderate condition (A) and high condition (B) throughout the entire minute of treatment. (C) Average broadband energy for the first pulse of the first three "on" periods (corresponding to the first three images in A and B) measured with PCD. Almost no recirculation of microbubbles within the tumor is observed in either cavitation condition, captured by both CEUS and PCD.

However, this study did not evaluate the temporal signature of these tumor perfusion loss events, only looking immediately after treatment occurred. Some studies have observed vascular rebound, or the recovery of tumor blood volume, over a wide range of times (hours to days) [13,14,37,56], but this phenomenon has not been extensively explored in the short term and could be investigated in the future. This study utilized microbubble evaluations of tumor blood volume to quantify cavitation-induced perfusion loss and to capitalize the theranostic capabilities of ultrasound and microbubbles. We note that ultrasound is the only imaging modality with a true blood pool agent ideal for evaluating tumor blood flow changes. However, contrast-free perfusion evaluations such as MRI-based methods employed in assessing blood-brain barrier opening [57–59] could offer complementary information. This information could also be important for understanding how to time treatments to avoid performing them while flow within the tumor is disrupted, if tumor vascularization is necessary.

H&E evaluations showed no signs of significant ablative damage or significant hemorrhage, suggesting that vascular changes induced by cavitation treatments are a reactionary phenomenon and not simply ablative for tumor vessels [8]. Even though other works utilizing similar acoustic parameters determined that their treatments were safe [7,13,36,60], further ex vivo analysis looking directly at vessel integrity and possible cell death would be required to solidly conclude the safety of the specific conditions used here. Previous studies utilizing similar acoustic parameters have also shown that this phenomenon is tumor specific, and hypothesize that the lack of properly matured vessels within tumor make them the most susceptible to cavitation induced mechanical stimuli, resulting in vascular changes [7,8,13]. Our results indicate that these treatments are likely safe and will not induce significant off-target damage, which is particularly relevant in HCCs where sparing the surrounding organ is of high importance.

Transient tumor perfusion loss could be utilized synergistically with other treatment techniques beyond drug extravasation. One such application is thermal ablation where perfusion within a lesion acts a heat-sink effect, and transient tumor perfusion loss could reduce the required treatment time or possibly improve efficacy. Another is with immune-based therapies, where sensitization of the immune system has been initially explored in relation to ultrasound cavitation treatments [35,36,50,61], and could assist in overcoming the immune-silencing properties of these solid tumors. A greater understanding of how transient tumor perfusion loss explored in this study influences tumor progression has yet to be studied, but will be addressed in future work.

### 4.4.3 *Drug penetration with ultrasound cavitation treatments*

In this work, cavitation treatments were also performed with codelivery of doxorubicin, aiming to improve drug penetration and therapeutic efficacy. It is hypothesized that microbubble cavitation within the tumor could act synergistically by mechanically modulating the tumor microenvironment, which typically acts as a barrier to drug delivery. Highly angiogenic tumors like HCC experience enhanced permeability and retention which increases interstitial fluid pressure, generating a pressure gradient that limits drug penetration within the tumor [12]. As demonstrated in Fig. 15, we observed a significant reduction in IFP with both cavitation treatments (albeit these are small pressures), indicating that these conditions are able to mechanically alter the tumor microenvironment and relieve this pressure gradient. We do note the presence of two

possible subgroups that appear in the control group, indicating possible measurement variability from the device sensitivity or differences in baseline tumor IFP across animals, but this would be need to be confirmed with a greater number of samples. The relationship between the reduction in tumor IFP and cavitation treatments is still not well understood and has been attributed to various cavitation-induced bioeffects such as widening of endothelial cell junctions, deformation of collagen fibers, dilation of lymphatic vessels, and the reduction of tumor blood perfusion [62,63]. Despite lacking a comprehensive understanding of this mechanism, cavitation treatments have displayed a relationship with tumor IFP scaling with acoustic pressure [39], and suggest a means for improved therapeutic payload delivery through enhanced vascular permeability and removal of this pressure gradient acting as a barrier to convection [39,64]. Other studies have also attributed similar changes in tumor IFP (5–10 mmHg) to enhanced drug uptake [40].

Conversely to this effect on IFP and its assumed benefit for drug delivery, we observed a significant increase in dox extravasation only in the moderate condition as opposed to both ultrasound treatments. However, this lack of improved drug penetration in the high condition could be explained by the vascular changes we observed and our treatment protocol. As depicted in Figs. 7–8, tumor perfusion was greatly reduced after the first treatment, with very few microbubbles entering the periphery of the tumor on subsequent injections and treatments. Since the doxorubicin dose was split across these four injections, this likely meant that drug delivered in injections two through four was unable to infiltrate the tumor, contributing to its reduced overall uptake. However, there still could be enhanced drug penetration alongside transient tumor perfusion loss in the high condition only on the first event, but could not be confirmed with the dox delivery followed in this study. Meanwhile, by not completely stopping flow after treatments, the moderate condition was able to consistently deliver drug across all four injections. The increased drug delivery observed here demonstrated the potential for microbubble cavitation to enhance drug penetration, while illustrating the induced tumor vascular effects cannot be ignored.

#### 4.4.4 *Limitations*

Despite the advances in cavitation treatments made in this study, there are limitations which should be addressed. Although many components of this study were clinically relevant, treatments were performed in a subcutaneous murine model. This is unlike HCCs, where the tumor

microenvironment is derived from and surrounded by the host organ, particularly impacted by disease. Subcutaneous lesions also lack some of the complex physiological composition that is unique to HCC, and further considerations of targeting, cavitation dynamics, and therapeutic efficacy would need to be addressed prior to clinical translation. Implementation of this technique to human tumors and other complex lesion types, particularly poorly perfused ones, may be limited by low microbubble concentrations. This potential barrier could be mitigated with other tumor sensitizing therapies to improve blood flow employed in similar studies such as mild hyperthermia [65] or nitric oxide therapy [66,67]. In addition, even though ultrasound conditions were consistent with ranges established in existing literature, we were unable to explore a greater parameter space (for example acoustic pressures and numbers of cycles) due to study and system hardware limitations. In particular, based on prior work establishing a linear relationship between inertial cavitation dose and drug penetration and its resulting therapeutic efficacy [14], we utilized the greatest pulse repetition frequency supported by the clinical system in the two ultrasound conditions employed in this study. Acoustic pressure has been described as a primary driver of cavitation-induced bioeffects, particularly tumor vascular changes [9,68]. However, pulse length (number of cycles), frequency and PRF also play a very important role in tumor perfusion changes and drug penetration. These four acoustic parameters - frequency, peak negative pressure, pulse length, and PRF - still require a more extensive investigation to determine their unique contributions to vascular permeability, in vivo microbubble cavitation dynamics, and drug delivery in future optimization studies.

Our repeated treatments confound drug results, and thus remains a question about the relationship between cavitation treatments and the drug penetration. Similarly, we observed different vascular and drug effects by our two conditions, but their contribution to tumor progression was not able to be assessed in this acute study. Although immediate enhancement of drug within the tumor was observed here, the potential influence of sustained perfusion loss resulting from cavitation treatments could possibly impact subsequent treatments performed over weeks. More advanced drug monitoring techniques such as small animal in vivo fluorescence imaging could provide unique quantitative spatial information which could be compared to tumor blood flow changes in longitudinal studies. Similarly, transient or selective tumor perfusion loss could have negative consequences, as cancer cells that remain after other anti-vascular therapies such as vascular

disrupting agents are hypothesized to be more prone to increased vascularization and proliferation, limiting the therapeutic efficacy of the treatment [11,13]. Finally, although the enhanced vascular permeability induced by cavitation treatments is beneficial for drug delivery, the potential increase of metastasis risk would need to be considered and evaluated in subsequent survival studies.

Although we introduced IFP measurements to further understand the mechanical effects of these treatment conditions, the scope of this study was unable to clearly answer the mechanistic question of how cavitation treatments induce tumor perfusion loss. Due to the wide array of microbubble interactions with surrounding tissues in a very small temporal window, the exact mechanism is very challenging to evaluate, but could be explored further in future experiments.

This study, while aiming to be highly translatable, was unable to attend to several considerations that would be need to be addressed prior to clinical translation. Doxorubicin was utilized here for its fluorescent properties, but other small molecule drugs, tyrosine kinase inhibitors, and immune checkpoint inhibitors have demonstrated clinical efficacy in cancer therapy and are beginning to become the standard of care. Although the same cavitation-induced mechanisms which resulted in the increased doxorubicin uptake observed in this work could translate to other drugs [69,70], their direct interactions would need to be studied. In particular, the influence of other drugs on tumor perfusion loss, extravasation distance, and interactions between drugs and microbubble shells could specifically be evaluated. Mechanical alterations to the tumor microenvironment were also the only effect studied here, but thermal changes produced by ultrasound treatments and their possible synergistic nature with tumor drug penetration could be explored further. Finally, although the murine model used in this study is intended to act as an analog to human tumors, the question remains whether transient tumor perfusion loss may be caused in humans with the acoustic conditions used in the present study.

## 4.5 CONCLUSION

Ultrasound cavitation treatments with clinically approved microbubbles were performed using a clinical scanner adapted for theranostic use. Transient tumor perfusion loss was quantified with CEUS and MIPTAC analysis, and doxorubicin extravasation was assessed. While inertial cavitation occurred in both treatment groups (1.6 and 2.2 MPa), the higher acoustic pressure

induced near-complete loss of tumor blood flow, as confirmed by CEUS and PCD, but reduced drug penetration, likely due to the influence of halted tumor perfusion for subsequent injections of the drug. The moderate cavitation treatment, experiencing a lesser degree of transient tumor perfusion loss across injections, produced greater drug extravasation. These findings suggest that optimizing cavitation intensity may balance tumor blood flow changes with drug delivery, and ongoing studies will examine the temporal characteristics of transient tumor perfusion loss and its synergy with standard chemotherapeutics to improve survival.

## 4.6 REFERENCES


[1] E. Kinsey, H.M. Lee, Management of Hepatocellular Carcinoma in 2024: The Multidisciplinary Paradigm in an Evolving Treatment Landscape, Cancers, 16 (2024).
[2] J. He, Z. Liu, X. Zhu, H. Xia, H. Gao, J. Lu, Ultrasonic Microbubble Cavitation Enhanced Tissue Permeability and Drug Diffusion in Solid Tumor Therapy, Pharmaceutics, 14 (2022).
[3] K. Kooiman, S. Roovers, S.A.G. Langeveld, R.T. Kleven, H. Dewitte, M.A. O'Reilly, J.M. Escoffre, A. Bouakaz, M.D. Verweij, K. Hynynen, I. Lentacker, E. Stride, C.K. Holland, Ultrasound-Responsive Cavitation Nuclei for Therapy and Drug Delivery, Ultrasound in medicine & biology, 46 (2020) 1296-1325.
[4] S. Liu, Y. Zhang, Y. Liu, W. Wang, S. Gao, W. Yuan, Z. Sun, L. Liu, C. Wang, Ultrasound-targeted microbubble destruction remodels tumour microenvironment to improve immunotherapeutic effect, British journal of cancer, 128 (2023) 715-725.
[5] D. Sharma, G.J. Czarnota, Using ultrasound and microbubble to enhance the effects of conventional cancer therapies in clinical settings, Cancer metastasis reviews, 44 (2025) 39.
[6] X. Hu, A. Kheirolomoom, L.M. Mahakian, J.R. Beegle, D.E. Kruse, K.S. Lam, K.W. Ferrara, Insonation of targeted microbubbles produces regions of reduced blood flow within tumor vasculature, Investigative radiology, 47 (2012) 398-405.
[7] S.B. Keller, D. Suo, Y.N. Wang, H. Kenerson, R.S. Yeung, M.A. Averkiou, Image-Guided Treatment of Primary Liver Cancer in Mice Leads to Vascular Disruption and Increased Drug Penetration, Frontiers in pharmacology, 11 (2020) 584344.
[8] X. Zhao, C. Pellow, D.E. Goertz, Intravital imaging and cavitation monitoring of antivascular ultrasound in tumor microvasculature, Theranostics, 13 (2023) 250-266.
[9] J. Wang, Z. Zhao, S. Shen, C. Zhang, S. Guo, Y. Lu, Y. Chen, W. Liao, Y. Liao, J. Bin, Selective depletion of tumor neovasculature by microbubble destruction with appropriate ultrasound pressure, International journal of cancer, 137 (2015) 2478-2491.
[10] R.K. Jain, Normalization of tumor vasculature: an emerging concept in antiangiogenic therapy, Science (New York, N.Y.), 307 (2005) 58-62.
[11] K. Liu, X. Zhang, W. Xu, J. Chen, J. Yu, J.R. Gamble, G.W. McCaughan, Targeting the vasculature in hepatocellular carcinoma treatment: Starving versus normalizing blood supply, Clinical and translational gastroenterology, 8 (2017) e98.
[12] D. Semela, J.F. Dufour, Angiogenesis and hepatocellular carcinoma, Journal of hepatology, 41 (2004) 864-880.
[13] D.E. Goertz, M. Todorova, O. Mortazavi, V. Agache, B. Chen, R. Karshafian, K. Hynynen, Antitumor effects of combining docetaxel (taxotere) with the antivascular action of ultrasound stimulated microbubbles, PloS one, 7 (2012) e52307.
[14] Y.-J. Ho, T.-C. Wang, C.-H. Fan, C.-K. Yeh, Spatially Uniform Tumor Treatment and Drug Penetration by Regulating Ultrasound with Microbubbles, ACS Applied Materials & Interfaces, 10 (2018) 17784-17791.
[15] W. Tzu-Yin, K.E. Wilson, S. Machtaler, J.K. Willmann, Ultrasound and microbubble guided drug delivery: mechanistic understanding and clinical implications, Current pharmaceutical biotechnology, 14 (2013) 743-752.
[16] T. Li, Y.N. Wang, T.D. Khokhlova, S. D'Andrea, F. Starr, H. Chen, J.S. McCune, L.J. Risler, A. Mashadi-Hossein, S.R. Hingorani, A. Chang, J.H. Hwang, Pulsed High-Intensity Focused Ultrasound Enhances Delivery of Doxorubicin in a Preclinical Model of Pancreatic Cancer, Cancer research, 75 (2015) 3738-3746.

[17] L.H. De Koninck, K.S. Vuong, S. Shin, J.E. Powers, M.A. Averkiou, Delivery of Cavitation Therapy With a Modified Clinical Scanner: In Vitro Evaluation, IEEE transactions on ultrasonics, ferroelectrics, and frequency control, 72 (2025) 351-361.
[18] G. Dimcevski, S. Kotopoulis, T. Bjånes, D. Hoem, J. Schjøtt, B.T. Gjertsen, M. Biermann, A. Molven, H. Sorbye, E. McCormack, M. Postema, O.H. Gilja, A human clinical trial using ultrasound and microbubbles to enhance gemcitabine treatment of inoperable pancreatic cancer, Journal of controlled release : official journal of the Controlled Release Society, 243 (2016) 172-181.
[19] M. Haram, R. Hansen, D. Bouget, O.F. Myhre, C.L. Davies, E. Hofsli, Treatment of Liver Metastases With Focused Ultrasound and Microbubbles in Patients With Colorectal Cancer Receiving Chemotherapy, Ultrasound in medicine & biology, 49 (2023) 2081-2088.
[20] O.R. Mason, B.P. Davidson, P. Sheeran, M. Muller, J.M. Hodovan, J. Sutton, J. Powers, J.R. Lindner, Augmentation of Tissue Perfusion in Patients With Peripheral Artery Disease Using Microbubble Cavitation, JACC. Cardiovascular imaging, 13 (2020) 641-651.
[21] A. Akhbardeh, H. Sagreiya, A. El Kaffas, J.K. Willmann, D.L. Rubin, A multi-model framework to estimate perfusion parameters using contrast-enhanced ultrasound imaging, Medical physics, 46 (2019) 590-600.
[22] M.A. Averkiou, M.F. Bruce, J.E. Powers, P.S. Sheeran, P.N. Burns, Imaging Methods for Ultrasound Contrast Agents, Ultrasound in medicine & biology, 46 (2020) 498-517.
[23] C.F. Dietrich, M. Averkiou, M.B. Nielsen, R.G. Barr, P.N. Burns, F. Calliada, V. Cantisani, B. Choi, M.C. Chammas, D.A. Clevert, M. Claudon, J.M. Correas, X.W. Cui, D. Cosgrove, M. D'Onofrio, Y. Dong, J. Eisenbrey, T. Fontanilla, O.H. Gilja, A. Ignee, C. Jenssen, Y. Kono, M. Kudo, N. Lassau, A. Lyshchik, M. Franca Meloni, F. Moriyasu, C. Nolsøe, F. Piscaglia, M. Radzina, A. Saftoiu, P.S. Sidhu, I. Sporea, D. Schreiber-Dietrich, C.B. Sirlin, M. Stanczak, H.P. Weskott, S.R. Wilson, J.K. Willmann, T.K. Kim, H.J. Jang, A. Vezeridis, S. Westerway, How to perform Contrast-Enhanced Ultrasound (CEUS), Ultrasound international open, 4 (2018) E2-e15.
[24] C. Strouthos, M. Lampaskis, V. Sboros, A. McNeilly, M. Averkiou, Indicator dilution models for the quantification of microvascular blood flow with bolus administration of ultrasound contrast agents, IEEE transactions on ultrasonics, ferroelectrics, and frequency control, 57 (2010) 1296-1310.
[25] M.A. Averkiou, E.K. Juang, M.K. Gallagher, M.A. Cuevas, S.R. Wilson, R.G. Barr, P.L. Carson, Evaluation of the Reproducibility of Bolus Transit Quantification With Contrast-Enhanced Ultrasound Across Multiple Scanners and Analysis Software Packages-A Quantitative Imaging Biomarker Alliance Study, Investigative radiology, 55 (2020) 643-656.
[26] C. Krolak, A. Wei, M. Shumaker, M. Dighe, M. Averkiou, A Comprehensive and Repeatable Contrast-Enhanced Ultrasound Quantification Approach for Clinical Evaluations of Tumor Blood Flow, Investigative radiology, 60 (2025) 281-290.
[27] C. Einen, S. Snipstad, H.F. Wesche, V. Nordlund, E.J. Devold, N. Amini, R. Hansen, E. Sulheim, C.L. Davies, Impact of the tumor microenvironment on delivery of nanomedicine in tumors treated with ultrasound and microbubbles, Journal of controlled release : official journal of the Controlled Release Society, 378 (2025) 656-670.
[28] C. Voutouri, F. Mpekris, M. Panagi, C. Krolak, C. Michael, J.D. Martin, M.A. Averkiou, T. Stylianopoulos, Ultrasound stiffness and perfusion markers correlate with tumor volume responses to immunotherapy, Acta biomaterialia, 167 (2023) 121-134.
[29] D. Fukumura, R.K. Jain, Tumor microvasculature and microenvironment: targets for anti-angiogenesis and normalization, Microvascular research, 74 (2007) 72-84.
[30] J.A. Nagy, S.H. Chang, S.C. Shih, A.M. Dvorak, H.F. Dvorak, Heterogeneity of the tumor vasculature, Seminars in thrombosis and hemostasis, 36 (2010) 321-331.
[31] J. D., T. B., H. V., L. J., B. K., Super-Resolution Ultrasound Imaging of Tumor Angiogenesis and Evaluation of Treatment Response to a Vascular Disrupting Agent, 2024 IEEE International Symposium on Biomedical Imaging (ISBI), (2024) pp. 1-5.
[32] K.M. Laginha, S. Verwoert, G.J. Charrois, T.M. Allen, Determination of doxorubicin levels in whole tumor and tumor nuclei in murine breast cancer tumors, Clinical cancer research : an official journal of the American Association for Cancer Research, 11 (2005) 6944-6949.
[33] R.G. Barr, P. Huang, Y. Luo, X. Xie, R. Zheng, K. Yan, X. Jing, Y. Luo, H. Xu, X. Fei, J.M. Lee, Contrast-enhanced ultrasound imaging of the liver: a review of the clinical evidence for SonoVue and Sonazoid, Abdominal radiology (New York), 45 (2020) 3779-3788.
[34] S. Keller, M. Bruce, M.A. Averkiou, Ultrasound Imaging of Microbubble Activity during Sonoporation Pulse Sequences, Ultrasound in medicine & biology, 45 (2019) 833-845.
[35] S. Bulner, A. Prodeus, J. Gariepy, K. Hynynen, D.E. Goertz, Enhancing Checkpoint Inhibitor Therapy with Ultrasound Stimulated Microbubbles, Ultrasound in medicine & biology, 45 (2019) 500-512.

[36] H.L. Liu, H.Y. Hsieh, L.A. Lu, C.W. Kang, M.F. Wu, C.Y. Lin, Low-pressure pulsed focused ultrasound with microbubbles promotes an anticancer immunological response, Journal of translational medicine, 10 (2012) 221.
[37] M. Todorova, V. Agache, O. Mortazavi, B. Chen, R. Karshafian, K. Hynynen, S. Man, R.S. Kerbel, D.E. Goertz, Antitumor effects of combining metronomic chemotherapy with the antivascular action of ultrasound stimulated microbubbles, International journal of cancer, 132 (2013) 2956-2966.
[38] A. Bellary, A. Villarreal, R. Eslami, Q.J. Undseth, B. Lec, A.M. Defnet, N. Bagrodia, J.J. Kandel, M.A. Borden, S. Shaikh, R. Chopra, T.W. Laetsch, L.J. Delaney, C.M. Shaw, J.R. Eisenbrey, S.L. Hernandez, S.R. Sirsi, Perfusion-guided sonopermeation of neuroblastoma: a novel strategy for monitoring and predicting liposomal doxorubicin uptake in vivo, Theranostics, 10 (2020) 8143-8161.
[39] Y. He, Y. Feng, D. Qiu, M. Lin, H. Jin, Z. Hu, X. Huang, S. Ma, Y. He, M. Lai, W. Jin, J. Liu, Regulation of IFP in solid tumours through acoustic pressure to enhance infiltration of nanoparticles of various sizes, Journal of drug targeting, 32 (2024) 964-976.
[40] N. Xiao, J. Liu, L. Liao, J. Sun, W. Jin, X. Shu, Ultrasound Combined With Microbubbles Increase the Delivery of Doxorubicin by Reducing the Interstitial Fluid Pressure, Ultrasound quarterly, 35 (2019) 103-109.
[41] M. Apfelbeck, T. Loupas, M. Chaloupka, D.A. Clevert, Improved diagnostic confidence using Super Resolution CEUS imaging in testicular lesions, Clinical hemorheology and microcirculation, 88 (2024) S113-s125.
[42] T. Loupas, Microvascular Imaging Super Resolution (MVI SR) and Time of Arrival Super Resolution (TOA SR) technologies,
in https://www.documents.philips.com/assets/20240718/6c9282d90889454cb0fcb1b1016b8e25.pdf.
[43] K. Welsher, S.P. Sherlock, H. Dai, Deep-tissue anatomical imaging of mice using carbon nanotube fluorophores in the second near-infrared window, Proceedings of the National Academy of Sciences of the United States of America, 108 (2011) 8943-8948.
[44] Q. Wu, M. Gray, C.A.B. Smith, L. Bau, R.O. Cleveland, C. Coussios, E. Stride, Challenges in classifying cavitation: Correlating high-speed optical imaging and passive acoustic mapping of cavitation dynamics, The Journal of the Acoustical Society of America, 156 (2024) 3608-3620.
[45] C.W. Burke, A.L. Klibanov, J.P. Sheehan, R.J. Price, Inhibition of glioma growth by microbubble activation in a subcutaneous model using low duty cycle ultrasound without significant heating, Journal of neurosurgery, 114 (2011) 1654-1661.
[46] G.J. Czarnota, R. Karshafian, P.N. Burns, S. Wong, A. Al Mahrouki, J.W. Lee, A. Caissie, W. Tran, C. Kim, M. Furukawa, E. Wong, A. Giles, Tumor radiation response enhancement by acoustical stimulation of the vasculature, Proceedings of the National Academy of Sciences of the United States of America, 109 (2012) E2033-2041.
[47] A. El Kaffas, J. Nofiele, A. Giles, S. Cho, S.K. Liu, G.J. Czarnota, Dll4-notch signalling blockade synergizes combined ultrasound-stimulated microbubble and radiation therapy in human colon cancer xenografts, PloS one, 9 (2014) e93888.
[48] P. Huang, Y. Zhang, J. Chen, W. Shentu, Y. Sun, Z. Yang, T. Liang, S. Chen, Z. Pu, Enhanced antitumor efficacy of ultrasonic cavitation with up-sized microbubbles in pancreatic cancer, Oncotarget, 6 (2015) 20241-20251.
[49] J.H. Hwang, A.A. Brayman, M.A. Reidy, T.J. Matula, M.B. Kimmey, L.A. Crum, Vascular effects induced by combined 1-MHz ultrasound and microbubble contrast agent treatments in vivo, Ultrasound in medicine & biology, 31 (2005) 553-564.
[50] P. Lai, C. Tarapacki, W.T. Tran, A. El Kaffas, J. Lee, C. Hupple, S. Iradji, A. Giles, A. Al-Mahrouki, G.J. Czarnota, Breast tumor response to ultrasound mediated excitation of microbubbles and radiation therapy in vivo, Oncoscience, 3 (2016) 98-108.
[51] P.T. Yemane, A.K.O. Åslund, S. Snipstad, A. Bjørkøy, K. Grendstad, S. Berg, Y. Mørch, S.H. Torp, R. Hansen, C.L. Davies, Effect of Ultrasound on the Vasculature and Extravasation of Nanoscale Particles Imaged in Real Time, Ultrasound in medicine & biology, 45 (2019) 3028-3041.
[52] M. Averkiou, M. Lampaskis, K. Kyriakopoulou, D. Skarlos, G. Klouvas, C. Strouthos, E. Leen, Quantification of tumor microvascularity with respiratory gated contrast enhanced ultrasound for monitoring therapy, Ultrasound in medicine & biology, 36 (2010) 68-77.
[53] A. Dizeux, T. Payen, G. Barrois, D. Le Guillou Buffello, S.L. Bridal, Reproducibility of Contrast-Enhanced Ultrasound in Mice with Controlled Injection, Molecular imaging and biology, 18 (2016) 651-658.
[54] H. Ryu, J.H. Kim, S. Lee, J.K. Han, Therapeutic response monitoring after targeted therapy in an orthotopic rat model of hepatocellular carcinoma using contrast-enhanced ultrasound: Focusing on inter-scanner, and inter-operator reproducibility, PloS one, 15 (2020) e0244304.

[55] D. Wildner, L. Pfeifer, R.S. Goertz, T. Bernatik, J. Sturm, M.F. Neurath, D. Strobel, Dynamic contrast-enhanced ultrasound (DCE-US) for the characterization of hepatocellular carcinoma and cholangiocellular carcinoma, Ultraschall in der Medizin (Stuttgart, Germany : 1980), 35 (2014) 522-527.
[56] S.J. Hunt, T. Gade, M.C. Soulen, S. Pickup, C.M. Sehgal, Antivascular ultrasound therapy: magnetic resonance imaging validation and activation of the immune response in murine melanoma, Journal of ultrasound in medicine : official journal of the American Institute of Ultrasound in Medicine, 34 (2015) 275-287.
[57] W. Labriji, J. Clauzel, J.L. Mestas, M. Lafond, C. Lafon, A.S. Salabert, L. Hirschler, J.M. Warnking, E.L. Barbier, I. Loubinoux, F. Desmoulin, Evidence of cerebral hypoperfusion consecutive to ultrasound-mediated blood-brain barrier opening in rats, Magnetic resonance in medicine, 89 (2023) 2281-2294.
[58] S. Rigollet, A. Delphin, L. Chalet, T. Ador, E. Dumont, B. Lemasson, T. Christen, C. Pichon, A. Delalande, V. Stupar, E.L. Barbier, Microvascular and astrocytic responses to repeated magnetic resonance-guided focused ultrasound, Journal of controlled release : official journal of the Controlled Release Society, 386 (2025) 114151.
[59] S. Rigollet, C. Rome, T. Ador, E. Dumont, C. Pichon, A. Delalande, E.L. Barbier, V. Stupar, FUS-mediated BBB opening leads to transient perfusion decrease and inflammation without acute or chronic brain lesion, Theranostics, 14 (2024) 4147-4160.
[60] S.B. Keller, Y.N. Wang, S. Totten, R.S. Yeung, M.A. Averkiou, Safety of Image-Guided Treatment of the Liver with Ultrasound and Microbubbles in an in Vivo Porcine Model, Ultrasound in medicine & biology, 47 (2021) 3211-3220.
[61] Y. Wu, J. Li, L. Shu, Z. Tian, S. Wu, Z. Wu, Ultrasound combined with microbubble mediated immunotherapy for tumor microenvironment, Frontiers in pharmacology, 15 (2024) 1304502.
[62] S.B. Keller, M.A. Averkiou, The Role of Ultrasound in Modulating Interstitial Fluid Pressure in Solid Tumors for Improved Drug Delivery, Bioconjugate chemistry, 33 (2022) 1049-1056.
[63] A. Mohammadabadi, R.N. Huynh, A.S. Wadajkar, R.G. Lapidus, A.J. Kim, C.B. Raub, V. Frenkel, Pulsed focused ultrasound lowers interstitial fluid pressure and increases nanoparticle delivery and penetration in head and neck squamous cell carcinoma xenograft tumors, Physics in medicine and biology, 65 (2020) 125017.
[64] F. Xi, Y. Feng, Q. Chen, L. Chen, J. Liu, Microbubbles Ultrasonic Cavitation Regulates Tumor Interstitial Fluid Pressure and Enhances Sonodynamic Therapy, Frontiers in oncology, 12 (2022) 852454.
[65] Y. Xiang, L. Tang, H. Pang, H. Xu, Y. He, Y. Feng, L. Ju, L. Zhang, D. Wang, Ultrasound -Induced Thermal Effect Enhances the Efficacy of Chemotherapy and Immunotherapy in Tumor Treatment, International journal of nanomedicine, 19 (2024) 6677-6692.
[66] T. Luo, L. Yao, Y. Wu, Y. Zhang, L. Lu, P. He, N. Li, X. Dong, Z. Liu, Ultrasound-Stimulated Microbubbles Cavitation Combined with Nitric Oxide Signaling Pathway to Alleviate Tumor Hypoperfusion and Hypoxia in MC38 Tumor Model, Academic radiology, 32 (2025) 4121-4133.
[67] Y. Zhao, D. Shi, L. Guo, M. Shang, X. Sun, D. Meng, S. Xiao, X. Wang, J. Li, Ultrasound targeted microbubble destruction-triggered nitric oxide release via nanoscale ultrasound contrast agent for sensitizing chemoimmunotherapy, Journal of nanobiotechnology, 21 (2023) 35.
[68] Y. He, M. Yu, J. Wang, F. Xi, J. Zhong, Y. Yang, H. Jin, J. Liu, Improving the Therapeutic Effect of Ultrasound Combined With Microbubbles on Muscular Tumor Xenografts With Appropriate Acoustic Pressure, Frontiers in pharmacology, 11 (2020) 1057.
[69] S. Snipstad, S. Berg, Ý. Mørch, A. Bjørkøy, E. Sulheim, R. Hansen, I. Grimstad, A. van Wamel, A.F. Maaland, S.H. Torp, C.L. Davies, Ultrasound Improves the Delivery and Therapeutic Effect of Nanoparticle-Stabilized Microbubbles in Breast Cancer Xenografts, Ultrasound in medicine & biology, 43 (2017) 2651-2669.
[70] Y. Wang, Y. Li, K. Yan, L. Shen, W. Yang, J. Gong, K. Ding, Clinical study of ultrasound and microbubbles for enhancing chemotherapeutic sensitivity of malignant tumors in digestive system, Chinese journal of cancer research = Chung-kuo yen cheng yen chiu, 30 (2018) 553-563.

# Chapter 5. TRANSIENT TUMOR PERFUSION LOSS: EVALUATING THE SPATIAL AND TEMPORAL DYNAMICS OF BLOOD FLOW CHANGES INDUCED BY ULTRASOUND CAVITATION TREATMENTS

Connor Krolak, Lance De Koninck, Sherry Gu, Yak-Nam Wang, Michalakis Averkiou

*Submitted to Ultrasonics Apr. 2026*

**Abstract**

Ultrasound-mediated microbubble cavitation can induce transient tumor perfusion loss (TTPL), yet the pressure-dependent magnitude and short-timescale recovery of this effect remains poorly defined. This study investigated how acoustic pressure governs both the extent and duration of TTPL following a single cavitation exposure. Subcutaneous hepatocellular carcinoma tumors (HEPG2 human cell line) in athymic nude mice (n = 15) received a 1-second cavitation treatment at peak-negative pressures of 1.4, 2.8, or 4.1 MPa. Due to the small f-number of the transducer employed, the estimated average peak negative pressures of these conditions within the tumor were 0.6, 1.1, and 1.7 MPa respectively. Tumor perfusion was evaluated using contrast-enhanced ultrasound (CEUS) immediately (within 1 minute), 5, 15, 30, and 60 minutes after treatment. Perfused area loss was quantified with a maximum intensity projection time-area curve (MIP-TAC) metric. Cavitation activity was assessed using passive cavitation detection (PCD), and histology evaluated acute tissue effects. Low acoustic pressure produced only partial perfusion loss with full recovery within 5 minutes. Moderate acoustic pressure induced substantial TTPL followed by near complete recovery by 15 minutes. High-pressure treatment caused complete perfusion loss in all tumors, with initial recovery at 15 minutes but also with a subsequent decline over the hour. Elevated broadband energy recorded with PCD confirmed inertial cavitation in the moderate and high conditions. Histology revealed damage-associated staining in 1/5 moderate-pressure tumors and 3/5 high-pressure tumors, consistent with pressure-dependent mechanical injury, possibly contributing to the gradual decline in tumor perfusion observed after initial rebound in the high-pressure condition.

## 5.1 INTRODUCTION

Contrast-enhanced ultrasound (CEUS), or the enhancement of ultrasound images with microbubble contrast agents, has been used as a non-invasive diagnostic tool for evaluating blood flow in a variety of clinical applications [1-3]. Utilizing contrast agents and ultrasound at higher acoustic pressures than those used for imaging generates ultrasound-mediated microbubble cavitation, or the rapid expansion and contraction of the gas core in response to ultrasound waves. Sonication of microbubbles with cavitation-inducing ultrasound conditions offers a non-invasive way to harness the mechanical and thermal bioeffects generated by these microbubbles for targeted therapeutic purposes [4-6]. The acoustic conditions applied, especially pressure amplitude and the number of cycles, govern the strength of these forces and the biological effects they produce [7]. Lower pressures are commonly used to enhance drug delivery by promoting vascular permeability [8], while higher pressures can alter the tumor microenvironment by reducing interstitial fluid pressure or inducing localized necrosis [9, 10].

Interestingly, under certain ultrasound conditions leveraged in cavitation treatments, alterations and reduction of tumor blood flow following exposure have been observed, which we have named transient tumor perfusion loss (TTPL) [11]. This phenomenon is thought to arise because tumor vasculature characterized by small, immature, and poorly developed vessels, is more vulnerable to the mechanical forces generated during microbubble cavitation. Possible unique properties of tumor vessels contributing to this effect are supported by the tumor-specific nature of the response [12]. Although the underlying mechanism has not been fully defined, current hypotheses suggest platelet aggregation due to exposure of extravascular tissue factor or basement membrane [13], inadequate pericyte regulation [14], or activation of ceramide-mediated cell-death pathways [15] could be the primary drivers of TTPL. This effect has been typically observed in studies pairing cavitation treatments with systemic drugs, leveraging the enhanced localized delivery or modulation of the tumor immune microenvironment induced by microbubble cavitation observed in preclinical studies.

A growing body of literature utilizing cavitation treatments in preclinical studies have observed this TTPL phenomenon, and although microbubble agents were used for therapy, only a limited

subset of studies has incorporated CEUS to observe these effects in real time. Despite this, studies which observed tumor vasculature immediately following treatment appear to have general consensus that the degree of perfusion loss appears to correlate with acoustic pressure (**Table 1**). However, the ultrasound exposure conditions and microbubble formulations used to elicit perfusion loss vary widely amongst studies, encompassing differences in microbubble type (clinical versus experimental agents), delivery strategy (bolus versus infusion), and sonication duration, which ranges from brief exposures under five seconds to treatments extending beyond five minutes. This heterogeneity underscores the need for a direct comparison of acoustic parameters and standardized CEUS evaluations to enable a greater understanding of this vascular effect.

Many works observing TTPL assert that tumor vascular rebound occurs following cavitation treatments, but the temporal dynamics of this phenomenon have not been thoroughly explored. To our knowledge, only a small number of studies have assessed tumor vascular recovery from cavitation treatments over a 24-hour period or longer [12, 16-18], and only three have examined blood flow recovery within the first hour using CEUS [13, 19, 20]. However, reported outcomes vary substantially due to differences in acoustic parameters and sampling intervals. Intravital microscopy work observing cavitation treatments [14, 21] has provided extremely valuable mechanistic insight into vascular responses and recovery kinetics, but these studies do not use CEUS and are unable to capture whole-tumor perfusion, underscoring the need for CEUS imaging approaches capable of resolving both spatial and temporal heterogeneity in tumor blood flow. Observations from our own work [11], particularly the possible influence of TTPL on the efficacy of repeated treatments, motivated a deeper examination of how long these effects persist following cavitation, especially in the shorter timescale.

| Study | MI | TTPL Degree | Notes |
|---|---|---|---|
| [12] | 0.52 | Incomplete | Nearly full recovery at 24 h |
| [13] | 0.89 | Incomplete | Targeted microbubbles only |
| [22] | 1.0-1.2 | Incomplete | Greatest disruption at 1% duty cycle |
| [17] | 1.02 | Incomplete | 71% (small MBs), 50% (large MBs) |
| [23] | 1.35 | Substantial | Infusion; 70% (1 pulse), 30% (3 pulses) |
| [12] | 1.55 | Substantial | 70% remaining at 24 h |
| [18] | 1.65 | Substantial | Central shutdown |
| [24] | 1.65 | Substantial | ~10x reduction in bolus slope, central shutdown |
| [25] | 1.65 | Substantial | Peak intensity decreased 88% |
| [13] | 1.79 | Incomplete | Targeted microbubbles only |
| [26] | 2.0 | Substantial | — |
| [20] | 2.85 | Substantial | ~50% recovery at 1 h, 80% at 24 h |
| [27] | 3.0 | Complete | Unfocused |
| [12] | 3.1 | Complete | Sustained over 24 h |
| [16] | 3.5 | Substantial | Recovery to 60–75% in 1 h |
| [19] | 4.6 | Complete | Reported full recovery in 10 min |
| [12] | 5.2 | Complete | Sustained over 24 h |
| [20] | 5.27 | Complete | Recovery to 23% at 24 h |

**Table 5.1**: Summary of reported transient tumor perfusion loss (TTPL) outcomes across mechanical index (MI) levels from published studies. TTPL degree is categorized using a rating scheme based on the percentage of tumor vascularity remaining after treatment derived from qualitative observations or quantitative perfusion metrics with the following categories: incomplete (>50% tumor vascularity remaining), substantial (25–50% remaining), and complete perfusion loss (<25% remaining). The table lists MI, TTPL degree, and relevant notes for each study.

This study was designed to define how acoustic pressure governs both the extent and the duration of TTPL following microbubble cavitation treatments. To isolate the specific contribution of pressure, we delivered a single one-second treatment rather than repeated exposures and held all acoustic parameters constant except for peak negative pressure, examining three levels to test the hypothesis that higher pressures would produce more pronounced and longer lasting perfusion loss. Tumor blood flow was monitored with CEUS immediately (within 1 minute), 5, 15, 30, and 60 minutes after treatment. Tumor perfused area loss was quantified with maximum intensity projection time-area curve (MIP-TAC) analysis [11]. Cavitation activity was evaluated using passive cavitation detection (PCD), and histology was performed to assess potential tissue damage

to characterize the resulting vascular effects observed with CEUS. Through this approach, the study aims to clarify the temporal dynamics and vascular consequences of cavitation-based treatments, providing insight needed to optimize therapeutic strategies that rely on or want to avoid cavitation-induced transient tumor perfusion loss.

## 5.2 MATERIALS AND METHODS

### 5.2.1 *Tumor cell line and mouse model preparation*

All animal protocols performed were approved by the Institutional Animal Care and Use Committee (IACUC) at the University of Washington, Seattle. This study used a human hepatocellular carcinoma line (HCC), specifically HEPG2 (American Type Culture Collection, HB-8065), to connect this work with prior and anticipated studies examining HCCs. Cells were cultured at 37°C and 5% CO2, in Eagle's Minimum Essential Medium supplemented with 10% fetal bovine serum and 1% antibiotic/antimycotic. HEPG2 cells suspended in 50 µL of phosphate buffered saline ($4*10^4$ cells/µL) were mixed with 50 µL of Matrigel and implanted in the hind flank in anesthetized eight- to twelve-week-old athymic nude mice (Charles River Laboratories, Wilmington, MA) with a 23G needle. Tumor dimensions were measured twice weekly with B-mode ultrasound imaging on a GE LogicBook XP (General Electric HealthCare, Chicago, IL, USA), a portable ultrasound scanner, and animals were enrolled in the study once the largest tumor diameter exceeded 8 mm, or an estimated tumor volume of approximately 120 $mm^3$ based on an ellipsoidal calculation, typically observed 4 to 6 weeks after inoculation. Recruited mouse tumor volume by condition derived from B-mode images of the tumor are presented in **Figure 5.1**.

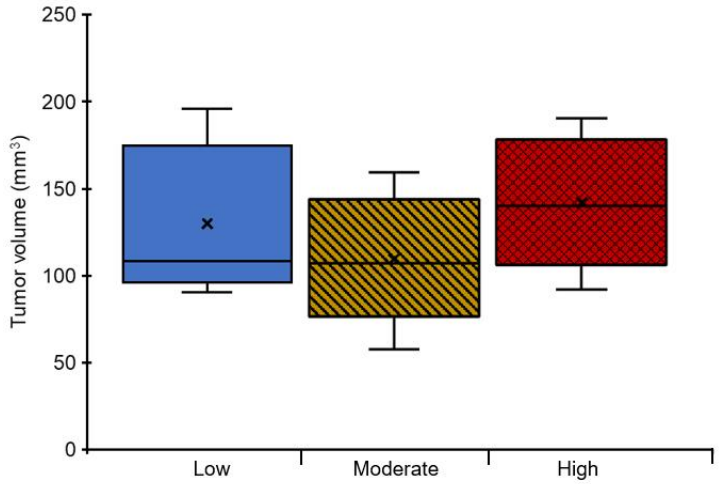


**Figure 5.1**: Tumor sizing across groups. Box and whisker plots of tumor volume by condition (n = 5 per group). Tumor volume is represented by ellipsoidal estimation from B-mode images. The "x" represents the mean value.

### 5.2.2 *Contrast agent*

Lumason microbubbles (Bracco Suisse SA, Geneva, Switzerland), known as SonoVue outside the United States, were used in this study because they are clinically approved for characterizing focal liver lesions in the United States and in numerous countries across Europe and Asia [29]. A microbubble dose of 50 μL per injection was selected based on prior studies [11, 28], providing sufficient signal while avoiding acoustic shadowing, and this dosing strategy was applied to all injections. Repeated bolus injections were chosen instead of infusion to avoid the added complexity of infusion systems, accommodate the limited injection volumes feasible in small animals, and deliver the most concentrated microbubble bolus.

### 5.2.3 *Ultrasound parameters*

A single-element transducer (BUL2, 1.19 MHz, 4.7 cm diameter, 5.1 cm focal length) driven by an RF amplifier (2200L, Electronics and Innovation, Rochester, NY, USA) was used to enable precise control of acoustic parameters. Transmit pulses were generated on an arbitrary function generator (AFG3102C, Tektronix, Beaverton, OR, USA) at 1.19 MHz with a long pulse duration (1000 cycles) and a short pulse-repetition time of 10 ms to maximize inertial cavitation dose. This particular pulse-repetition time was employed as dissolution time for microbubbles has been found to be approximately 30 ms [30]. By firing at a faster rate, we could possibly re-interrogate the

remaining gas even after the microbubble shell has been ruptured to continue to generate mechanical forces on the tumor. Although the maximum pressure occurs 50 mm from the transducer, an axial distance of 55 mm was selected as the treatment location to slightly increase the 6-dB spot size (length = 13 mm, width = 2 mm) with the tumor volume. A simulated acoustic field derived from a numerical solution of the Rayleigh integral for the circular piston therapeutic transducer with a representative 8 mm diameter tumor is shown in **Figure 5.2**. Three acoustic conditions with peak-negative pressures at 55 mm of 1.4, 2.8, and 4.1 MPa were evaluated to sample the range of acoustic pressures employed in cavitation studies where perfusion changes were observed. These acoustic pressures were measured in a water tank setup with a 0.4 mm membrane hydrophone (UT1604-225; Precision Acoustics, Dorchester, UK) placed 55 mm from the transducer. Experimental and simulated data normalized to the pressure at the focus is displayed along the propagation axis in **Fig. 5.2A**, and for the focal beampattern in **Fig. 5.2B**. However, due to the small f-number of the transducer (highly focused) employed in this study, the pressure within the tumor was non-uniform, with a majority of the tumor volume experiencing a much lower acoustic pressure. Average peak-negative pressure within the tumor was calculated from the simulated field for an 8 mm tumor placed at 55 mm (as shown in **Fig. 5.2C**), and was estimated to be 0.6, 1.1, and 1.7 MPa for the three conditions respectively. These two pressure values (the pressure at 55 mm and average tumor pressure) per condition are listed in **Table 5.2**, and these conditions will be referred to as the low, moderate, and high-pressure condition.

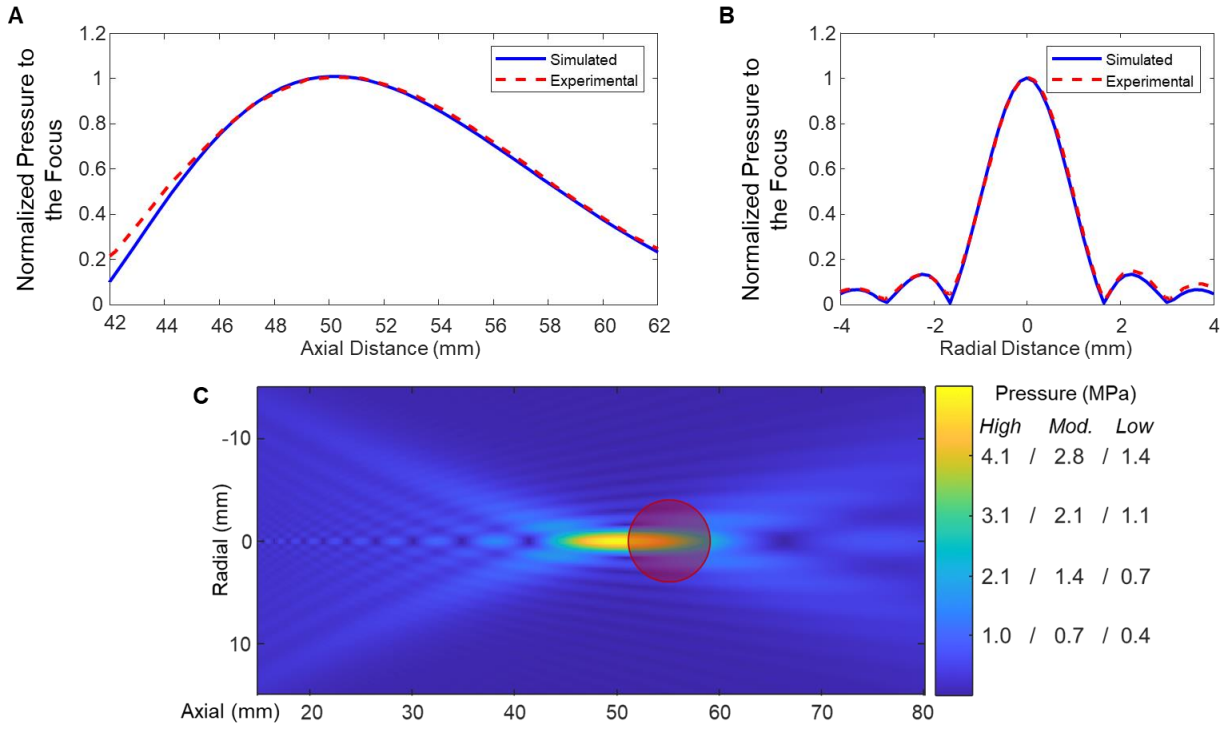


**Figure 5.2**: Beam field characteristics for the single element therapeutic transducer. Experimental and simulated pressure normalized to the pressure at the focus are displayed for the propagation axis (A) and for the focal beampattern (B). (C) The simulated beam field with a representative 8 mm diameter tumor centered 55 mm from the source (as per our alignment). Theoretical peak negative pressures for the three acoustic conditions are listed.

| Ultrasound Condition | Peak negative pressure at 55 mm (tumor center) | Estimated average peak negative pressure within the tumor area |
|---|---|---|
| Low | 1.4 MPa | 0.6 MPa |
| Moderate | 2.8 MPa | 1.1 MPa |
| High | 4.1 MPa | 1.7 MPa |

**Table 5.2**: Acoustic pressures at the tumor center (55 mm) and estimated average tumor pressure of cavitation treatment pulses for the three ultrasound conditions employed in this study.

### 5.2.4 *Experimental setup and treatment procedure*

To account for the transducer spatial characteristics and the alignment of several probes to the tumor and allow for simultaneous treatment and imaging, a heated (37°C) and degassed water tank setup was utilized (**Figure 5.3**). The single element transducer powered by a function generator and amplifier as described above, was used for delivering the cavitation treatments. A Philips L12-

5 ultrasound probe on the iU22 scanner was used for small animal CEUS imaging. Another single element transducer centered at 5 MHz (C308, Evident Scientific, Waltham, MA) was also employed for in vivo passive cavitation detection (PCD) assessments. Before beginning the experiments, all three transducers were aligned to the same 3-D location using a thin vertical wire target. The PCD transducer was first positioned 5.1 cm from the wire (geometric focus) using a pulse-echo method. It was then fixed to that location and served as a receiver to align the therapeutic single element transducer and L12-5 probe at distances of 5.5 cm and 2.5 cm from the wire, respectively, and to match the PCD transducer's vertical position (see **Fig. 5.3**). After recording the wire's location on the L12-5 image, the wire target was removed from the water tank. Mice were induced at 3% isoflurane and maintained at 1.5–2% isoflurane and fitted with a 30G tail-vein catheter. They were secured to a custom restraining board, partially submerged in the water tank such that the tumor bearing flank was fully submerged while the animal's head remained above water, and positioned so that the tumor center aligned with the previously recorded wire location on the L12-5 image.

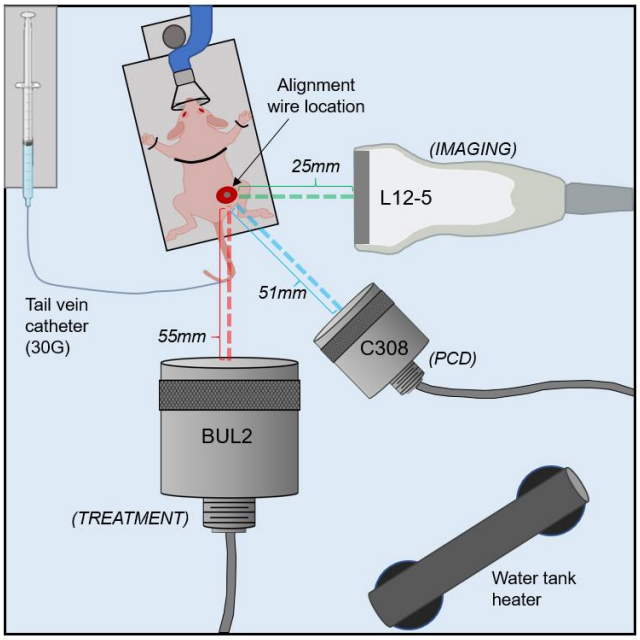


**Figure 5.3**: Schematic of a top-down view of the heated, degassed water tank experimental setup. Co-alignment of the treatment, imaging, and passive cavitation detecting probes to red circle, representing the subcutaneous tumor on the flank of the mouse. The black dot within the tumor indicates the location of the wire used to align the probes before the mouse was placed with the center of the tumor in the same location.

Mice were randomly divided into three groups (n = 5 per group) where they received cavitation treatments at the low, moderate, or high-pressure condition (see **Table 5.2**). The experimental timeline is summarized in **Figure 5.4**. A bolus of microbubbles was delivered before the cavitation treatment while the tumor was continuously scanned with CEUS (amplitude modulation, 4.1 MHz, 4 cycles, mechanical index = 0.06) to establish baseline tumor vascularity. A time-intensity curve was formed from a freeform polygon region of interest (ROI) of the tumor to determine when peak microbubble concentration within it had occurred, as illustrated in **Figure 5.4B**. The pulse train delivered for one second by the single element therapeutic transducer is displayed in **Figure 5.4C**. PCD measurements were acquired using an oscilloscope (DPO 7054C, Tektronix, Beaverton, OR, USA) operated with a segmented memory ("Fast Frame") mode. Prior to any microbubble injection, PCD was recorded in each animal to establish a baseline signal. During the cavitation treatment, scattered acoustic signals were captured from the first 50 delivered pulses (0.5 s of treatment time) at a sampling rate of 200 MS/s. After the cavitation treatment, repeated boluses of microbubbles were delivered while CEUS was performed at several time points to evaluate the resulting tumor blood flow changes, titled "post-treatment" scans. These image loops were collected immediately (within 1 minute), 5, 15, 30, and 60 minutes after treatment. Mice were sacrificed by isoflurane overdose immediately following the scan at the 60-minute mark, and tissue was harvested and fixed in 10% formalin for histological evaluation to assess cavitation-induced damage.

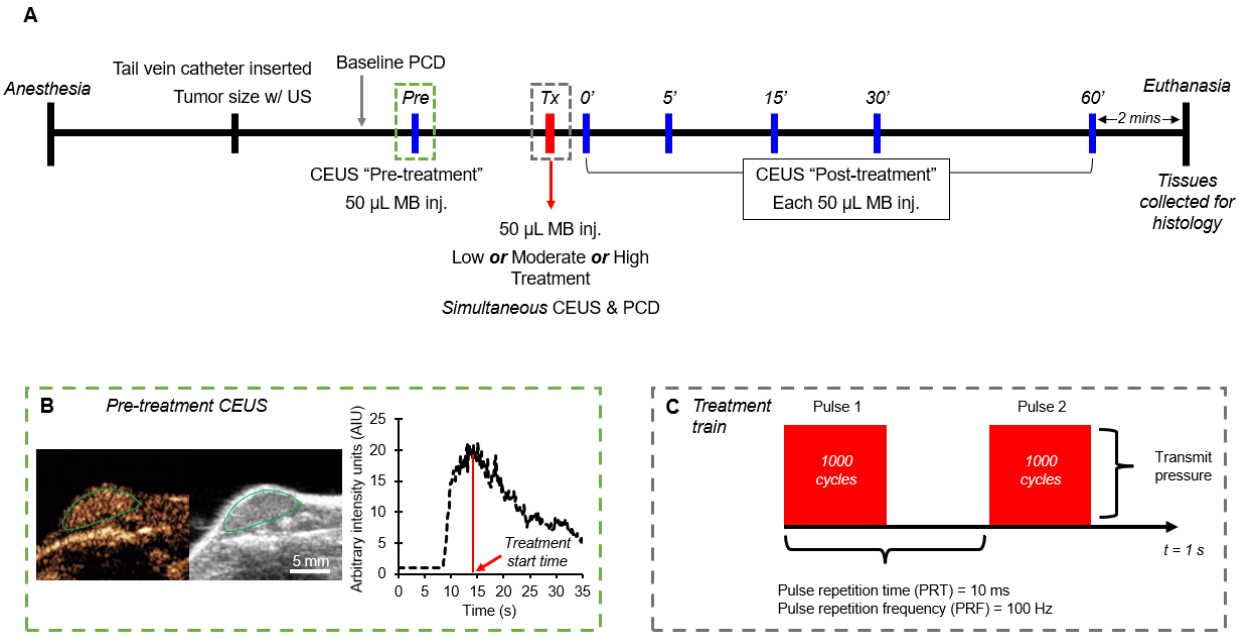


**Figure 5.4**: Experimental protocol overview. (A) Timeline of contrast-enhanced ultrasound (CEUS) evaluations, passive cavitation detection (PCD) measurements, and cavitation treatment delivery (Tx). MB = microbubble. (B) An example CEUS side-side image of a tumor and the resulting time-intensity curve performed during pre-treatment CEUS to determine cavitation treatment timing. (C) A schematic to illustrate the pulse train transmitted by the therapeutic transducer to perform the cavitation treatment.

### 5.2.5 *CEUS quantification – Maximum intensity projection time-area curve analysis*

The maximum intensity projection time-area curve (MIP-TAC) analysis used here (see **Figure 5**) was developed by our group to quantify the cavitation-induced tumor blood flow changes, or a phenomenon we titled TTPL [11]. Irregularities in tumor vasculature lead to substantial spatial heterogeneity in tumor blood flow [30, 31]. Furthermore, cavitation-based interventions have been shown to alter perfusion in a non-uniform manner across different tumor regions [14]. These observations indicate that assessing perfusion loss at a single time point may not adequately capture the full extent of tumor blood-volume dynamics following cavitation treatment, and thus our MIP-TAC approach was utilized to capture the spatial extent of TTPL. Pre- and post-treatment CEUS loops were exported from the scanner and processed with Philips QLAB's super-resolution method, which applies maximum intensity projection (MIP) with advanced motion compensation and further image processing to enhance spatial resolution. In a MIP loop, the brightest pixel intensities are cumulatively retained. The MIP loop was then analyzed in MATLAB to generate a

time-area curve (TAC), representing the normalized portion of the tumor exhibiting any microbubble signal over time, referred to as a MIP-TAC. A MIP-TAC reports the perfused area on a scale from 0 (no detected blood flow) to 100 (fully perfused). TTPL was evaluated by considering the MIP-TAC value 15 seconds after contrast arrival in the tumor, as this time point approximates the one-pass circulation time in mice [32], reducing confounding from bubble recirculation and limiting temporal smearing of contrast signal in the MIP due to motion. To evaluate changes in tumor vascularity over time, perfused area loss was calculated as the difference in MIP-TAC value from pre-treatment and each timepoint. Although consistent bolus microbubble delivery was confirmed with real-time CEUS imaging, the influence of injection variability was further mitigated with MIP-TAC as pixel brightness must only exceed the noise floor to be included in the area-based calculation.

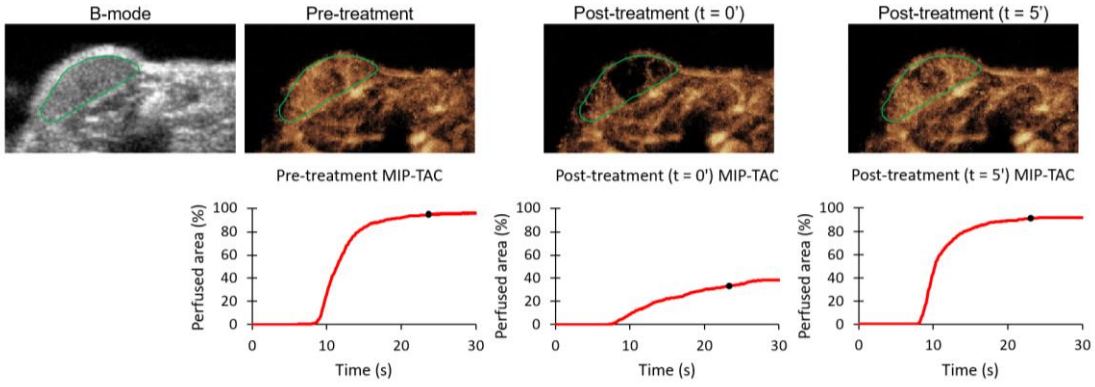


**Figure 5.5.** A representative example from the moderate pressure cavitation group to illustrate maximum intensity projection time-area curve (MIP-TAC) analysis. A B-mode image and maximum intensity projection (MIP) images before, immediately after, and 5 minutes after treatment are displayed, with their corresponding MIP-TACs. The black dot on each curve represents the timepoint 15 seconds after contrast arrival used to calculate perfused area.

### 5.2.6 *Passive cavitation analysis*

Processing of the received scattered signals during cavitation treatments followed the approach described in our previous work [11, 33]. Each waveform was first truncated to its original pulse length using a rectangular window, after which its mean value was removed to eliminate the oscilloscope's small DC offset. A one-sided power spectrum (scaled by 2 divided by the number of samples squared) was then computed for each truncated waveform. Broadband energy was

collected between the third harmonic, chosen to minimize contributions from the transmitted pulse, and 10 MHz, the approximate upper limit of the receiver bandwidth. Within this range, 0.3 MHz-wide bands centered on each harmonic and ultraharmonic were excluded, and the remaining bands were summed to obtain the broadband energy per pulse. This procedure was repeated for all pulses. The inertial cavitation dose (ICD) was calculated as the sum over the treatment duration of the product of broadband energy per pulse and pulse duration. To evaluate the temporal evolution of broadband energy within each pulse, a 40-cycle rectangular window (1.19 MHz) was applied to each truncated pulse and shifted by 20 cycles (50%) across the pulse. Broadband energy for each window was computed using the same method described above.

### 5.2.7 *Histology and immunohistochemistry analysis*

Tumor tissues were both flash-frozen in optimal cutting temperature (OCT) and fixed in formalin, transferred to 70% ethanol, and paraffin embedded. Taken from the tumor center, 4 μm sections were stained with H&E, kiel 67 (Ki67), cluster of differentiation (CD31), Annexin V, and cleaved caspase-3 (CC3) markers, with two sections analyzed per stain for each mouse. Staining was performed by the UW Histology and Imaging Core. Presence of localized architectural disruption in H&E, absence of Ki67, and presence of Annexin V or CC3 stains in similar regions of the tumor was used to evaluate cavitation-induced damage. Ki67 expression stains for proliferating tumor cells, while Annexin V and CC3 stain for early and late stage apoptosis respectively, with the absence of Ki67 and presence of Annexin V or CC3 indicating regions of cavitation-induced cell death. The additional abnormal appearance in H&E in these regions assisted in confirming that these regions likely resulted from localized disruption of cells from the cavitation treatment. IHC stains were visualized with 3,3′-diaminobenzidine (DAB), and stains were performed on separate sequential sections of the tumor.

### 5.2.8 *Statistical analysis*

A Kruskal-Wallis test with Dunn-Bonferroni post-hoc was used to evaluate if significant differences were observed in tumor perfused area loss between ultrasound conditions at each timepoint. This statistical analysis was repeated for all measured timepoints. The Kruskal-Wallis test was also performed to determine if average measured ICD differed significantly across

treatment conditions. Statistical analyses were performed in JASP version 0.96.0 (JASP Team 2026, Amsterdam, The Netherlands). For all analyses, the significance level was set to 0.05.

## 5.3 RESULTS

### 5.3.1 *Quantification of tumor blood flow changes*

CEUS imaging revealed pressure-dependent differences in TTPL following the cavitation treatment. Qualitatively, MIP CEUS images at immediately after treatment showed limited perfusion loss with the low-pressure condition, with an effectively complete recovery at 5 minutes that was sustained for all following observations (**Figure 5.6**). For the moderate-pressure condition, substantial perfusion loss was illustrated immediately after treatment, with maximal recovery observed 15 minutes after treatment which was sustained throughout the remaining observations. In the high-pressure condition, a complete absence of blood flow was observed immediately after treatment, uniquely also affecting peripheral tumor vessels and possible skin vessels proximal to the tumor. Maximal tumor reperfusion was observed by 15 minutes as well, but a regression of tumor perfusion was observed following this timepoint.

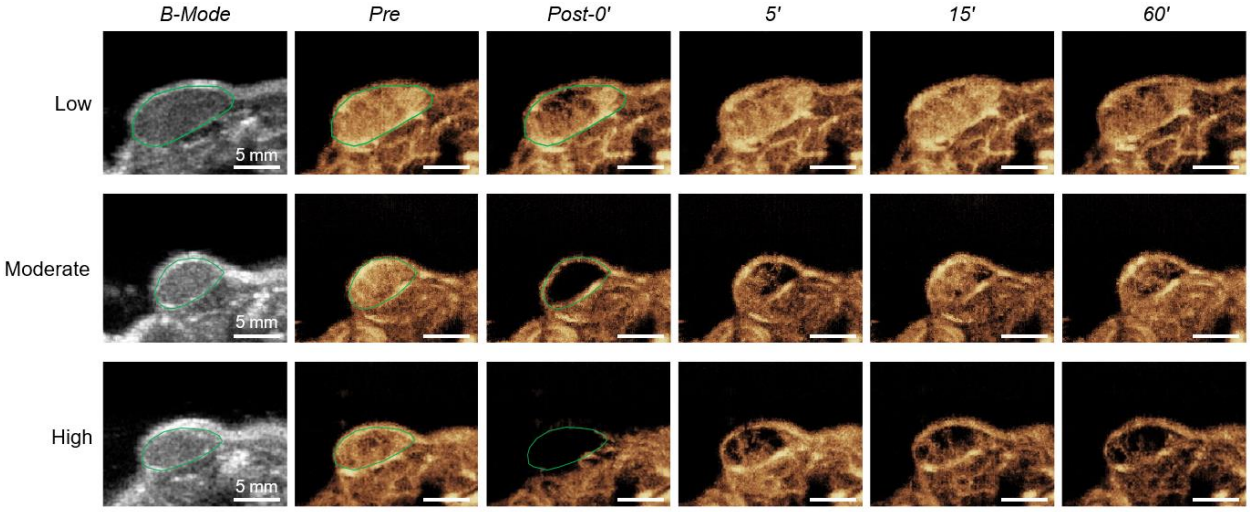


**Figure 5.6.** B-mode and maximum intensity projection (MIP) images at designated timepoints for a representative example from each treatment group. The tumor is outlined by a green region of interest in the B-mode and pre-treatment, and immediate post-treatment MIP images.

Quantitatively, MIP-TAC analysis demonstrated that the low-pressure condition produced variable responses that never reached full perfusion loss (35% tumor perfused area loss on average), with complete recovery occurring within 5 minutes (**Figure 5.7**). With the moderate-pressure condition,

tumors exhibited up to 80% perfused area loss. This perfusion loss was followed by a partial recovery to approximately a 20% perfused area deficit from baseline vascularity within 15 minutes, which was sustained throughout the hour. With the high-pressure condition, all tumors experienced complete perfusion loss, a significantly greater extent of TTPL than the low-pressure group ($p = 0.003$, Kruskal-Wallis with Dunn-Bonferroni post-hoc). Although perfusion recovered to 75-80% by 15 minutes as observed in the moderate-pressure condition, a gradual decline in perfusion was observed over the full hour of monitoring, to a significantly greater degree of perfusion loss than the low-pressure condition at the hour mark ($p = 0.017$, Kruskal-Wallis with Dunn-Bonferroni post-hoc).

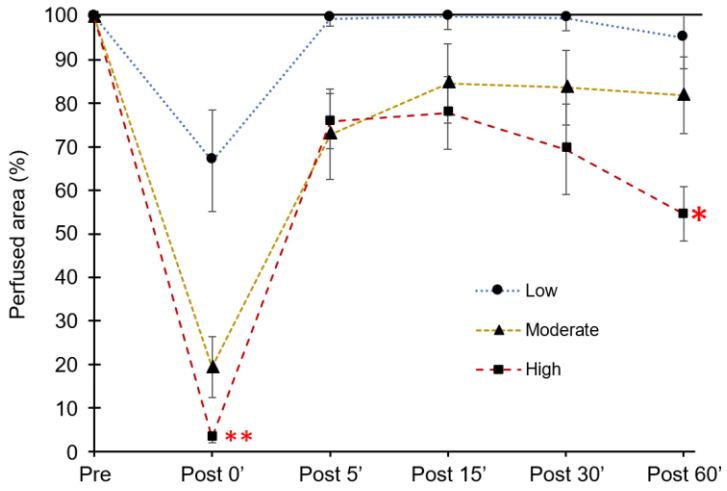


**Figure 5.7.** Tumor perfused area for each cavitation condition over time. Mean and standard error values at each timepoint are illustrated. The high-pressure condition experienced a significantly greater average perfused area loss compared to the low-pressure condition (Kruskal-Wallis with Dunn-Bonferroni post-hoc, high-low $p = 0.003$, ranked $\varepsilon^2$ effect size: 0.8, $n = 5$ per group). The average perfused area loss for the high-pressure condition was also significantly greater than the low-pressure condition at the 60-minute timepoint (Kruskal-Wallis with Dunn-Bonferroni post-hoc, high-low $p = 0.017$, ranked $\varepsilon 2$ effect size: 0.57, $n = 5$ per group). *$p < 0.05$, **$p < 0.01$.

### 5.3.2 *Evaluation of cavitation activity*

**Figure 5.8A** shows the average net broadband energy (baseline PCD measurement subtracted) measured during the first 50 transmitted pulses. With the low-pressure condition, broadband energy rose above baseline only for the first two pulses. Increasing the pressure to moderate condition elevated broadband energy for all 50 pulses, peaking at the third pulse and gradually decreasing to a steady state by approximately the 20$^{th}$ pulse. Raising the pressure further to the

high condition produced broadband energy levels similar to those in the moderate-pressure condition, indicating comparable cavitation activity despite the differing tumor responses observed in with CEUS evaluations. However, cavitation in the water was observed with imaging at this pressure, possibly confounding PCD measurements. **Figure 5.8B** displays the inertial cavitation dose (ICD) for the first 50 pulses. ICD was lowest in the low-pressure condition due to the limited magnitude and short duration of broadband energy generation. Measured ICD was similar for the moderate and high-pressure treatments, reflecting their comparable broadband energy magnitudes and sustained activity across multiple pulses. Both groups had significantly greater ICD on average compared to the low-pressure treatment (high-low p = 0.007, moderate-low p = 0.009, Kruskal-Wallis with Dunn's post-hoc).

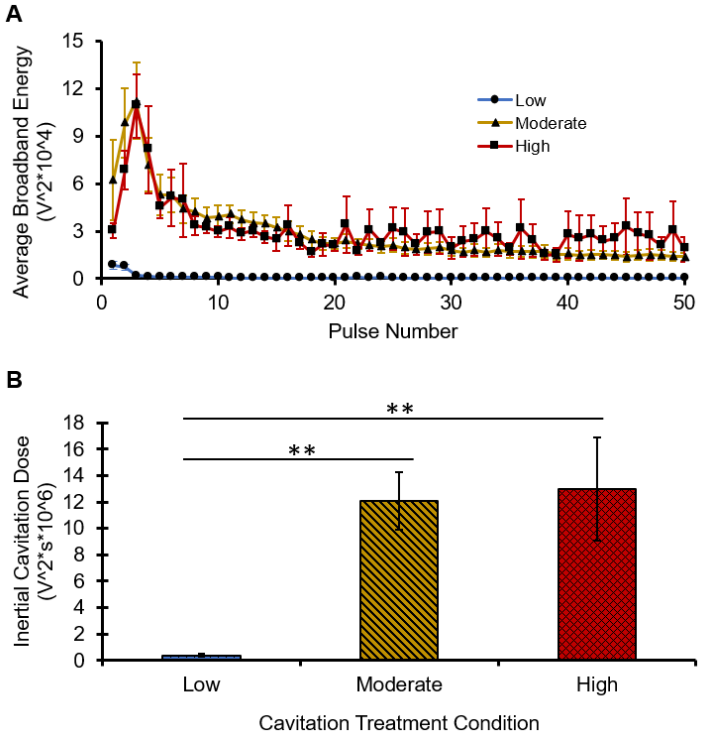


**Figure 5.8.** Passive cavitation detection measurements during treatments. (A) Average net broadband energy with standard error bars for the first 50 transmitted pulses in each condition. (B) Average inertial cavitation dose (ICD) with standard error bars over the 1 second treatment time. The moderate and high-pressure conditions demonstrated a significantly greater ICD compared to the low-pressure condition (Kruskal-Wallis with Dunn's post-hoc, high-low p = 0.007, moderate-low p = 0.009, ranked $\varepsilon^2$ effect size: 0.67, n = 5 per group). **p < 0.01.

### 5.3.3 *Histological evaluations*

Tissue stains were primarily evaluated to assess if acute tissue damage resulted from ultrasound treatments. Damage was qualitatively assessed through the presence of certain features in H&E, Ki67, and Annexin V or CC3 stains in the same region of the tumor. Representative samples from each condition with these stains is shown in **Figure 5.9**. In particular, appearance of localized regions of tissue homogenization in H&E combined with an absence of Ki67 expression and presence of Annexin V (early apoptosis) and/or CC3 (execution pathway, final stage of apoptosis) were used to determine if cavitation-induced damage had occurred. No abnormalities and no apoptosis were observed in the low-pressure case (**Figure 5.9A**). This staining pattern possibly associated with damage was only observed in one mouse in the moderate-pressure condition (this case shown in **Figure 5.9B**) and in 3 mice in the high-pressure condition (**Figure 5.9C**). In the moderate-pressure condition, only the Annexin V and not the CC3 stain appeared in the one mouse where possible damage occurred (**Figure 5.9B**). CD31 stains across all mice were generally analogous, indicating similar vascular properties as reflected by the comparable baseline vascularity observed with MIP-TAC of all recruited tumors.

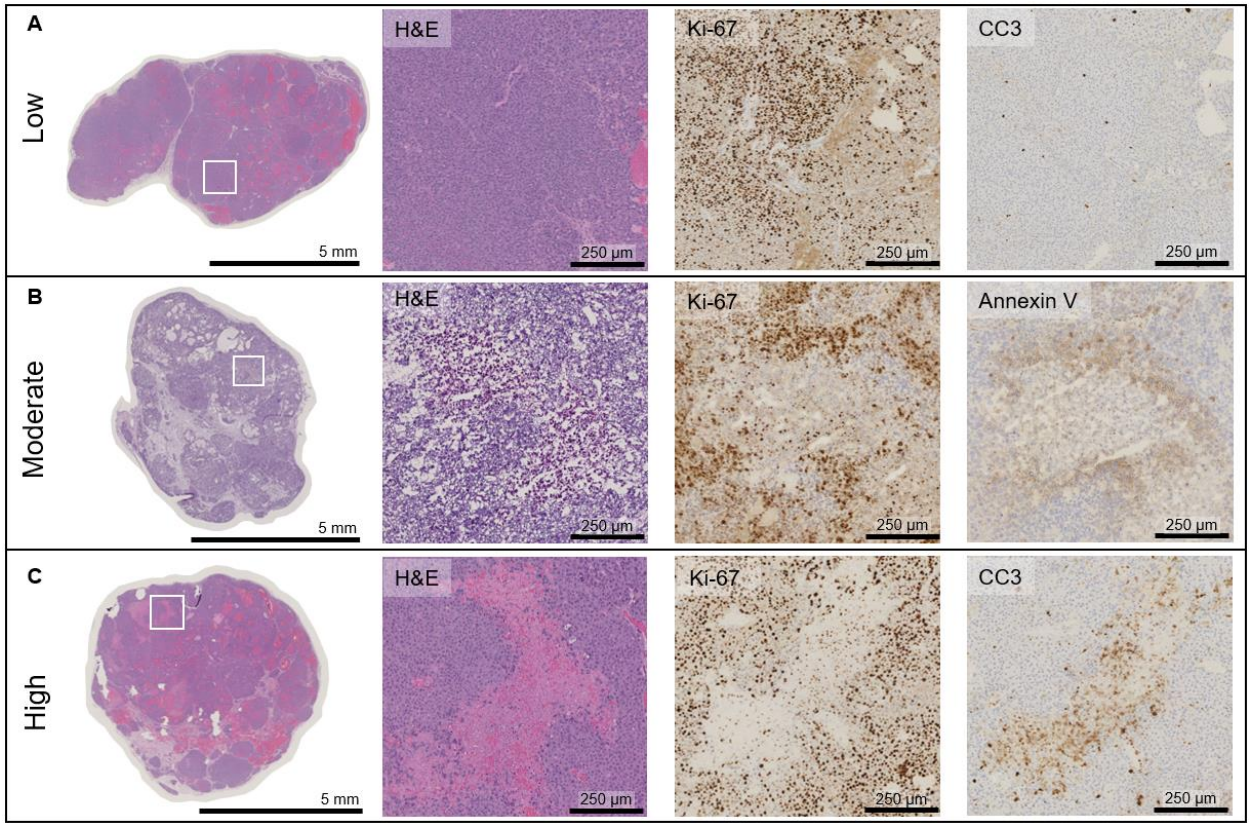


**Figure 5.9.** Representative histological images from each ultrasound condition. An example full section hematoxylin and eosin (H&E) image and H&E, Ki-67, and CC3 stains of a zoomed-in region of interest are displayed from left to right for the low (A), moderate (B), and high (C) conditions. In the far-right image in the moderate condition (B), an Annexin V image is displayed instead of a CC3 stain as only this apoptotic marker was positively stained for in this condition.

## 5.4 DISCUSSION

### 5.4.1 *Transient tumor perfusion loss scales with acoustic pressure*

Our findings demonstrate that the degree of transient tumor perfusion loss scales with acoustic pressure, with the greatest TTPL immediately after treatment observed at the highest pressures. The low-pressure condition exhibited only partial perfusion loss, with the moderate and high-pressure conditions exhibited significantly greater TTPL. However, the extent of TTPL was still greater in the high-pressure condition compared to the moderate, with all mice in the high-pressure condition exhibiting near complete blood flow cessation. These acoustic pressures and resulting degrees of TTPL generally align with vascular observations made at similar mechanical indices in other cavitation-based studies (**Table 5.1**). The relationship between TTPL and acoustic pressure

could be related to the heterogeneity of vessel sizes within tumors, as previous studies have demonstrated that small vessels (< 50 μm) responded to cavitation treatments at 1 MPa, while larger vessels only experienced blood flow events at greater acoustic pressures (>2 MPa) [14, 34]. Our work suggests that cavitation treatments above an acoustic pressure of 1 MPa (mechanical index of 0.9) would result in uniform TTPL throughout the tumor, likely due to this acoustic pressure inducing a cessation of blood flow in a majority of the tumor vessels. However, the transducer employed in our study had a very small focal spot relative to the size of the tumor as a high gain transducer was necessary to transmit high acoustic pressures, but this means that a majority of the tumor experienced acoustic pressures below that of the focus. This suggests that although we expect the trend with acoustic pressure to be the same, the acoustic pressure necessary for inducing TTPL throughout the entire tumor may be lower with a more uniform treatment region, and that the average estimated pressures reported here are more likely the main drivers of the immediate perfusion loss observed throughout the entire tumor.

Our vascular results also provided greater insights into the recovery dynamics of tumor perfusion following cavitation treatments, uniquely monitoring the effect of a single one second treatment. Only the low-pressure condition exhibited complete vascular recovery within the one-hour monitoring window, and this recovery occurred rapidly within approximately 5 minutes and was sustained throughout the hour. The average perfused area at 60 minutes decreased in one mouse exhibiting abnormal respirations, slightly reducing the average of this group at that timepoint. However, despite these all conditions differing in extent of TTPL immediately after treatment, similar rebound dynamics with considerable tumor perfusion recovery was observed within 5 minutes in the moderate and high conditions as well. However, unlike the low-pressure condition, these two higher pressure conditions both reached maximal reperfusion at the 15-minute timepoint, but still experienced reduced perfusion compared to their baseline measurements. In the high-pressure condition, a continuous reduction in tumor perfusion was observed at all timepoints beyond 15 minutes, reaching a significantly greater extent of perfusion loss at 60 minutes as compared to the low-pressure condition. This effect could be attributed to damage observed histologically in a majority of mice within this condition, possibly resulting from microvascular injury and permanent changes to the tumor microenvironment, as these two conditions reached

high acoustic pressures in small areas of the tumor similar in size perceived damage in histological observations.

Although the precise recovery dynamics may vary with tumor type and microenvironmental composition, these results underscore the value of CEUS as a real-time feedback tool for assessing vascular status during cavitation-based therapies. Importantly, the observed pressure-dependent recovery kinetics has direct implications for treatment design when leveraging cavitation therapy. These findings suggesting that if repeated cavitation exposures are desired, allowing at least 15 minutes between treatments appears necessary in preclinical models to ensure that microbubbles, and possibly any co-delivered therapeutic payloads, can re-enter the tumor vasculature. This point is often overlooked, as many treatment schemes implicitly assume that microbubbles readily recirculate into the tumor, yet our data suggest that TTPL can substantially limit re-entry above certain acoustic pressures. This consideration is relevant even for infusion-based strategies, where systemic microbubble concentrations may remain high but effective intratumoral delivery may still be impaired by TTPL, but would need to be evaluated directly.

Our PCD results aimed to characterize microbubble activity and were able to conclude that spectral components consistent with what is often referred to as inertial cavitation were present in our moderate and high-pressure conditions. With the low-pressure condition, although the 1.25 MPa pressure in the tumor center possibly entered the inertial cavitation regime according to previously studied cavitation thresholds [35], the very small area around the focus which experienced this pressure was possibly below the detection threshold of our PCD system. Our PCD results in the moderate and high-pressure conditions were comparable, despite the differences observed in perfusion evaluations. This finding supports previous assertions that more complex cavitation activity can occur during inertial cavitation other than the elevation of broadband noise [36]. Although PCD measurements remain useful for confirming if certain levels of cavitation activity are present during treatment, cavitation-induced TTPL is most accurately captured using CEUS combined with image-based quantification methods like MIP-TAC.

Although many works have focused on cavitation treatments as a means for improving therapeutic outcomes, TTPL and its recovery dynamics could be leveraged as a diagnostic tool. Based on

findings in this study, sonications with pressures around 1 MPa (mechanical index of 0.9-1) could be coupled with microbubble injections to induce significant and reversible TTPL if a tumor is present. However, TTPL has not been studied in humans where differing tumor properties exist and it is possible that reversible TTPL is not feasible, and further characterization of TTPL in humans would be necessary for utilizing this technique. If preclinical findings match those in humans, by performing standard CEUS imaging within 5 minutes of treatment, suspect lesions could be visualized as areas of reduced signal (perfusion loss) to assist in characterizing them as tumors. The tumor-specific nature of this phenomenon would allow for the entire organ to be sonicated, rather than requiring advanced knowledge of lesion locations to be targeted and allow for possible detection of satellite lesions during treatment planning. Unlike conventional imaging biomarkers, TTPL may be observed in real time with low MI nonlinear imaging in CEUS, possibly allowing immediate diagnostic confirmation. Since ultrasound systems and contrast agents are portable and widely available, this technology has strong potential for deployment in resource-limited and remote settings, thereby helping to reduce healthcare disparities in cancer diagnosis. However, the response of different lesion types, particularly differences between benign and malignant lesions to TTPL pulses, has not been explored in human cancers and could provide necessary information about unique tumor characteristics alongside the phenomenon's specificity as a diagnostic measure. Further optimization of ultrasound parameters explored here could elicit a condition where significant TTPL occurs without significant effects on the tumor microenvironment, positioning it as a pivotal diagnostic tool.

### 5.4.2 *Cavitation-induced damage and tumor composition possibly influences resulting tumor blood flow changes*

Beyond the transient to semi-transient TTPL response shared amongst all conditions, cavitation-induced vascular damage likely also contributed to the pressure-dependent differences in tumor perfusion observed in this study. At the higher pressures, histological evidence of damage was detected in a subset of tumors (3 out of 5 at the high-pressure and 1 out of 5 at the moderate-pressure), and this damage was spatially localized, consistent with the <2 mm focal region of the therapeutic transducer where the much greater pressures were experienced in these conditions (4.1 MPa and 2.8 MPa respectively). Colocalization of stains indicating damage, specifically only Annexin V (indicating permeation of cellular membranes) but not CC3, was only observed in one

sample in the moderate-pressure group. However, in both these groups, observations were not seen in across all samples, possibly missed due to the small focal spot size and its exact location within the tumor. Despite this, the injury observed from stains in the higher-pressure samples may reflect localized mechanical damage from cavitating microbubbles or small-scale hemorrhage, but the definitive relation of these observations to cavitation treatments could not be made with the small sample size and staining panel employed in this study. However, samples in which damage was observed in the high-pressure condition also saw a reduction in tumor perfused areas by the hour timepoint from the MIP-TAC analysis. This suggests that the blood flow observations, particularly those in high-pressure condition, could possibly have been influenced by acute damage from the cavitation treatments, potentially reflecting vascular impairment and apoptosis associated with the initial stages of the ceramide pathway.

Several mechanisms proposed in previous studies could plausibly explain the phenomenon of TTPL observed in this study, but the exact pathway has still not been conclusively determined. One possible driver of this effect is platelet-driven thrombosis, as mechanical injury to the endothelium can expose basement membrane or tissue factor, which could rapidly induce local platelet accumulation. This hypothesis was supported by Hu et al [13] where TTPL was not induced when anti-thrombogenic agents were administered, indicating clot formation could be causing the sudden cessation of blood flow. Additionally, prothrombin time, or the time taken for fibrin clots to form, is approximately 9 to 12 seconds in mice, resulting from high levels of clotting factor V [37, 38]. This rapid time course would be feasible with the significant perfusion loss observed immediately after treatment (performed within 1 minute of sonication), but the rapid recovery dynamics observed and how they align with clearance of possible thrombus in mouse microcirculation would need to be investigated further. Pericyte-mediated vessel spasm has also been considered as a possible driver of TTPL induced by cavitation treatments. The nucleus of pericytes are mechanosensory, as these cells are designed to respond to hydrodynamic pressure and shear stress from fluid flow to regulate blood flow via contraction [39]. Previous works have shown that tumors lack properly functioning pericytes compared to surrounding parenchyma [40, 41] and could contribute to the tumor specificity of this effect. Endothelial injury resulting from cavitation treatments has also been linked to the ceramide pathway, resulting vascular dysfunction and initiating apoptosis and often coupled with radiation treatments [15, 42]. Endothelial cells

contain roughly twenty-fold higher levels of acid sphingomyelinase (aSMase) than most other cell types, which is a catalyst for ceramide generation [43]. Ultrasound cavitation treatments have been shown to elevate aSMase and ceramide, promoting endothelial cell death through membrane disruption [15, 44]. Increased ceramide staining has been observed as early as one hour after microbubble destruction in vitro [42] and increased ceramide levels could have contributed to apoptosis and reduced perfusion observed at the hour point in this study in the high-pressure condition. However, this pathway may become more prominent beyond the one-hour window examined here but is unlikely to have resulted in the rapid cessation of tumor blood immediately following treatment observed in this work.

Cavitation treatments have been linked to a variety of effects on the tumor microenvironment beyond those listed above, but these effects have not been well defined in relation to their possible contribution to vascular changes. Changes to tumor interstitial fluid pressure resulting from microbubble cavitation, likely driven by poration of endothelial cells or widening of cell-cell junctions, has also been observed with parameters inducing TTPL [11, 45, 46], and this rapid pressure adjustment could contribute to blood flow changes. Although unable to answer the mechanistic question directly in this study, a greater understanding of the temporal dynamics and alterations of the tumor microenvironment derived from this work further understanding of this phenomenon, and future studies could employ ultrasound parameters known to induce TTPL defined here to evaluate mechanism thoroughly.

### 5.4.3 *Limitations*

This study has several limitations that should be considered when interpreting the findings. First, all experiments were performed in a subcutaneous model using a single tumor type, and perfusion dynamics may differ in tumors and the magnitude of TTPL might differ under the same acoustic conditions. Because our goal was to isolate the effects of a short and single cavitation exposure (one second), we did not evaluate how multiple treatments might alter TTPL or recovery kinetics. We also did not assess long-term vascular effects, which could influence the optimal selection of acoustic parameters if more permanent blood flow effects were desired. Additionally, although pulse length and pulse repetition frequency likely play important roles in modulating vascular responses, the scope of in vivo experimentation limited our ability to explore a broader parameter

space. As previously mentioned, the small focal spot of the therapeutic transducer also produced non-uniform pressure distributions across the tumor, raising the possibility that side-lobe pressures contributed to the observed effects and that lower pressures than those tested may be sufficient to induce similar TTPL responses. We were not able to observe uniform histological findings across all samples in each group, challenged by the small focal spot size as demonstrated by **Fig. 5.2C**, the small central region of the tumor which was evaluated, and limited sample size. Only CEUS was used to evaluate blood flow changes as presence of the agent is necessary for subsequent cavitation treatments, but we were unable to evaluate vascular changes of individual vessels, and other blood flow evaluation techniques could provide complementary information to our results. Finally, translation to human tumors which differ substantially in scale, vascular organization, and mechanical properties, may yield different perfusion outcomes, and require further investigation in clinical settings.

## 5.5 CONCLUSION

This work demonstrates that acoustic pressure plays a central role in determining both the extent and duration of cavitation-induced tumor blood flow changes, or TTPL. By acquiring CEUS data at different time points following treatment and utilizing our quantitative MIP-TAC analysis, we characterized the recovery dynamics of this phenomenon over a time course not thoroughly examined, providing new insight into the temporal and spatial dynamics of cavitation-mediated TTPL. Elevated broadband energy confirmed the presence of inertial cavitation in our moderate and high-pressure conditions, indicating that the observed vascular responses were driven by mechanical forces generated by oscillating and collapsing microbubbles. Our findings also suggest that long pulses (> 100 cycles) with acoustic pressures beyond a certain threshold (4 MPa peak negative pressure) in the presence of microbubble contrast agents can induce mechanical damage and possibly induce more permanent tumor blood flow changes. Importantly, these results offer possible guidance for optimizing cavitation-based treatment protocols, suggesting that repeated exposures above 1 MPa (mechanical index of 0.9-1.0) must account for TTPL, as this effect can substantially limit microbubble reentry and thereby reduce the effective dose delivered to the tumor in treatments after the first sonication. Collectively, this work advances our understanding of how acoustic conditions induce TTPL and informs the design of more effective therapeutic ultrasound-mediated cavitation strategies.

## 5.6 ACKNOWLEDGEMENTS

Research was supported from the National Institute of Biomedical Imaging and Bioengineering of the National Institutes of Health under award number R01EB032655. SonoVue was generously supplied by Bracco (Bracco Suisse SA, Geneva, Switzerland) and we acknowledge the technical support of Dr. Samir Cherkaoui. We also acknowledge the support of Dr. Thanasis Loupas with discussions on QLAB super-resolution. We also thank Jenifer Mendez-Pacheco and Kaleb Vuong for their assistance in animal care and technical support.

## 5.7 REFERENCES

[1] M.A. Averkiou, M.F. Bruce, J.E. Powers, P.S. Sheeran, P.N. Burns, Imaging Methods for Ultrasound Contrast Agents, Ultrasound in medicine & biology, 46 (2020) 498-517.
[2] A. El Kaffas, A. Hoogi, J. Zhou, I. Durot, H. Wang, J. Rosenberg, A. Tseng, H. Sagreiya, A. Akhbardeh, D.L. Rubin, A. Kamaya, D. Hristov, J.K. Willmann, Spatial Characterization of Tumor Perfusion Properties from 3D DCE-US Perfusion Maps are Early Predictors of Cancer Treatment Response, Scientific reports, 10 (2020) 6996.
[3] D. Wildner, L. Pfeifer, R.S. Goertz, T. Bernatik, J. Sturm, M.F. Neurath, D. Strobel, Dynamic contrast-enhanced ultrasound (DCE-US) for the characterization of hepatocellular carcinoma and cholangiocellular carcinoma, Ultraschall in der Medizin (Stuttgart, Germany : 1980), 35 (2014) 522-527.
[4] K. Kooiman, S. Roovers, S.A.G. Langeveld, R.T. Kleven, H. Dewitte, M.A. O'Reilly, J.M. Escoffre, A. Bouakaz, M.D. Verweij, K. Hynynen, I. Lentacker, E. Stride, C.K. Holland, Ultrasound-Responsive Cavitation Nuclei for Therapy and Drug Delivery, Ultrasound in medicine & biology, 46 (2020) 1296-1325.
[5] S. Liu, Y. Zhang, Y. Liu, W. Wang, S. Gao, W. Yuan, Z. Sun, L. Liu, C. Wang, Ultrasound-targeted microbubble destruction remodels tumour microenvironment to improve immunotherapeutic effect, British journal of cancer, 128 (2023) 715-725.
[6] F. Padilla, J. Brenner, F. Prada, A.L. Klibanov, Theranostics in the vasculature: bioeffects of ultrasound and microbubbles to induce vascular shutdown, Theranostics, 13 (2023) 4079-4101.
[7] D. Dalecki, WFUMB Safety Symposium on Echo-Contrast Agents: bioeffects of ultrasound contrast agents in vivo, Ultrasound in medicine & biology, 33 (2007) 205-213.
[8] J. He, Z. Liu, X. Zhu, H. Xia, H. Gao, J. Lu, Ultrasonic Microbubble Cavitation Enhanced Tissue Permeability and Drug Diffusion in Solid Tumor Therapy, Pharmaceutics, 14 (2022).
[9] S.B. Keller, M.A. Averkiou, The Role of Ultrasound in Modulating Interstitial Fluid Pressure in Solid Tumors for Improved Drug Delivery, Bioconjugate chemistry, 33 (2022) 1049-1056.
[10] N. McDannold, Y. Zhang, N. Vykhodtseva, Nonthermal ablation in the rat brain using focused ultrasound and an ultrasound contrast agent: long-term effects, Journal of neurosurgery, 125 (2016) 1539-1548.
[11] C. Krolak, L. De Koninck, S. Gu, Y.N. Wang, J.E. Powers, M. Averkiou, Ultrasound cavitation therapy: inducing tumor drug delivery and blood flow changes with clinical ultrasound tools, Journal of controlled release : official journal of the Controlled Release Society, 393 (2026) 114748.
[12] J. Wang, Z. Zhao, S. Shen, C. Zhang, S. Guo, Y. Lu, Y. Chen, W. Liao, Y. Liao, J. Bin, Selective depletion of tumor neovasculature by microbubble destruction with appropriate ultrasound pressure, International journal of cancer, 137 (2015) 2478-2491.
[13] X. Hu, A. Kheirolomoom, L.M. Mahakian, J.R. Beegle, D.E. Kruse, K.S. Lam, K.W. Ferrara, Insonation of targeted microbubbles produces regions of reduced blood flow within tumor vasculature, Investigative radiology, 47 (2012) 398-405.
[14] X. Zhao, C. Pellow, D.E. Goertz, Intravital imaging and cavitation monitoring of antivascular ultrasound in tumor microvasculature, Theranostics, 13 (2023) 250-266.

[15] A. El Kaffas, M.J. Gangeh, G. Farhat, W.T. Tran, A. Hashim, A. Giles, G.J. Czarnota, Tumour Vascular Shutdown and Cell Death Following Ultrasound-Microbubble Enhanced Radiation Therapy, Theranostics, 8 (2018) 314-327.
[16] Y.J. Ho, T.C. Wang, C.H. Fan, C.K. Yeh, Spatially Uniform Tumor Treatment and Drug Penetration by Regulating Ultrasound with Microbubbles, ACS Appl Mater Interfaces, 10 (2018) 17784-17791.
[17] P. Huang, Y. Zhang, J. Chen, W. Shentu, Y. Sun, Z. Yang, T. Liang, S. Chen, Z. Pu, Enhanced antitumor efficacy of ultrasonic cavitation with up-sized microbubbles in pancreatic cancer, Oncotarget, 6 (2015) 20241-20251.
[18] M. Todorova, V. Agache, O. Mortazavi, B. Chen, R. Karshafian, K. Hynynen, S. Man, R.S. Kerbel, D.E. Goertz, Antitumor effects of combining metronomic chemotherapy with the antivascular action of ultrasound stimulated microbubbles, International journal of cancer, 132 (2013) 2956-2966.
[19] C. Chien Ting, B.I. Raju, T. Shevchenko, A.L. Klibanov, Control and reversal of tumor growth by ultrasound activated microbubbles, in: 2009 IEEE International Ultrasonics Symposium, 2009, pp. 77-80.
[20] Z. Liu, S. Gao, Y. Zhao, P. Li, J. Liu, P. Li, K. Tan, F. Xie, Disruption of tumor neovasculature by microbubble enhanced ultrasound: a potential new physical therapy of anti-angiogenesis, Ultrasound in medicine & biology, 38 (2012) 253-261.
[21] R. Anbarafshan, C. Pellow, K. Kiezun, H. Leong, D.E. Goertz, In vivo high-speed microscopy of microbubbles in the chorioallantoic membrane model, Theranostics, 14 (2024) 1794-1814.
[22] C.W. Burke, A.L. Klibanov, J.P. Sheehan, R.J. Price, Inhibition of glioma growth by microbubble activation in a subcutaneous model using low duty cycle ultrasound without significant heating, Journal of neurosurgery, 114 (2011) 1654-1661.
[23] A. Daecher, M. Stanczak, J.B. Liu, J. Zhang, S. Du, F. Forsberg, D.B. Leeper, J.R. Eisenbrey, Localized microbubble cavitation-based antivascular therapy for improving HCC treatment response to radiotherapy, Cancer letters, 411 (2017) 100-105.
[24] D.E. Goertz, M. Todorova, O. Mortazavi, V. Agache, B. Chen, R. Karshafian, K. Hynynen, Antitumor effects of combining docetaxel (taxotere) with the antivascular action of ultrasound stimulated microbubbles, PloS one, 7 (2012) e52307.
[25] S. Bulner, A. Prodeus, J. Gariepy, K. Hynynen, D.E. Goertz, Enhancing Checkpoint Inhibitor Therapy with Ultrasound Stimulated Microbubbles, Ultrasound in medicine & biology, 45 (2019) 500-512.
[26] S.B. Keller, D. Suo, Y.N. Wang, H. Kenerson, R.S. Yeung, M.A. Averkiou, Image-Guided Treatment of Primary Liver Cancer in Mice Leads to Vascular Disruption and Increased Drug Penetration, Frontiers in pharmacology, 11 (2020) 584344.
[27] Y. He, M. Yu, J. Wang, F. Xi, J. Zhong, Y. Yang, H. Jin, J. Liu, Improving the Therapeutic Effect of Ultrasound Combined With Microbubbles on Muscular Tumor Xenografts With Appropriate Acoustic Pressure, Frontiers in pharmacology, Volume 11 - 2020 (2020).
[28] R.G. Barr, P. Huang, Y. Luo, X. Xie, R. Zheng, K. Yan, X. Jing, Y. Luo, H. Xu, X. Fei, J.M. Lee, Contrast-enhanced ultrasound imaging of the liver: a review of the clinical evidence for SonoVue and Sonazoid, Abdominal radiology (New York), 45 (2020) 3779-3788.
[29] A. Bouakaz, P.J.A. Frinking, N. de Jong, N. Bom, Noninvasive measurement of the hydrostatic pressure in a fluid-filled cavity based on the disappearance time of micrometer-sized free gas bubbles, Ultrasound in medicine & biology, 25 (1999) 1407-1415.
[30] D. Fukumura, R.K. Jain, Tumor microvasculature and microenvironment: targets for anti-angiogenesis and normalization, Microvascular research, 74 (2007) 72-84.
[31] J.A. Nagy, S.H. Chang, S.C. Shih, A.M. Dvorak, H.F. Dvorak, Heterogeneity of the tumor vasculature, Seminars in thrombosis and hemostasis, 36 (2010) 321-331.
[32] K. Welsher, S.P. Sherlock, H. Dai, Deep-tissue anatomical imaging of mice using carbon nanotube fluorophores in the second near-infrared window, Proceedings of the National Academy of Sciences of the United States of America, 108 (2011) 8943-8948.
[33] L.H. De Koninck, K.S. Vuong, S. Shin, J.E. Powers, M.A. Averkiou, Delivery of Cavitation Therapy With a Modified Clinical Scanner: In Vitro Evaluation, IEEE transactions on ultrasonics, ferroelectrics, and frequency control, 72 (2025) 351-361.
[34] X. Zhao, A. Wright, D.E. Goertz, An optical and acoustic investigation of microbubble cavitation in small channels under therapeutic ultrasound conditions, Ultrasonics sonochemistry, 93 (2023) 106291.
[35] S.B. Keller, P.S. Sheeran, M.A. Averkiou, Cavitation Therapy Monitoring of Commercial Microbubbles With a Clinical Scanner, IEEE transactions on ultrasonics, ferroelectrics, and frequency control, 68 (2021) 1144-1154.

[36] Q. Wu, M. Gray, C.A.B. Smith, L. Bau, R.O. Cleveland, C. Coussios, E. Stride, Challenges in classifying cavitation: Correlating high-speed optical imaging and passive acoustic mapping of cavitation dynamics, The Journal of the Acoustical Society of America, 156 (2024) 3608-3620.
[37] J.A. De Pablo-Moreno, A. Liras, L. Revuelta, Standardization of Coagulation Factor V Reference Intervals, Prothrombin Time, and Activated Partial Thromboplastin Time in Mice for Use in Factor V Deficiency Pathological Models, Frontiers in veterinary science, 9 (2022) 846216.
[38] L.L. Peters, E.M. Cheever, H.R. Ellis, P.A. Magnani, K.L. Svenson, R. Von Smith, M.A. Bogue, Large-scale, high-throughput screening for coagulation and hematologic phenotypes in mice, Physiological genomics, 11 (2002) 185-193.
[39] C.A. Dessalles, A. Babataheri, A.I. Barakat, Pericyte mechanics and mechanobiology, Journal of Cell Science, 134 (2021).
[40] M. Chen, X. Lei, C. Shi, M. Huang, X. Li, B. Wu, Z. Li, W. Han, B. Du, J. Hu, Q. Nie, W. Mai, N. Ma, N. Xu, X. Zhang, C. Fan, A. Hong, M. Xia, L. Luo, A. Ma, H. Li, Q. Yu, H. Chen, D. Zhang, W. Ye, Pericyte-targeting prodrug overcomes tumor resistance to vascular disrupting agents, The Journal of clinical investigation, 127 (2017) 3689-3701.
[41] S. Morikawa, P. Baluk, T. Kaidoh, A. Haskell, R.K. Jain, D.M. McDonald, Abnormalities in pericytes on blood vessels and endothelial sprouts in tumors, The American journal of pathology, 160 (2002) 985-1000.
[42] G.J. Czarnota, R. Karshafian, P.N. Burns, S. Wong, A. Al Mahrouki, J.W. Lee, A. Caissie, W. Tran, C. Kim, M. Furukawa, E. Wong, A. Giles, Tumor radiation response enhancement by acoustical stimulation of the vasculature, Proceedings of the National Academy of Sciences of the United States of America, 109 (2012) E2033-2041.
[43] M. Garcia-Barros, F. Paris, C. Cordon-Cardo, D. Lyden, S. Rafii, A. Haimovitz-Friedman, Z. Fuks, R. Kolesnick, Tumor response to radiotherapy regulated by endothelial cell apoptosis, Science (New York, N.Y.), 300 (2003) 1155-1159.
[44] J.T. Nofiele, R. Karshafian, M. Furukawa, A. Al Mahrouki, A. Giles, S. Wong, G.J. Czarnota, Ultrasound-activated microbubble cancer therapy: ceramide production leading to enhanced radiation effect in vitro, Technology in cancer research & treatment, 12 (2013) 53-60.
[45] Y. He, Y. Feng, D. Qiu, M. Lin, H. Jin, Z. Hu, X. Huang, S. Ma, Y. He, M. Lai, W. Jin, J. Liu, Regulation of IFP in solid tumours through acoustic pressure to enhance infiltration of nanoparticles of various sizes, Journal of drug targeting, 32 (2024) 964-976.
[46] F. Xi, Y. Feng, Q. Chen, L. Chen, J. Liu, Microbubbles Ultrasonic Cavitation Regulates Tumor Interstitial Fluid Pressure and Enhances Sonodynamic Therapy, Frontiers in oncology, 12 (2022) 852454.

# Chapter 6. FUTURE/ON-GOING WORK: ULTRASOUND CAVITATION TREATMENTS AND IMMUNOTHERAPY

**Abstract**

Structural abnormalities and immunosuppressive features within the tumor microenvironment are thought to contribute to the limited effectiveness of immune checkpoint inhibitors (ICI) in liver cancers. However, ultrasound and microbubble cavitation treatments have emerged as a promising approach to enhance immunotherapy delivery and potency or even modulate the immune environment on their own. In this chapter, we describe on-going work investigating whether cavitation-induced transient tumor perfusion loss (TTPL) elicits sustained immune-modulating effects, and whether tumor susceptibility to TTPL correlates with responsiveness to ICIs. To capture the phenotypic heterogeneity of liver malignancies and a more analogous immune environment to human liver cancer, we used a transgenic mouse model with underlying steatosis that develops both hepatocellular carcinoma (HCC) and intrahepatic cholangiocarcinoma (ICC) in this study. We describe on-going work evaluating the potential antitumor-enhancing effects of cavitation in combination with standard-of-care ICIs for liver cancer.

## 6.1 INTRODUCTION

Hepatocellular carcinoma (HCC) presents a substantial and growing burden to global healthcare systems. For patients with advanced disease where localized therapies are no longer feasible and the risk of metastasis is high, the current clinical care utilizes the administration of immune checkpoint inhibitors (ICIs) (1). ICIs exert their therapeutic activity by disrupting interactions between checkpoint receptors and ligands on circulating leukocytes which bind to them, thereby preventing transmission of inhibitory signals that suppress T-cell activation. This blockade restores cytotoxic T-cell function and enhances antitumor immune responses. In particular, the combination of tremelimumab (anti-CTLA-4) and durvalumab (anti-PD-L1) has demonstrated clinically meaningful antitumor efficacy in trials involving patients with unresectable hepatocellular carcinoma (2). However, clinical success remains inconsistent, with reported response rates to anti-PD-1/PD-L1 therapies ranging from 10% to 30% (3, 4). These limitations underscore the need for strategies that can enhance immunotherapy efficacy by overcoming barriers resulting from the tumor microenvironment (TME).

The TME not only restricts drug uptake and accumulation through its abnormal vasculature and dense extracellular matrix but also actively suppresses antitumor immunity. Induction of immunosuppressive cytokines and regulatory T-cells blunt the effectiveness of ICIs (5-7). Transport of therapeutic molecules such as ICIs into tumor interstitium depends on convective flow (8, 9), but the combination of increased vascular permeability, poor lymphatic drainage, and chronic inflammation leads to elevated interstitial fluid levels and high interstitial fluid pressure (IFP) with little to no convective flow in the interstitium (10, 11). These physical abnormalities and immunosuppressive barriers present in the TME hinder the efficacy of ICIs in solid tumors like HCC.

Applications of ultrasound in the presence of microbubbles have emerged as a promising strategy to enhance the delivery and efficacy of immunotherapies. Cavitation, or the rapid oscillation and collapse of microbubbles, generates physical forces reported to permeate cell membranes and improve drug penetration (12, 13). Beyond enhancing delivery, cavitation may directly stimulate antitumor immunity by promoting the release of structurally intact tumor-associated peptides, potentiate immunostimulatory or chemotactic signaling pathways, or facilitate intracellular

delivery of immune-modulating factors (14-16). Cavitation has also been shown to reduce tumor IFP, which may further improve convective transport and penetration of ICIs (17, 18). These findings highlight the potential for ultrasound cavitation treatments to synergize with ICIs through both physical changes to the TME and priming of the immune system.

Under specific acoustic conditions, cavitation treatments can also induce marked alterations in tumor perfusion. This rapid, pressure-dependent reduction in tumor blood flow following exposure to cavitation treatments has been observed in multiple therapeutic ultrasound studies, often referred to as vascular shutdown or transient tumor perfusion loss (TTPL) (18-20). This effect is thought to arise from the heightened vulnerability of tumor vasculature to the mechanical stresses generated during cavitation, supported by its tumor-specific nature (21). Ultrasound and microbubble combinations have therefore been explored as "anti-vascular" agents capable of disrupting tumor blood flow, with potential downstream effects on immune modulation. These include enhanced trafficking or penetration of ICIs or activated T cells into tumor tissue, as well as improved antigen-presenting cell maturation (22, 23). However, the magnitude and duration of TTPL is strongly dependent on ultrasound parameters used, where a wide range of acoustic conditions are employed and vascular dynamics are often not characterized with simultaneous imaging. Variability in TTPL responses may help explain the inconsistent immune responses reported for cavitation-based therapies. While some studies have documented augmented antitumor immunity despite immediate vascular shutdown (23, 24), others have observed minimal immune cell infiltration (25, 26), potentially attributed to a more sustained impairment of tumor perfusion.

Motivated the current barrier in effective ICI treatments of HCC, the present study investigates the potential immunological benefits of ultrasound-mediated cavitation in combination with ICI therapy. Specifically, we sought to determine whether immune-modulating effects persist under cavitation conditions that induce TTPL and to evaluate whether the susceptibility of tumors to TTPL correlates with their responsiveness to ICIs. To capture the heterogeneity of liver tumor phenotypes, we used a transgenic mouse model of liver cancer with underlying steatosis that develops both HCC and intrahepatic cholangiocarcinoma (ICC). This work also uniquely studied the effects of a single ultrasound pulse, which has not previously been explored in cavitation treatments. Through administration of anti-PD-L1 and anti-CTLA-4 antibodies, we assessed

whether cavitation treatments enhanced leukocyte infiltration into tumors, thereby indicating activation of antitumor immune responses.

## 6.1 Materials and Methods

### 6.1.1 *Mouse model preparation*

All animal protocols performed were approved by the Institutional Animal Care and Use Committee (IACUC) at the University of Washington, Seattle. Utilizing mice purchased from Jackson Labs (Bar Harbor, ME), 8-week-old Pten-floxed ($Pten^{fl/fl}$) mice (B6.129S4-Pten<tm1Hwu>/J, strain 006440) were bred with albumin (Alb)-Cre transgenic mice (B6.Cg-Speer6-ps1<Tg(Alb-cre)21Mgn>/J, strain 003574) to derive Ptenfl/fl;AlbCre (also known as Pten-/-, or Pten-null) mice. In addition to liver steatosis, at approximately 40 weeks old, Pten-null mice develop tumors that are 5-10 mm in diameter (20, 27, 28). Starting from 36 weeks of age, mice were imaged weekly with B-mode ultrasound imaging to track tumor growth. Once tumors reached 6 mm in diameter, 32 mice were randomly separated into one of the four treatment groups (n = 6 per group).

### 6.1.2 *Drugs and contrast agent*

Immune checkpoint inhibitors were administered via intraperitoneal injection 3 times a week for 3 consecutive weeks for a total of 9 injections. Injection volume was fixed at 250 µL. Mice in groups receiving the ICI were given a combination of anti-PD-L1 (200 µg per mouse, InVivoMAb anti-mouse PD-L1, B7-H1) and anti-CTLA-4 (100 µg per mouse, InVivoMAb anti-mouse CTLA-4, CD152) on day 1 of treatment. For all subsequent ICI administration, only anti-PD-L1 was given, and all ICI drug administrations were diluted to 250 uL in 0.9% sterile saline. Mice in control and ultrasound cavitation only groups received only 0.9% sterile saline for all injections.

Lumason microbubbles (Bracco Suisse SA, Geneva, Switzerland), marketed as SonoVue outside the United States, were selected for this study because they are clinically approved for characterization of focal liver lesions in the United States as well as in numerous countries across Europe and Asia (29). A microbubble dose of 50 µL per injection was used, consistent with prior reports as it provides adequate imaging signal while minimizing acoustic shadowing (18, 20). This

microbubble dosing scheme was used for cavitation treatments and all contrast-enhanced ultrasound (CEUS) scans.

### 6.1.3 *Ultrasound parameters*

An in-house single-element transducer (0.6 MHz, 5.0 cm diameter, 11 cm focal length) driven by an RF amplifier (2200L, Electronics and Innovation, Rochester, NY, USA) was used to enable precise control of acoustic parameters. A single 10,000 cycle pulse was generated on an arbitrary function generator (AFG3102C, Tektronix, Beaverton, OR, USA) at 0.6 MHz for the cavitation treatment pulse, with an approximate peak negative pressure of 1 MPa. An axial distance of 80 mm was selected as the treatment location to maximize the size of the treatment volume to promote a uniform acoustic pressure throughout the tumor. The measured acoustic field from a hydrophone in a water tank system and a representative 6 mm diameter tumor placed at 80 mm are shown in **Figure 6.1A**.

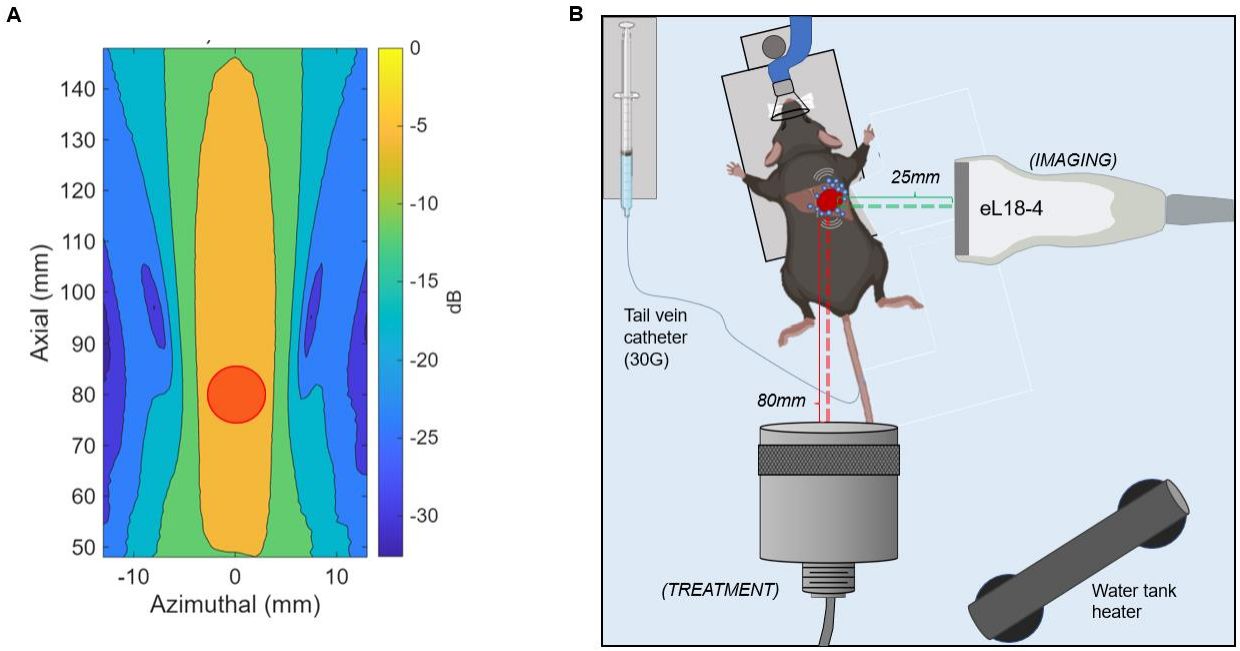


**Figure 6.1**: Visualization of ultrasound field and alignment in cavitation treatments. (A) The measured 2D field of the single element transducer in log scale. A representative 6 mm diameter tumor is overlaid at the 80 mm location. (B) Schematic of a top-down view of the heated, degassed water tank experimental setup. Co-alignment of the treatment and imaging probes to red circle, representing the orthotopic tumor in the liver of the mouse.

### 6.1.4 *Experimental setup and treatment procedure*

To account for the alignment of several probes to the intrahepatic tumor and allow for simultaneous treatment and imaging, a heated (37°C) and degassed water tank setup was utilized (**Figure 6.1B**). The single element transducer powered by a function generator and amplifier as described above was used for administering the cavitation treatments. A Philips eL18-4 ultrasound probe on the EPIQ scanner (Philips Healthcare, Bothell, WA, USA) was used to guide the procedure. Before beginning the experiments, both transducers were aligned to the same 3-D location using a thin acrylic disk. First, the single element transducer was positioned 80 mm from the target using a pulse-echo technique. Then, the eL18-4 was aligned 2.5 cm from the target using imaging, and an image of the location of the center of the disc was recorded prior to its removal. Mice were induced at 3% isoflurane and maintained at 1.5–2% isoflurane and fitted with a 30G tail-vein catheter. Hair on the abdomen was shaved and depilated with hair-removal cream (Veet) to permit ultrasound transmission to the liver. Mice were secured to a custom restraining board, partially submerged in the water tank, and positioned so that the tumor center aligned with the previously recorded target location on the eL18-4 image.

Mice were randomly divided into four groups (n = 6 per group), as depicted in **Table 6.1**. The experimental timeline is summarized in **Figure 6.2**. All mice received 250 µL intraperitoneal injections of either ICI or saline 3 times a week for 3 weeks following enrollment. When CEUS imaging was performed as outlined on the experimental timeline, of a bolus of microbubbles was delivered while the tumor was continuously scanned with CEUS (amplitude modulation, 4.1 MHz, 4 cycles, mechanical index = 0.06) to establish tumor vascularity. For mice in the control or ICI only groups, they exclusively received CEUS scans at enrollment (week 1) and endpoint (week 4). On these days, sequential 1 mm B-mode images were also collected for the entire liver to allow volumetric reconstruction of the lesion from user drawn regions of interest. For mice receiving cavitation treatments, they received these two CEUS scans alongside a cavitation treatment regime on week 1 and 2 of treatment. When performing a pre-treatment CEUS scan for mice enrolled in a group receiving cavitation treatments, a time-intensity curve was formed from a freeform polygon region of interest (ROI) of the tumor to determine when peak microbubble concentration occurred. Cavitation treatments were then performed with a new microbubble injection and immediately followed by a standard CEUS scan on another bolus of microbubbles within 2

minutes of treatment. This process was repeated three times, each spaced 30 minutes apart to allow for tumor reperfusion as estimated in our previous work. After each CEUS imaging or cavitation session, mice were gently weaned off anesthesia while active heat support was supplied. Three days after endpoint CEUS on week 4, mice were euthanized via CO2 overdose with secondary methods, and all imaged liver tumors were harvested and fixed in 10% formalin for histological evaluations.

| **Treatment Group** (*n = 6 per group*) |
|---|
| 1) Control (saline only) |
| 2) Immunotherapy only (anti-PD-L1 & CTLA-4) |
| 3) Ultrasound cavitation treatment only |
| 4) Ultrasound cavitation treatment + immunotherapy |

**Table 6.1**: Experimental groups used in this study.

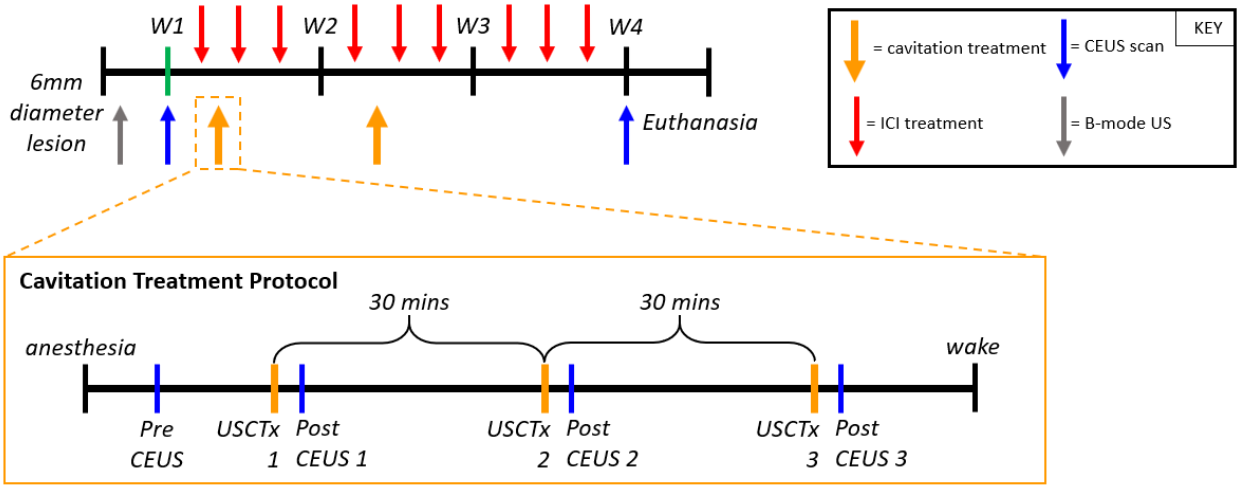


**Figure 6.2**: Experimental timeline. After recruitment, mice received intraperitoneal injections of immune checkpoint inhibitors (ICI) therapy or saline for 3 weeks, represented by the red arrows. Timing of cavitation treatments, contrast-enhanced ultrasound scans (CEUS), and B-mode imaging are shown with the orange, blue and grey arrows respectively. The procedures performed during cavitation treatments are shown in the orange subpanel. Weeks are abbreviated to W, and ultrasound is abbreviated to US.

## 6.2 CURRENT PROGRESS

All mouse experiments have recently been completed (April 2026), with analysis pending. The following provides insights and initial thoughts regarding the recently collected data.

Tumor size and overall tumor burden were evaluated. Good agreement was found between tumor sizes determined with ultrasound imaging and the approximate size of the excised lesion. Liver volume was calculated from B-mode images of the tumor taken in 1 mm intervals to account for irregularities in lesion shape. Percent change in primary tumor volume by group is shown in **Figure 6.3**, where it appears that mice in the cavitation conditions saw a reduction in tumor growth. With overall tumor burden being similar across all mice, this could possibly indicate benefits associated with targeted. However, size changes are not entirely representative of response, and vascular and immune-based differences have yet to be established.

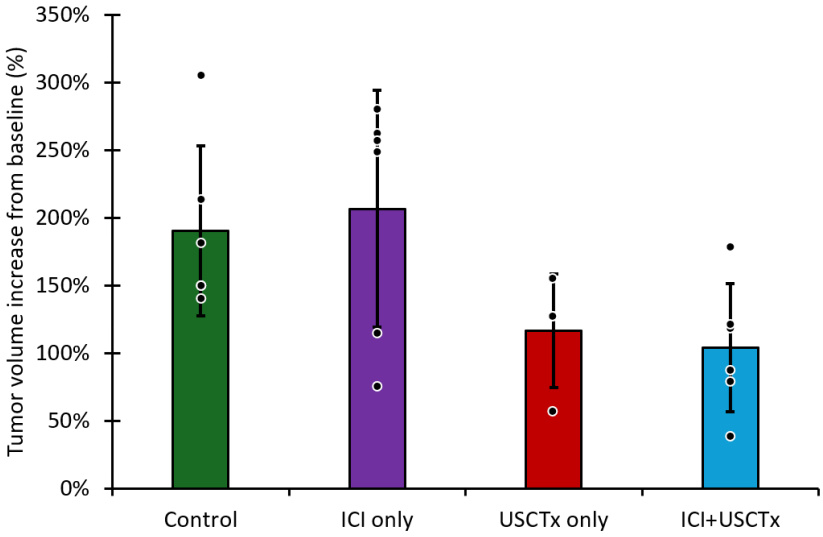


**Figure 6.3**: Changes to primary tumor volume from recruitment by condition. Average and standard deviation for each group is displayed.

CEUS images were processed offline following collect. We applied our custom respiratory-gating algorithm to exclude frames affected by out-of-plane respiratory motion and then utilized Philips QLAB super-resolution platform to apply maximum-intensity projection (MIP) to the remaining frames. An example set of images collected before and immediately after cavitation treatments are shown in **Figure 6.4**. Subsequent analyses will quantitatively evaluate

the effects of TTPL, and possibly stratifying outcomes by tumor phenotype as tumor compositions have been suggested to be a source of variability in TTPL magnitude (30). In addition, we will investigate the impact of repeated cavitation treatments, including whether complete vascular recovery between sessions occurred and if this influences the magnitude of TTPL in subsequent treatments. Finally, differences in vascular response may be examined in relation to the composition of recruited immune cell populations, providing insight into how mechanical forces from microbubble cavitation on the tumor microenvironment shape downstream immunologic effects.

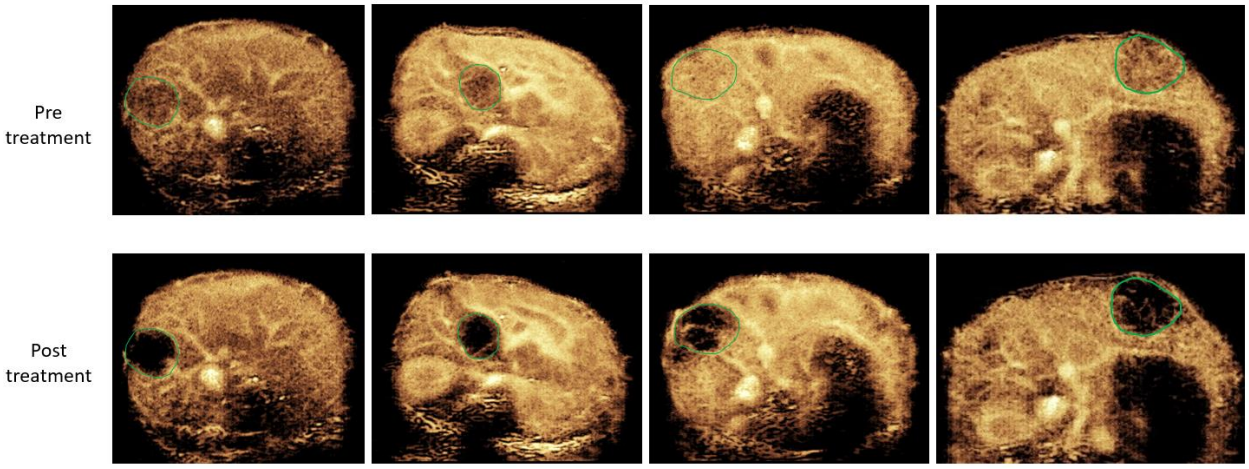


**Figure 6.4**: Representative images displaying perfusion loss in response to cavitation treatments. Maximum-intensity projection contrast-enhanced ultrasound images before and after cavitation treatment are shown, with the tumor highlighted by a green region of interest.

Immunological evaluations are currently underway. A pathologist will blindly evaluate H&E sections and HepPar1 stained sections to determine tumor phenotypes. Immunofluorescence will be used on fixed tissue sections to observe neutrophils, macrophages, and T-cell infiltration and distribution across conditions.

## 6.3 REFERENCES

1. van Bömmel F, Berg T, Lordick F. Immune checkpoint inhibition (ICI) in current systemic therapies for hepatocellular carcinoma (HCC). ESMO gastrointestinal oncology. 2023;1:27-39.
2. Abou-Alfa GK, Lau G, Kudo M, Chan SL, Kelley RK, Furuse J, et al. Tremelimumab plus Durvalumab in Unresectable Hepatocellular Carcinoma. NEJM evidence. 2022;1(8):EVIDoa2100070.
3. El-Khoueiry AB, Sangro B, Yau T, Crocenzi TS, Kudo M, Hsu C, et al. Nivolumab in patients with advanced hepatocellular carcinoma (CheckMate 040): an open-label, non-comparative, phase 1/2 dose escalation and expansion trial. Lancet (London, England). 2017;389(10088):2492-502.

4. Yu Y. Molecular classification and precision therapy of cancer: immune checkpoint inhibitors. Frontiers of medicine. 2018;12(2):229-35.
5. Gerlini G, Tun-Kyi A, Dudli C, Burg G, Pimpinelli N, Nestle FO. Metastatic melanoma secreted IL-10 down-regulates CD1 molecules on dendritic cells in metastatic tumor lesions. The American journal of pathology. 2004;165(6):1853-63.
6. Thomas DA, Massagué J. TGF-beta directly targets cytotoxic T cell functions during tumor evasion of immune surveillance. Cancer cell. 2005;8(5):369-80.
7. Turk MJ, Guevara-Patiño JA, Rizzuto GA, Engelhorn ME, Sakaguchi S, Houghton AN. Concomitant tumor immunity to a poorly immunogenic melanoma is prevented by regulatory T cells. The Journal of experimental medicine. 2004;200(6):771-82.
8. Jain RK. Transport of molecules in the tumor interstitium: a review. Cancer research. 1987;47(12):3039-51.
9. Munson JM, Shieh AC. Interstitial fluid flow in cancer: implications for disease progression and treatment. Cancer management and research. 2014;6:317-28.
10. Wagner M, Wiig H. Tumor Interstitial Fluid Formation, Characterization, and Clinical Implications. Frontiers in oncology. 2015;5:115.
11. Wiig H, Swartz MA. Interstitial fluid and lymph formation and transport: physiological regulation and roles in inflammation and cancer. Physiological reviews. 2012;92(3):1005-60.
12. Kooiman K, Roovers S, Langeveld SAG, Kleven RT, Dewitte H, O'Reilly MA, et al. Ultrasound-Responsive Cavitation Nuclei for Therapy and Drug Delivery. Ultrasound in medicine & biology. 2020;46(6):1296-325.
13. Stride E, Coussios C. Nucleation, mapping and control of cavitation for drug delivery. Nature Reviews Physics. 2019;1(8):495-509.
14. Escoffre JM, Deckers R, Bos C, Moonen C. Bubble-Assisted Ultrasound: Application in Immunotherapy and Vaccination. Advances in experimental medicine and biology. 2016;880:243-61.
15. Hu S, Zhang X, Unger M, Patties I, Melzer A, Landgraf L. Focused Ultrasound-Induced Cavitation Sensitizes Cancer Cells to Radiation Therapy and Hyperthermia. Cells. 2020;9(12):2595.
16. Unga J, Hashida M. Ultrasound induced cancer immunotherapy. Advanced drug delivery reviews. 2014;72:144-53.
17. He Y, Feng Y, Qiu D, Lin M, Jin H, Hu Z, et al. Regulation of IFP in solid tumours through acoustic pressure to enhance infiltration of nanoparticles of various sizes. Journal of drug targeting. 2024;32(8):964-76.
18. Krolak C, De Koninck L, Gu S, Wang YN, Powers JE, Averkiou M. Ultrasound cavitation therapy: inducing tumor drug delivery and blood flow changes with clinical ultrasound tools. Journal of controlled release : official journal of the Controlled Release Society. 2026;393:114748.
19. Hu X, Kheirolomoom A, Mahakian LM, Beegle JR, Kruse DE, Lam KS, et al. Insonation of targeted microbubbles produces regions of reduced blood flow within tumor vasculature. Investigative radiology. 2012;47(7):398-405.
20. Keller SB, Suo D, Wang YN, Kenerson H, Yeung RS, Averkiou MA. Image-Guided Treatment of Primary Liver Cancer in Mice Leads to Vascular Disruption and Increased Drug Penetration. Frontiers in pharmacology. 2020;11:584344.
21. Wang J, Zhao Z, Shen S, Zhang C, Guo S, Lu Y, et al. Selective depletion of tumor neovasculature by microbubble destruction with appropriate ultrasound pressure. International journal of cancer. 2015;137(10):2478-91.
22. Liu YT, Sun ZJ. Turning cold tumors into hot tumors by improving T-cell infiltration. Theranostics. 2021;11(11):5365-86.
23. Wu N, Cao Y, Liu Y, Zhou Y, He H, Tang R, et al. Low-intensity focused ultrasound targeted microbubble destruction reduces tumor blood supply and sensitizes anti-PD-L1 immunotherapy. Frontiers in bioengineering and biotechnology. 2023;11:1173381.
24. Hunt SJ, Gade T, Soulen MC, Pickup S, Sehgal CM. Antivascular ultrasound therapy: magnetic resonance imaging validation and activation of the immune response in murine melanoma. Journal of ultrasound in medicine : official journal of the American Institute of Ultrasound in Medicine. 2015;34(2):275-87.
25. Bulner S, Prodeus A, Gariepy J, Hynynen K, Goertz DE. Enhancing Checkpoint Inhibitor Therapy with Ultrasound Stimulated Microbubbles. Ultrasound in medicine & biology. 2019;45(2):500-12.
26. Li N, Tang J, Yang J, Zhu B, Wang X, Luo Y, et al. Tumor perfusion enhancement by ultrasound stimulated microbubbles potentiates PD-L1 blockade of MC38 colon cancer in mice. Cancer letters. 2021;498:121-9.

27. Horie Y, Suzuki A, Kataoka E, Sasaki T, Hamada K, Sasaki J, et al. Hepatocyte-specific Pten deficiency results in steatohepatitis and hepatocellular carcinomas. The Journal of clinical investigation. 2004;113(12):1774-83.
28. Kenerson HL, Yeh MM, Yeung RS. Tuberous sclerosis complex-1 deficiency attenuates diet-induced hepatic lipid accumulation. PloS one. 2011;6(3):e18075.
29. Barr RG, Huang P, Luo Y, Xie X, Zheng R, Yan K, et al. Contrast-enhanced ultrasound imaging of the liver: a review of the clinical evidence for SonoVue and Sonazoid. Abdominal radiology (New York). 2020;45(11):3779-88.
30. Padilla F, Brenner J, Prada F, Klibanov AL. Theranostics in the vasculature: bioeffects of ultrasound and microbubbles to induce vascular shutdown. Theranostics. 2023;13(12):4079-101.

# Chapter 7. CONCLUSIONS

## 7.1 SUMMARY

Hepatocellular carcinoma (HCC) presents a growing global health burden, motivating the advancement of more effective and accessible diagnostic and therapeutic strategies. This thesis developed a theranostic framework that leverages ultrasound and microbubble technologies to improve early detection, treatment monitoring, and therapeutic modulation of the tumor microenvironment. We first established quantitative contrast-enhanced ultrasound (CEUS) methodologies in both clinical and preclinical settings to enable robust perfusion assessment and then applied these tools to investigate ultrasound-mediated cavitation to alter tumor vascular function, reduce interstitial fluid pressure, and enhance drug delivery. Across these studies, we aimed to define how acoustic conditions influence cavitation-induced tumor vascular responses using clinically relevant tools to maximize translatability.

The first component of this work focused on developing rigorous CEUS imaging techniques for quantifying tumor and organ perfusion in HCCs. Currently, clinical adoption of quantitative CEUS has been limited by lack of standardization in microbubble delivery, imaging parameters, and techniques to correct for motion. As a result, they often lack sufficient repeatability to be reliably used in longitudinal studies such as treatment monitoring. In **Chapter 2**, through standardized probe fixation with an articulated arm, controlled bolus delivery, and custom respiratory gating and motion compensation algorithms, we have developed a comprehensive and repeatable imaging protocol and analysis for the evaluation of liver tumor perfusion. We demonstrated that bolus transit parameters derived from TIC analysis with our data collection and processing techniques exhibit greater repeatability across injections than those reported in most other clinical CEUS studies. Across a large patient study (n = 80), we evaluated inter-injection coefficients of variation (COV) for the four most commonly used blood-flow metrics in CEUS TIC analysis: rise time (*RT*), mean transit time (*MTT*), peak intensity (*PI*), and area under the curve (*AUC*). The average COV for *RT* and *MTT* were below 21%, whereas *PI* and *AUC* exhibited COVs below 40%, establishing useful thresholds for longitudinal studies utilizing these metrics to determine when true physiological changes have occurred. COVs for these metrics extracted directly from the TIC and from the curve fitted data were very similar, indicating the robustness of the data collection regime

and suggesting that curve fitting, which is not standardized in clinical evaluations, could be eliminated and direct bolus TIC metric calculations could be made. The standardized CEUS imaging method and analysis presented here yields highly repeatable perfusion metrics that may be sufficiently sensitive for assessing therapeutic response in longitudinal studies, and the techniques defined here could be adjusted to expand their application to other tumors in the future.

Utilizing our established scanning protocol, we extended CEUS quantification to HCC diagnosis in **Chapter 3** through quantification of metrics in the CEUS Liver Imaging and Reporting Data Systems (LI-RADS), the current clinical gold standard. Many previous attempts to quantify HCC blood flow with CEUS have been limited by the inability to capture late washout due to bubble destruction from 5-minute continuous imaging or excessive respiratory motion. To our knowledge, this work is the first time the CEUS LI-RADS scheme has been implemented quantitatively, marking a milestone for the computational assessments of clinical CEUS data. In our HCC patient data with confirmed LI-RADS LR-5 lesions, we quantitatively captured arterial phase hyperenhancement (APHE) using *RT* and washout using a relative degree of washout parameter. These two characteristic features of HCCs are the primary vascular features used in CEUS LI-RADS diagnosis and were present in all lesions captured with our quantitative tool. Importantly, we also quantified the washout of these lesions for the first time through *DW* and *rDW*, a tumor characteristic which was previously only evaluated qualitatively in CEUS LI-RADS. With parametric processing, we were able to visualize these perfusion-based parameters and manipulate regions of interest (ROI) synchronized across images. Through this quantitative parametric analysis, we aim to reduce subjectivity of ROI selection, assist in removing observer bias, and provide metrics to clinicians to potentially improve the sensitivity of CEUS LI-RADS. This work establishes a framework for algorithmic approaches to diagnosis, aiming to remove expertise-driven barriers from adoption and promote use of CEUS LI-RADS as a first line vascular diagnostic option.

The second component of the thesis evaluate cavitation-based cancer treatments using clinically available microbubbles and a modified clinical ultrasound system and assessed blood flow changes with our quantitative CEUS tools (**Chapters 2 and 3**). In **Chapter 4**, we evaluated two acoustic conditions generated by a clinical scanner and probe in acute studies of humanized HCC mouse models. This work marks the first time long cycle pulses (1000 cycles) have been delivered with

a clinical system for drug delivery cavitation treatments, emphasizing the translation of the techniques and findings described here. Cavitation-induced transient tumor perfusion loss (TTPL) was quantified using our novel maximum intensity projection time area curve (MIP-TAC) analysis, and drug extravasation was assessed from doxorubicin fluorescent signal. Although inertial cavitation occurred in both conditions, the higher-pressure exposure produced a near-complete shutdown of tumor blood flow after a single treatment, which likely reduced measured drug penetration in subsequent injections. In contrast, the lower-pressure treatment exhibited a smaller degree of TTPL across injections and saw a in greater degree of doxorubicin extravasation, furthering the importance of considering vascular changes in cavitation treatment protocols. A reduction in tumor interstitial pressure in both conditions provides further insight into the improved drug delivery leveraged by cavitation treatments, suggesting that these conditions can mechanically alter the tumor microenvironment and relieve the pressure gradient. The ability to perform these cavitation treatments on a clinical diagnostic scanner and the introduction of a quantitative tool in MIP-TAC to evaluate vascular response provide new contributions to the field that hope to enhance clinical translation of these techniques. Similarly, the integration of real-time imaging employed in this work that is often omitted from similar cavitation studies emphasized its importance in providing feedback on vascular changes, necessary for the implementation of optimal treatment protocols.

Motivated by our findings, we investigated how acoustic pressure governs the spatial and temporal dynamics of TTPL in **Chapter 5** and discovered that this phenomenon could also be utilized as a diagnostic imaging biomarker. Using CEUS at multiple time points following a one-second-long cavitation treatment and employing our quantitative MIP-TAC analysis, we characterized TTPL recovery over a previously unexplored time course. Our data depicted that bulk TTPL recovery was shared across acoustic conditions, with average maximal reperfusion occurring 15 minutes after treatment. Elevated broadband energy confirmed inertial cavitation under both moderate- and high-pressure conditions where significant TTPL was observed, indicating that the resulting vascular responses were driven by mechanical forces from oscillating and collapsing microbubbles. These findings offer guidance for optimizing cavitation-based treatment protocols, that repeated exposures above 1 MPa must account for TTPL, as perfusion shutdown can significantly limit microbubble entry and reduce the effective dose delivered in subsequent

sonications. Through the new insights into the recovery process of TTPL and its effects on the tumor provided by this work, we considered its potential as a diagnostic tool in liver cancer for the first time. Acoustic conditions that induce transient flow shutdown without causing mechanical tissue damage to define a parameter window in which a tumor-specific vascular response can be elicited, and we filed a provisional patent for these methods as a result.

Finally, we are currently exploring how ultrasound cavitation treatments can influence antitumor immunity with and without use of immune checkpoint inhibitors in **Chapter 6**. This is the first work to demonstrate that TTPL is feasible with a cavitation treatment consisting of a single pulse and will evaluate whether tumor susceptibility to TTPL relates to responsiveness to ICIs. By using a transgenic mouse model of liver cancer that develops both HCC and intrahepatic cholangiocarcinoma (ICC) with a background of steatosis, we captured the heterogeneity of liver tumor phenotypes and an immune environment that is more like human liver cancer than other employed animal models. By administering ICIs (anti-PD-L1 and anti-CTLA-4) that have demonstrated efficacy in HCCs and ICCs, we aim to evaluate leukocyte infiltration in the tumor and further understand how ultrasound cavitation treatments can improve the efficacy of ICI therapy.

Facing the rising global burden of HCC, the development of new diagnostic and therapeutic technologies remains of high clinical importance. In this work, we investigated multiple facets of image-guided cancer therapy, from quantitative perfusion evaluations to biological impacts of cavitation treatments. We leveraged tools and acoustic parameters already available in clinical settings to improve the translation of findings here. Collectively, this thesis advances both the diagnostic and therapeutic dimensions of ultrasound–microbubble technology and contributes foundational knowledge toward developing clinically translatable theranostic strategies for HCC.

## 7.2 Future Directions

Several promising avenues for future investigation emerge from the findings of this work beyond the on-going immune checkpoint inhibitor work in **Chapter 6**. From a diagnostic perspective, true assessments of the sensitivity of our quantitative implementation of CEUS LI-RADS remain to be established. Evaluating patient populations with LR-3 and LR-4 lesions could help determine

whether the quantitative perfusion metrics defined here capture vascular characteristics consistent with HCC. These analyses may support earlier detection of HCC, with the potential to improve patient outcomes as HCC patients only receive treatment when suspect lesions are classified as LR-5. Additionally, the CEUS scanning protocol and quantitative analysis framework developed in this study could be applied to patients receiving immune checkpoint inhibitors to assess whether CEUS-derived tumor perfusion changes can serve as early predictors of therapeutic response.

With respect to cavitation treatments and TTPL, multiple directions warrant further exploration. Our current treatment protocol which delivered drug across four sequential cavitation exposures suggested that TTPL may transiently limit drug penetration. However, this design prevented a clear assessment of how acoustic pressure and the resulting tumor vascular change independently influence drug delivery. Future studies could address this by administering fluorescent model drugs (dextrans or similar tracers) and evaluate their intratumoral uptake following single cavitation exposures that either induce or do not induce TTPL. These experiments would clarify whether TTPL should be avoided when maximizing drug uptake is the primary therapeutic goal and establish at which acoustic parameters TTPL begins to heavily influence effects. Deepening our understanding of the mechanisms underlying TTPL is also of high importance. In vivo studies could administer inhibitors to isolate the possible influence of various proposed mechanisms, such as anti-thrombotic agent co-delivered to mitigate platelet aggregation. A greater understanding of the biological mechanism of TTPL would not only contextualize the variation of effect observed across acoustic conditions but also possibly introduce new questions regarding cascading biological effects of TTPL and their role in therapy.

Beyond its therapeutic implications, the spatial and temporal dynamics of TTPL characterized in this work suggest that it may also hold value as a clinical diagnostic tool. However, TTPL has not yet been evaluated in humans, and direct clinical assessment is necessary to determine its safety, and then diagnostic utility. Future studies could also integrate TTPL evaluations with super-resolution imaging or volumetric CEUS to better characterize how tumor vessel size, architecture, and spatial distribution relate to the extent of TTPL. These approaches may provide deeper insight into tumor vascular biology and expand the diagnostic potential of CEUS-based techniques in HCC.

## 7.3 LIST OF PUBLICATIONS AND PRESENTATIONS

Peer-reviewed publications

1. **Krolak C**, Wei A, Shumaker M, Dighe M, Averkiou M. A Comprehensive and Repeatable Contrast-Enhanced Ultrasound Quantification Approach for Clinical Evaluations of Tumor Blood Flow. Invest Radiol. 2025 Apr 1;60(4):281-290. doi: 10.1097/RLI.0000000000001127. Epub 2024 Oct 9. PMID: 39418656; PMCID: PMC11888899.
2. **Krolak C**, Dighe M, Clark A, Shumaker M, Yeung R, Barr RG, Kono Y, Averkiou M. Quantification of Hepatocellular Carcinoma Vascular Dynamics With Contrast-Enhanced Ultrasound for LI-RADS Implementation. Invest Radiol. 2024 Apr 1;59(4):337-344. doi: 10.1097/RLI.0000000000001022. Epub 2023 Sep 19. PMID: 37725492; PMCID: PMC10939991.
3. Voutouri C, Mpekris F, Panagi M, **Krolak C**, Michael C, Martin JD, Averkiou MA, Stylianopoulos T. Ultrasound stiffness and perfusion markers correlate with tumor volume responses to immunotherapy. Acta Biomater. 2023 Sep 1;167:121-134. Epub 2023 Jun 13. PMID: 37321529.
4. **Krolak C**, De Koninck L, Gu S, Wang YN, Powers JE, Averkiou M. Ultrasound cavitation therapy: inducing tumor drug delivery and blood flow changes with clinical ultrasound tools. J Control Release. 2026 May 10;393:114748. doi: 10.1016/j.jconrel.2026.114748. Epub 2026 Feb 23. PMID: 41740923.
5. **Krolak C**, De Koninck L, Gu S, Wang YN, Averkiou M. Transient tumor perfusion loss: a controllable vascular reaction to ultrasound cavitation treatments. (*submitted to Ultrasonics*)

Patents

1. Averkiou M., **Krolak C**. (2026). *Method and device for tumor identification with ultrasound contrast agents*. US provisional patent 63/991,557 (50619.01US1)

Conference proceedings

1. **Krolak C**, De Koninck L, Gu S, Pacheco JM, Averkiou M, "Vascular disruption: a controllable transient vascular tumor reaction to ultrasound cavitation treatments," In 2025 IEEE International Ultrasonics Symposium (IUS) (pp. 75-65). IEEE.
2. **Krolak C**, De Koninck L, Vuong K, Gu S, Pacheco JM, Powers J, Averkiou M, "Modulating tumor vasculature with a clinical scanner and approved contrast agents: are we ready for clinical translation?," 30th European Symposium on Ultrasound Contrast Imaging, pg. 32-34, Rotterdam, The Netherlands, Jan. 2025.
3. **Krolak C**, De Koninck L, Vuong K, Gu S, Pacheco JM, Loupas T, Wang YN, Averkiou M, "Evaluation of cavitation-induced tumor vascular disruption with a new quantitative perfusion method: time-area curve – TAC analysis," 30th European Symposium on Ultrasound Contrast Imaging, pg. 80-82, Rotterdam, The Netherlands, Jan. 2025.
4. De Koninck L, **Krolak C**, Powers J, Averkiou M, "Simultaneous PCD and CEUS to monitor microbubble cavitation treatments in an animal tumor model," 30th European Symposium on Ultrasound Contrast Imaging, pg. 111-113, Rotterdam, The Netherlands, Jan. 2025.

5. **Krolak C**, De Koninck L, Vuong K, Gu S, Wang YN, Averkiou M, "Vascular disruption: a potentially therapeutic tool in ultrasound cavitation treatments," In 2024 IEEE Ultrasonics, Ferroelectrics, and Frequency Control Joint Symposium (UFFC-JS) (pp. 155-156). IEEE.
6. De Koninck L, **Krolak C**, Vuong K, Shin S, Powers J, Averkiou M, "Modulation of the tumor microenvironment with a modified clinical scanner," In 2024 IEEE Ultrasonics, Ferroelectrics, and Frequency Control Joint Symposium (UFFC-JS) (pp. 78-79). IEEE.
7. **Krolak C**, De Koninck L, Vuong K, Gu S, Averkiou M, "Ultrasound and microbubble-mediated modulation of the tumor microenvironment for enhanced drug delivery," The 38th Annual Advances in Contrast Ultrasound Bubble Conference, Chicago, 2024.
8. De Koninck L, **Krolak C**, Vuong K, Powers J, Averkiou M, "Delivery of ultrasound cavitation therapy with a modified clinical scanner," J. Acoust. Soc. Am. 1 October 2023; 154 (4_supplement): A259. https://doi.org/10.1121/10.0023463
9. **Krolak C**, Shumaker M, Dighe M, Averkiou M, "Evaluating the reproducibility of contrast-enhanced ultrasound perfusion metrics in clinical data," In 2023 IEEE International Ultrasonics Symposium (IUS) (pp. 60-61). IEEE.
10. De Koninck L, Juang E, **Krolak C**, Averkiou M, "Investigation of combined ultrasound cavitation treatment with contrast microbubbles and mild hyperthermia in porcine liver" 22nd Annual International Symposium on Therapeutic Ultrasound (ISTU), Lyon, France, 2023
11. **Krolak C**, Shumaker M, Clark A, Dighe M, Averkiou M, "Tumor perfusion quantification with parametric processing of contrast-enhanced ultrasound," 28th European Symposium on Ultrasound Contrast Imaging, pg. 63-65, Rotterdam, The Netherlands, Jan. 2023.
12. Averkiou M, **Krolak C**, Clark A, Dighe M, "Automated quantification of hepatocellular carcinoma perfusion for LI-RADS classification with parametric image analysis," The 36th Annual Advances in Contrast Ultrasound Bubble Conference, Chicago, 2022.
13. **Krolak C**, Clark A, Dighe M, Averkiou M, "Characterization of hepatocellular carcinoma perfusion metrics with quantitative contrast-enhanced ultrasound," In 2022 IEEE International Ultrasonics Symposium (IUS). IEEE.
14. **Krolak C**, Clark A, Dighe M, and Averkiou M, "Evaluation and early detection of hepatocellular carcinoma with quantitative contrast-enhanced ultrasound," 27th European Symposium on Ultrasound Contrast Imaging, pg. 102-104, Rotterdam, The Netherlands, Jan. 2022.
15. **Krolak C**, Clark A, Dighe M, Averkiou M, Quantitative contrast-enhanced ultrasound for the evaluation and early detection of hepatocellular carcinoma. The Journal of the Acoustical Society of America. 2021 Oct;150(4):A33.